

**Monodisperse ZnO Micro and Nanoparticles  
Obtained by Micro Segmented Flow Synthesis**

---

**Dissertation**

Submitted to

**Faculty of Mathematics and Natural Science  
Technical University of Ilmenau**

To obtain the academic degree

**doctor rerum naturalium**

**(Dr. rer. nat.)**

by

**Shuning Li**

Sept. 2012



## **Doctoral Committee**

**Chairman:** Prof. Dr. rer. nat. habil. Michael Köhler  
(Department of Physical Chemistry and Microreaction Technology, TU  
Ilmenau)

**Referees:** Prof. Dr. rer. nat. habil. Michael Köhler  
(Department of Physical Chemistry and Microreaction Technology, TU  
Ilmenau)

Prof. Dr. rer. nat. habil. Uwe Ritter  
(Institute for Chemistry and Biotechnology, TU Ilmenau)

Dr. Challa Kumar  
(Center for Advanced Microstructures and Devices, Louisiana State  
University)

**Members:** Prof. Dr. rer. nat. habil. Andreas Bund  
(Department of Electrochemistry and Galvano Technique, TU Ilmenau)

Dr. rer. nat. Alexander Groß  
(Department of Physical Chemistry and Microreaction Technology, TU  
Ilmenau)

**Date for the viva voce:** 03. 09. 2012

**Date for the defense:** 03. 09. 2012



*To my family*

*for their endless love and support*



**Abstract**

ZnO micro and nanoparticles have attracted considerable interest because of their remarkable performance in electronics, optics and photonics. As a wide band gap semiconductor material, ZnO is also a potential candidate for various applications including gas sensing, light emitting devices and solar cells. Although some technologies have been developed to produce well-defined ZnO particles of different shapes and sizes, ZnO particles prepared by micro segmented flow synthesis have been rarely reported. The aim of this work was to develop a microfluidic system based on the micro segmented flow method and to test whether the microfluidic components are suitable for the generation and investigation of ZnO particles with improved homogeneity.

In order to optimize the experimental conditions, ZnO particles were first synthesized in batch. The optimized batch conditions were then adapted to two microfluidic arrangements for continuous synthesis of ZnO particles below 100 °C. The set-ups included computer-controlled syringe pumps, T-injectors, PTFE tubings and PTFE knot mixers in a thermostat water bath. The ZnO particles were obtained under strong alkaline conditions at elevated temperature in aqueous solution and DMSO solution. Needle-like, flower-like and compact ZnO particles were obtained. In nearly all cases, a strong effect of the flow conditions on the homogeneity of the formed particles was observed. The higher quality of the particles can be attributed to the fast mixing and enhanced heat transfer caused by segment-internal convection.

In addition, two other microfluidic set-ups were developed to control the ZnO formation reaction at temperature up to 150 °C. A static micromixer was used for mixing the reactants at room temperature. The formation of segmented flow was realized by injection of the reaction mixture into a carrier stream. The particle growth took place in PTFE tube coils inside a thermostat, which allowed to heat up to 150 °C. By using this set-up, flower-like, star-like, and spherical ZnO particles were successfully synthesized. The shape and size of the formed particles were strongly dependent on the reactant concentration and the molar ratio of NaOH/Zn(Ac)<sub>2</sub>. The total residence time for preparation of these particles was only 9.3 s, which is very short compared to the most

conventional methods.

The effect of the solvent on the formation of ZnO particle has also been investigated using this microfluidic set-up. Two different experimental conditions were applied to prepare ZnO particles, where  $\text{Zn}(\text{Ac})_2$  and NaOH in ethylene glycol (EG) were mixed with water or water/EG mixing solvent to achieve different water contents in the final mixture solution. The formation of homogeneous particles was characterized by SEM and TEM. A stronger dependence of the particle size and shape on the water content was observed. Furthermore, the water content can be used for tuning the optical absorption spectra of the formed ZnO particles.

Besides the ZnO microparticles, ZnO nanoparticles with an average diameter around 4-5 nm have been synthesized using  $\text{Zn}(\text{Ac})_2$  and LiOH in ethanol. The prepared nanoparticles exhibited green and blue emission under excitation at 325 nm. In order to understand the size-dependent optical properties of ZnO nanoparticles, extended X-ray absorption fine structure (EXAFS) spectroscopy was applied to study their local structure properties and compared with that of ZnO flower-like microparticles. The EXAFS measurements revealed higher vacancies and a higher degree of structural disorders in the nanoparticles than the microparticles. These disorders and vacancies could contribute to the blue shift of the visible emission from ZnO nanoparticles.

Due to the potential applications of semiconductor-metal composite particles in diverse areas, the flower-like ZnO microparticles obtained by micro segmented flow synthesis were used to fabricate ZnO/4-MBA/Au composite particles using a simple strategy. The formed composite particles were very homogeneous in shape and size. The surface coverage of Au nanoparticles on ZnO/4-MBA particles can be adjusted by changing the molar ratio of ZnO/4-MBA to Au. In order to study the interaction of 4-MBA molecules with ZnO and Au particles, Raman spectra of ZnO/4-MBA and ZnO/4-MBA/Au particles were analysed.

In summary, the segmented flow technique is suitable to generate ZnO particles with controlled size and morphology. Compared to most conventional methods, this technique offers several advantages, and it provides a new insight into material synthesis under environmentally friendly conditions.

**Abstract**

Mikro- und Nanopartikel aus Zinkoxyd (ZnO) besitzen bemerkenswerte Eigenschaften für Applikationen im Bereich der Elektronik, Optik und Photonik. Als ein Halbleitermaterial mit großer Bandlücke ist ZnO ebenfalls für die Entwicklung von Sensoren, Light Emitting Diodes (LEDs) und Solarzellen von hohem Interesse. Die Herstellung definierter Materialien mit einheitlicher Morphologie und enger Partikel-Größenverteilung ist hierzu eine wichtige Voraussetzung. Verschiedene Verfahren zur Herstellung entsprechender Partikel sind in der Vergangenheit untersucht worden. Die tropfenbasierte Mikrofluidik bietet die Möglichkeit einer exzellenten Reaktionskontrolle durch die Verwendung eines Tropfens als Reaktionsgefäß. Kurze Mischzeiten, hohe Heiz-/Kühlraten sowie eine definierte Verweilzeit ermöglichen so neben stöchiometrischen Parametern eine exakte Reaktionsführung. Ziel der hier vorliegenden Dissertationsschrift ist die Untersuchung der ZnO-Präzipitation in entsprechenden mikrofluidischen Systemen sowie die Charakterisierung der hergestellten Materialien.



## List of Publications

### Journal Papers

1. Y. Li, D. G. Yamane, **S. Li**, R. Reddy, J. S. Goettert, K. Nandakumar, C. S. S. R. Kumar, "Geometric Optimization of Liquid-Liquid Slug Flow in Flow-Focusing Millifluidic Devices", 2012, submitted
2. **S. Li**, A. Knauer, K. Risch, U. Ritter, J. M. Köhler, "Synthesis and Characterization of ZnO/4-Mercaptobenzoic Acid/Au Composite Particles", *Materials Letters*, 2012, revised
3. **S. Li**, A. Roy, H. Lichtenberg, G. Merchan, C. S. S. R. Kumar, J. M. Köhler, "Local Structure of ZnO Micro Flowers and Nanoparticles Obtained by Micro Segmented Flow Synthesis", *ChemPhysChem*, 2012, 13, 1557-1561
4. **S. Li**, G. A. Groß, P. M. Günther, J. M. Köhler, "Hydrothermal Micro Continuous-Flow Synthesis of Spherical, Cylinder-, Star- and Flower-like ZnO Microparticles", *Chemical Engineering Journal*, 2011, 167, 681-687
5. Knauer, A. Thete, **S. Li**, H. Romanus, A. Csáki, W. Fritzsche, J. M. Köhler, "Au/Ag/Au Double Shell Nanoparticles with Narrow Size Distribution Obtained by Continuous Micro Segmented Flow Synthesis", *Chemical Engineering Journal*, 2011, 166, 1164-1169
6. **S. Li**, S. Meierott, J. M. Köhler, "Effect of Water Content on Growth and Optical Properties of ZnO nanoparticles Generated in Binary Solvent Mixtures by Micro Continuous Flow Synthesis", *Chemical Engineering Journal*, 2010, 165, 958-965
7. Z. Chang, C. A. Serra, M. Bouquey, I. Kraus, **S. Li**, J. M. Köhler, "Multiscale Materials from Microcontinuous-Flow Synthesis: ZnO and Au Nanoparticle-Filled Uniform and Homogeneous Polymer Microbeads", *Nanotechnology*, 2010, 21, 015605
8. **S. Li**, P. M. Günther, J. M. Köhler, "Micro Segmented-Flow Technique for Continuous Synthesis of Different Kinds of ZnO Nanoparticles in Aqueous and in

DMSO Solution”, Journal of Chemical Engineering of Japan, 2009, 42, 338-345

**Conference Proceedings**

1. Z. Chang, **S. Li**, M. Bouquey, I. Kraus, C. A. Serra, J. M. Köhler, “Continuous-Microflow Synthesis of Multiscale Materials Based on Polymer Microparticles/Inorganic Nanoparticles Composites”, Proceedings of the Second WSEAS International Conference on Nanotechnology, 2010
2. **S. Li**, P. M. Günther, J. M. Köhler, “Micro Segmented-Flow Technique for Continuous Synthesis of Fluorescent ZnO Micro- and Nanoparticles”, Micro System Technique Congress, 2009

---

**Table of Contents**

<b>1</b>	<b>Introduction</b>	<b>1</b>
1.1	ZnO crystals	1
1.1.1	Crystal structure	3
1.1.2	Physical properties and device applications	4
1.1.3	Synthesis methods	9
1.2	Micro segmented flow	13
1.2.1	Segment formation and manipulation	14
1.2.2	Unique features of micro segmented flow	15
1.2.3	Applications of micro segmented flow	18
1.3	Aim and objective	21
<b>2</b>	<b>Materials and methods</b>	<b>22</b>
2.1	Microfluidic systems for synthesis of ZnO particles	22
2.2	Particle synthesis	28
2.2.1	ZnO micro and nanoparticles	28
2.2.2	Au nanoparticles	28
2.2.3	ZnO/Au composite particles	29
2.2.4	ZnO/4-MBA/Au composite particles	29
2.3	Chemicals	30
2.4	Characterization	32
2.4.1	pH meter	32
2.4.2	UV/Vis spectroscopy	32
2.4.3	Photoluminescence (PL) spectroscopy	33
2.4.4	Scanning electron microscopy (SEM)	33
2.4.5	Transmission electron microscopy (TEM)	34

2.4.6	Differential centrifugal sedimentation (DCS)-----	35
2.4.7	Small angle X-ray scattering (SAXS) -----	36
2.4.8	X-ray diffraction (XRD)-----	37
2.4.9	X-ray absorption spectroscopy (XAS) -----	38
2.4.10	Thermogravimetric analysis (TGA) -----	40
2.4.11	Raman spectroscopy -----	41
<b>3</b>	<b>Results and discussion -----</b>	<b>42</b>
3.1	Continuous synthesis of ZnO particles by micro segmented flow technique in aqueous and dimethylsulfoxide (DMSO) solutions-----	42
3.1.1	Batch synthesis of ZnO particles-----	42
3.1.2	Micro segmented flow synthesis of ZnO particles in aqueous solution-----	43
3.1.3	Micro segmented flow synthesis of ZnO particles in DMSO solution-----	46
3.2	Hydrothermal micro segmented flow synthesis of ZnO microparticles with different morphologies -----	50
3.3	Effect of the water content on growth and optical properties of ZnO particles generated by micro segmented flow synthesis -----	60
3.4	Local structure studies of ZnO micro flowers and nanoparticles obtained by micro segmented flow synthesis -----	71
3.5	Synthesis and characterization of ZnO composite particles-----	79
3.5.1	Solution-based method -----	79
3.5.2	Assembly method -----	82
<b>4</b>	<b>Conclusion and outlook -----</b>	<b>90</b>
<b>5</b>	<b>References -----</b>	<b>92</b>
<b>6</b>	<b>Appendix -----</b>	<b>109</b>

---

6.1	Abbreviations -----	109
6.2	Synthesis of water core/polymer shell particles by co-axial capillaries microfluidic device-----	110
6.2.1	Experimental methods-----	111
6.2.2	Results and discussion-----	112
6.3	Generation of monodisperse slugs by a flow-focusing millifluidic chip -----	121
6.3.1	Experimental methods-----	121
6.3.2	Results and discussion-----	122
6.4	Preparation of Co-doped ZnO nanoparticles by micro segmented flow synthesis -----	125
6.5	Batch synthesis of Ag and Au nanoparticles -----	128
6.6	Scientific publications -----	129
6.7	Curriculum vitae-----	132
6.8	Acknowledgements -----	134



# 1 Introduction

## 1.1 ZnO crystals

In recent years, significant interest has emerged in wide band gap semiconductor materials due to an increasing need for short-wavelength photonic devices and high-power, high-frequency electronic devices [1]. Zinc oxide, as a typical II-VI semiconductor material, has received much attention lately because of its direct wide band gap ( $\sim 3.3$  eV at 300 K) and high exciton binding energy (60 meV). It allows high efficient excitonic emission at room temperature and makes ZnO a promising material for UV optoelectronic devices such as UV light emitting diodes and photodetectors. The lack of a center of symmetry in wurtzite, combined with large electromechanical coupling, results in strong piezoelectric and pyroelectric properties and the consequent use of ZnO in mechanical actuators and piezoelectric sensors [2]. Moreover, under high pressure, the melting point of ZnO is 1975 °C, which determines its high thermal stability. Transparency to visible light provides opportunities to develop transparent electronics and UV optoelectronics. Due to its attractive physical properties, ZnO has turned into a new hot focus in the field of optics [3], optoelectronics [4], and sensors [5-6] during the past decade.

ZnO can be considered as an “old” material and has been studied for several decades. In terms of characterization, the lattice parameter studies date back to 1929 by Fuller [7] and 1935 by Bunn [8], detailed optical properties were investigated by Mollwo in 1954 [9] and vibrational properties were studied by Raman scattering by Damen *et al.* in 1966 [10]. The research peaked at the end of 1970s and beginning of 1980s, driven by the availability of good bulk single crystals and first epitaxial layers [11]. Then the interest faded away. The main obstacle to the development of ZnO has been the lack of reproducible and low-resistivity p-type ZnO [12-13]. The present renaissance in ZnO research started in the middle 1990s. It has been documented by numerous conferences, workshops, symposia and more than 1000 ZnO-related papers per year compared to slightly beyond 100 in 1970 [14-15]. More reviews and books on ZnO have been published recently [2, 11, 14, 16-19].

It is necessary to know that ZnO occupies already an enviable place in the industrial market. ZnO is industrially produced at levels of  $10^5$  tons each year. It is widely used in the rubber

manufacturing (~ 36 %), in the industry of ceramics as a flux (~ 26 %), in the chemical industry (~ 20 %), in the animal food as trace elements (~ 12 %) and in paints (~ 3 %; 50 % in 1961). The last 3 % are used for different applications, for example in electronics (ferrites, varistors), ends of matches and pharmaceutical industry [20].

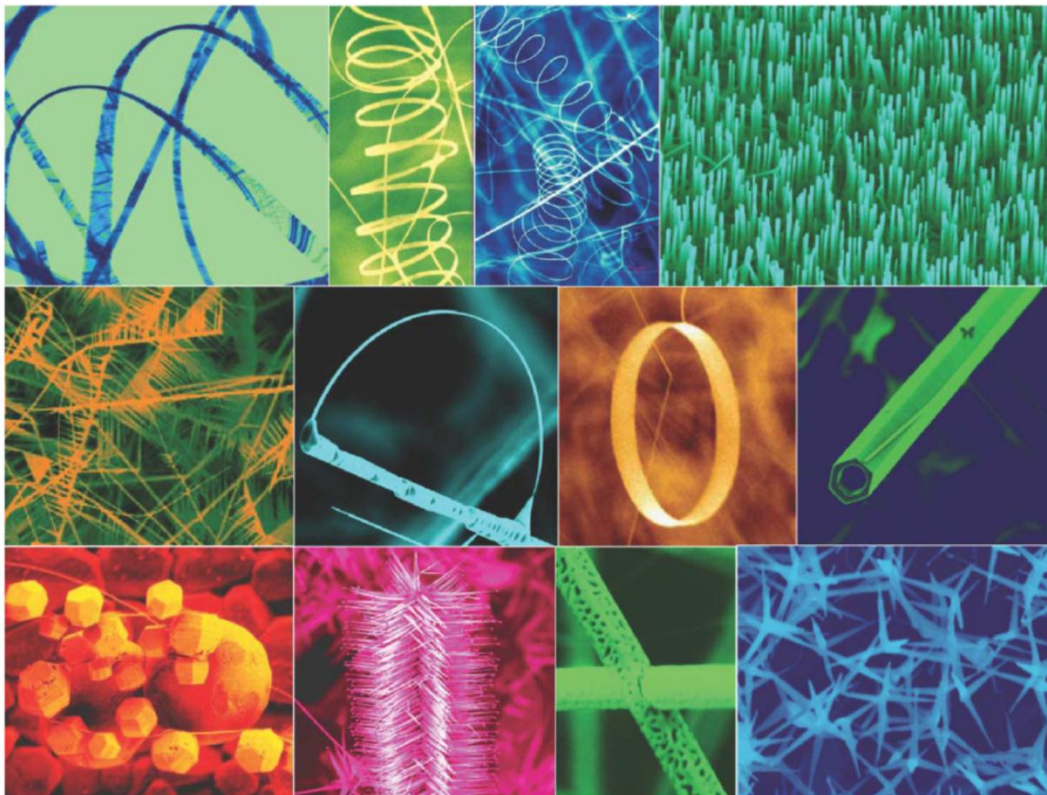


**Fig. 1.1** Different morphologies of ZnO nanostructures [21].

Nanostructured ZnO materials have also received considerable interest because of their remarkable performance in electronics, optics and photonics. Different nanostructure morphologies of ZnO have been reported including nanowires [22], nanorods [23], nanocombs [24], nanoflowers [25], nanorings [26], nanohelices [27-28] and nanocages [29] (Fig. 1.1). These nanostructures can be obtained by different fabrication methods, such as vapor-phase transport [30], chemical vapor deposition [31-33] and hydrothermal synthesis [17]. With reduction in size, ZnO nanostructures possess several unique advantages such as high specific surface area, chemical stability, electrochemical activity and high electron communication features, which mainly result from the quantum confinement effect [2]. Such properties indicate a wide range of novel applications in photodetectors, sensors, light emitting diodes and varistors. They are also

attractive for biomedical applications due to their bio-safety and large surface area [34].

This section gives an in-depth description of the crystal structure, physical properties, applications and synthesis techniques of ZnO.

### 1.1.1 Crystal structure

Zinc oxide crystallizes in three forms: hexagonal wurtzite, cubic zincblende, and the rarely observed cubic (rocksalt) structure. At ambient temperature and pressure, the wurtzite structure is most stable and thus most common. The zincblende form can be stabilized by growing ZnO on substrates with cubic lattice structure. In both cases, the zinc and oxide centers are tetrahedral. The rocksalt (NaCl) structure is only observed at relatively high pressures (about 10 GPa) [35]. The cubic zincblende and rocksalt structures are illustrated in Fig. 1.2 [19].

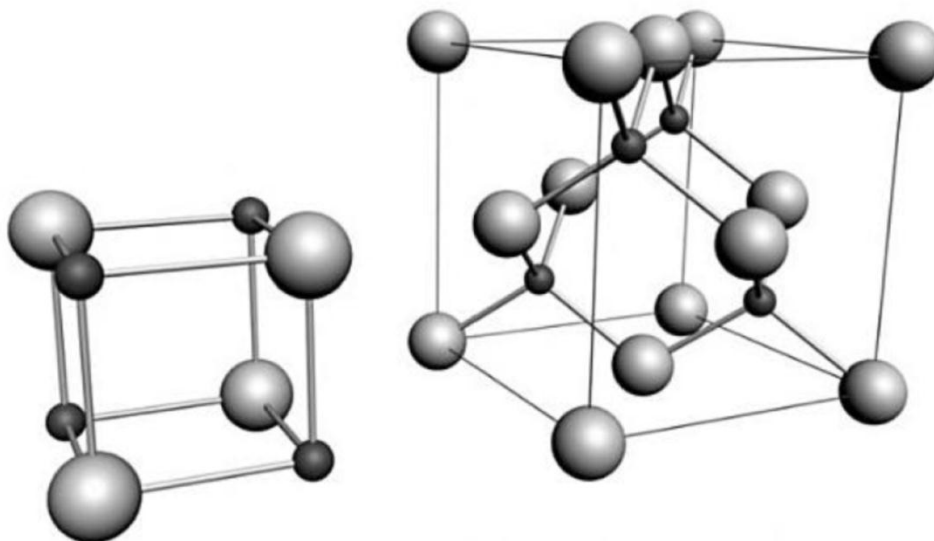


**Fig. 1.2** The rocksalt (left) and zincblende (right) phases of ZnO. Oxygen atoms are shown as white spheres, zinc atoms as black spheres. Only one unit cell is illustrated for clarity [19].

Wurtzite ZnO has a hexagonal structure with lattice parameters  $a = 0.32495$  nm and  $c = 0.52069$  nm; their ratio  $c/a \sim 1.60$  is close to the ideal value for hexagonal cell  $c/a = 1.633$ . As in most group II-VI materials, the bonding in ZnO is largely ionic. The structure of wurtzite ZnO can be described as a number of alternating planes composed of tetrahedrally coordinated  $O^{2-}$  and  $Zn^{2+}$  stacked alternately along the  $c$ -axis, as shown in Fig. 1.3 [2]. The tetrahedral coordination in ZnO results in polar symmetry along the hexagonal axis. This polarity is responsible for some of

the properties of ZnO, including its piezoelectricity and spontaneous polarization. It is also a key factor in crystal growth, etching and defect generation [19].

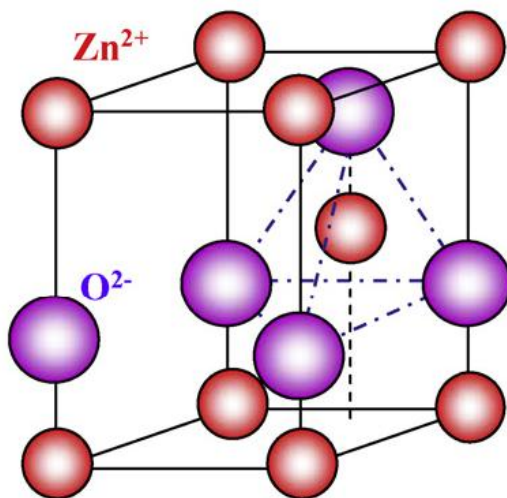


**Fig. 1.3** The wurtzite structure model of ZnO. The tetrahedral coordination of Zn-O is shown [16].

Another important characteristic of ZnO is polar surfaces. The most common polar surface is the basal plane (0001). One end of the basal polar plane terminates with partially positive Zn lattice sites and the other end terminates in partially negative oxygen lattice sites. The oppositely charged ions produce positively charged Zn-(0001) and negatively charged O-(000 $\bar{1}$ ) surfaces, resulting in a normal dipole moment and spontaneous polarization along the *c*-axis as well as a variance in surface energy. To maintain a stable structure, the polar surfaces generally have facets or exhibit massive surface reconstructions. However, ZnO  $\pm$  (0001) are an exception, and they are atomically flat, stable and without reconstruction [36-37]. Efforts to understand the superior stability of the ZnO  $\pm$  (0001) polar surfaces are at the forefront of research in today's surface physics [2, 38-41].

### 1.1.2 Physical properties and device applications

The basic physical properties of ZnO are shown in Table 1.1 [22, 42-43]. It is worth noting that there is still uncertainty in some of the values. For example, the values for thermal conductivity show some spread in values and this may be a result of the influence of defects such as dislocations [43].

**Table 1.1** Properties of wurtzite ZnO.

Property	Value
Lattice constants (T = 300 K)	
<i>a</i>	0.32495 nm
<i>c</i>	0.52069 nm
<i>a/c</i>	1.602
Density	5.606 g/cm <sup>3</sup>
Stable phase at 300 K	wurtzite
Melting point	1975 °C
Thermal conductivity	0.6-1.2 W/m·K
Linear expansion coefficient	<i>a</i> : $6.5 \times 10^{-6} \text{ }^\circ\text{C}^{-1}$ <i>c</i> : $3.0 \times 10^{-6} \text{ }^\circ\text{C}^{-1}$
Refractive index	2.0
Energy gap	3.3 eV (direct)
Exciton binding energy	60 meV

Due to the wide range of useful properties, ZnO offers versatile potentials for providing electric, photonic and sensor devices. In the following, the recent progress in device applications of ZnO is presented.

### Light emitting devices

ZnO is considered as a potentially attractive material for light emitting devices in the ultraviolet region. The main reasons are its large exciton binding energy (60 meV), which permits excitonic emission at room temperature and above. It is well known that light emitting diodes (LED) require both p-type and n-type material. Since the growth of reproducible p-type ZnO has not been developed yet, widespread fabrication of ZnO p-n homojunction-based LEDs is not possible. Therefore, n-type ZnO growth on other available and comparable p-type materials could provide an alternative way for at least demonstrating the advantages of ZnO [44-45]. This subject has received much attention recently. The heterojunctions have been realized by use of

different p-type semiconducting materials, such as GaN [46], SiC [47], Si [48], NiO [49] and diamond [50]. For example, Ya. I. Alivov *et al.* [51] have reported the growth, processing and fabrication of n-ZnO/p-GaN heterojunction LED devices on Al<sub>2</sub>O<sub>3</sub> substrates. Room-temperature electroluminescence in the blue-violet region with a peak wavelength of 430 nm has been observed from this structure under forward bias. O. Lupan *et al.* [52] have used ZnO nanowires/p-Si heterostructures to fabricate a LED structure. The threshold forward voltage is low (1.4 V). At room temperature this device emits a broad visible band centered at 590 nm. More details of these heterostructure LEDs have been summarized in several review studies [13, 45, 53] and books [44, 54].

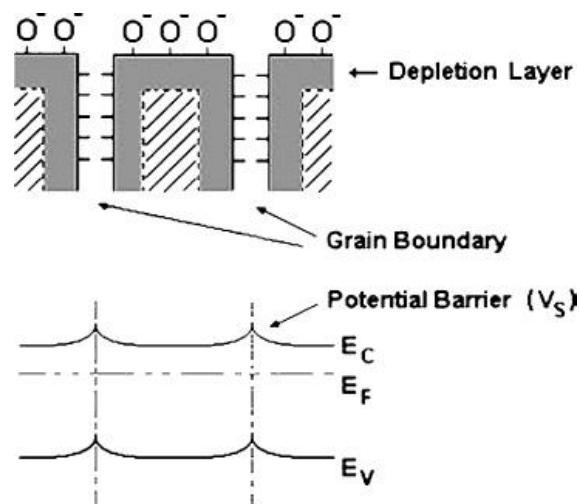


**Fig. 1.4** Formation of depletion layers in the surface and grain boundary regions of ZnO due to the oxygen chemisorption [5, 54-55].

### Gas sensors

ZnO has been widely used for sensing applications because of its high sensitivity to the chemical environment. The sensing mechanism of ZnO-based sensors can be explained by the modulation model of the depletion layer shown in Fig. 1.4 [5, 55].

The oxygen vacancies in ZnO act as an electron donor on ZnO surfaces providing electrons to the conduction band and making ZnO an n-type semiconductor. Oxygen from the ambient adsorbs on the ZnO surface and captures electrons from the conduction band and form O<sup>-</sup> (Equation 1.1). After sufficient adsorption of oxygen, depletion layers are formed on the surface region of ZnO, leading to a decreasing conductivity. When the sensors are exposed to reducing

gases, for instance, ethanol, the gases will react with the adsorbed  $O^-$  (Equation 1.2) and release the trapped electrons back to the conduction band. This leads to an increase in conductivity [5, 44, 55].



As one of the most widely applied gas-sensing materials, ZnO has been extensively studied for a long time because of its high chemical stability, low cost and good flexibility in fabrication. Many experimental results have demonstrated that ZnO exhibits pronounced gas sensitivity for detecting  $NH_3$  [56], CO [57],  $H_2$  [58],  $O_3$  [59],  $H_2S$  [60],  $NO_2$  [61] and  $C_2H_5OH$  [55, 62]. L. Liao *et al.* [55] have reported different ZnO nanorods sensors, which can detect  $C_2H_5OH$  and  $H_2S$  (100 ppm) in air. The results show that the thin nanorods have a significantly better sensitivity than the thick nanorods since the density of oxygen vacancies increases when the diameter of the ZnO nanorods decreases. Q. Wan *et al.* [62] have fabricated a ZnO nanowire sensor. It exhibits high sensitivity and fast response upon exposure to 1, 5, 50, 100 and 200 ppm ethanol gas at 300 °C.

### **Dye-sensitized solar cells**

Dye-sensitized solar cells (DSSCs) are promising devices for low-cost solar energy conversion and are intensively investigated nowadays. ZnO is obviously one of the best candidates among semiconductors for DSSC applications because it can be synthesized easily and inexpensively in different shapes and sizes by using various methods, and it is environment friendly and stable [44].

Fig. 1.5 demonstrates a typical DSSC structure, which is mainly composed of three parts: (1) a ~ 10  $\mu m$  thick film of a wide band gap semiconductor such as ZnO or  $TiO_2$  nanoparticles, (2) a monolayer of dye molecules adsorbed on the semiconductor nanostructures, and (3) an electrolyte containing a redox couple (traditionally  $I^-/I_3^-$ ) that penetrates in between the dye-coated nanostructure, serving as charge carrier [45]. The semiconductor nanoparticles harvest the electrons from photo-excited dye molecules and transport them to the collecting anode.

Meanwhile, the oxidized dyes are reduced by redox species that convey electrons from the counter electrode [45, 63-64].

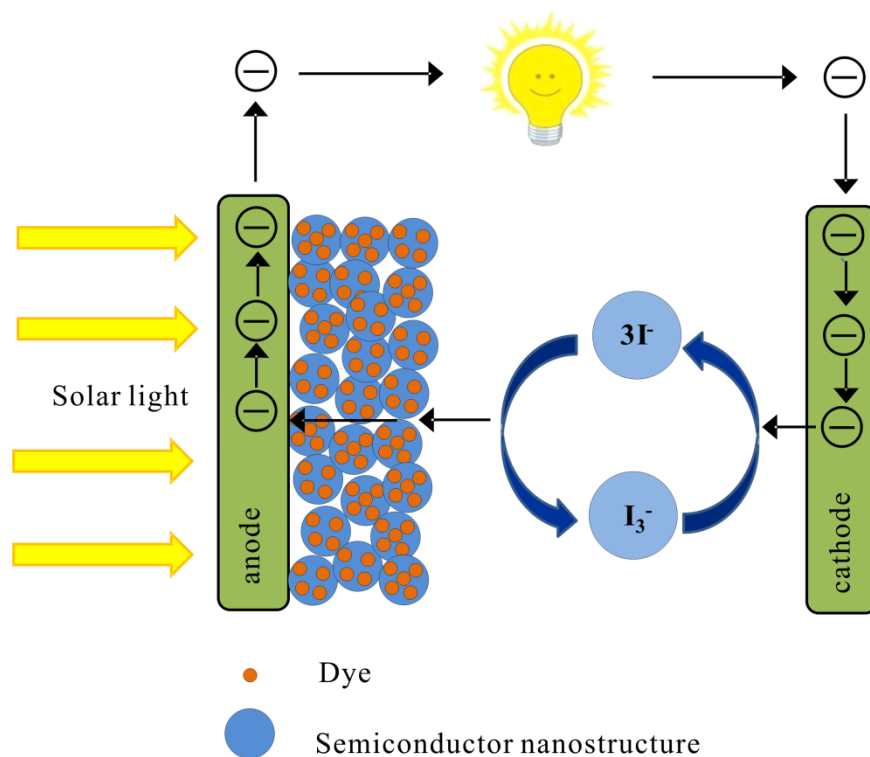


**Fig. 1.5** Schematic diagram of dye-sensitized solar cell.

So far, various ZnO nanostructures have been extensively studied for DSSCs. ZnO arrays of 1D nanostructures, such as nanowires and nanotubes have been widely utilized to significantly enhance the electrons transport velocity within the photoanode by providing a direct conduction pathway for the rapid collection of photogenerated electrons [65]. However, the insufficient internal surface area of these 1D nanostructure arrays limits the power conversion efficiency at a relatively low level, for example, only 1.5 % for ZnO nanowires [66] and 1.6 % for nanotubes [67]. In addition, 2D and 3D ZnO nanostructures have also been investigated for DSSC applications due to their large specific surface area. F. Xu *et al.* [65] have presented a DSSC based on hierarchical ZnO nanowire-nanosheet architectures, which show a power conversion efficiency of 4.8 %. C. Wu *et al.* [68] have fabricated a 3D ZnO nanodendrite/nanoparticle composite DSSC with an efficiency of 3.74 %. The highest efficiency reported up to date is 7.2 % achieved with a porous single crystal [69].

### 1.1.3 Synthesis methods

**Table 1.2** Methods for ZnO deposition and growth.

General Techniques	Sub-techniques
Physical Vapor Deposition (PVD)	Thermal evaporation Electron beam-PVD Sputtering Pulsed laser deposition
Chemical Vapor Deposition (CVD)	Thermal CVD Low pressure CVD Plasma enhanced CVD Metal-organic CVD Molecular beam epitaxy (MBE)
Solution Based Chemistry (SBC)	Hydrothermal synthesis Polyol-mediated synthesis Sol-gel synthesis Template-assisted synthesis

A variety of methods exist for ZnO deposition and growth. They can be broadly classified into three main methods: physical vapor deposition (PVD), chemical vapor deposition (CVD) and solution based chemistry (SBC). Each method can be subdivided into different individual techniques shown in Table 1.2 [5, 70-71]. Gas phase synthesis methods (PVD and CVD) are applied in a gaseous environment in a closed chamber and have been widely used to prepare ZnO nanostructures. However, due to the complex processes, sophisticated equipment and high temperatures, they can hardly be used for large-scale production in commercial applications [32]. In recent years, solution based chemistry methods have attracted more and more attention and have already been commonly used to grow ZnO with high yield and uniformity at relatively low temperature. Three of them have been applied to grow ZnO micro and nanoparticles in this work, and they are discussed in more detail below.

#### Hydrothermal Synthesis

Hydrothermal synthesis can be defined as a synthesis method for growing single crystals from an aqueous solution at high temperature under high vapor pressure. Since no sophisticated equipment is required and crystalline can be created directly from the solution, hydrothermal synthesis provides a simple and effective option for large-scale production of ZnO crystals. Compared to other growth methods, hydrothermal synthesis has several advantages such as low cost, high yield, rapid growth rates and environmental friendliness [72]. The size and shape of the obtained ZnO particle can be easily controlled by adjusting the reaction temperature, reaction time, reactant concentrations or molar ratio of precursors. For example, a controlled synthesis of flower- and rod-like ZnO particles has been realized by hydrothermal method at 120 °C. The well-defined morphologies were obtained by simply tuning the ratio of sodium hydroxide to zinc acetate in narrow range [73]. Well-faceted hexagonal ZnO nanorods have been synthesized at relative low temperature (90 °C) without any catalyst or templates. The experiments have shown that the diameter of the ZnO nanorods decreased with prolonging the reaction time [74].

In addition, hydrothermal synthesis enables the synthesis of ZnO nanostructures with unique shapes by use of organic additives. C. Kuo *et al.* [75] have prepared unusual ZnO microspheres constructed of interconnected nanostructures by hydrothermal synthesis. Trisodium citrate plays a key role in directing the formation of these microstructures. These microspheres possess high surface areas (28.9 m<sup>2</sup>/g) and can be examined for applications as a catalyst support. Y. Peng *et al.* [76] have developed ZnO nanorings and nanodisks on a large scale by using polyacrylamide (PAM) and carboxyl-functionalized polyacrylamide (PAM-COOH) as crystal growth modifiers. Polymer-directed crystal growth and mediated self-assembly of nanocrystals may provide promising routes to synthesis of various ordered inorganic materials with complex structures.

### **Polyol-mediated synthesis**

Polyol-method synthesis has turned out to be well suited for the preparation of spherical oxide particles of 30-200 nm [77]. This method is based on heating suitable metal salts and a defined amount of water in a multivalent and high-boiling alcohol, such as ethylene glycol, diethylene glycol or polyethylene glycol. The alcohol itself can act as a stabilizer and therefore, it can limit the growth of particles and prohibit the particles agglomeration. Due to high reaction temperature which can be applied (> 150 °C), highly crystalline oxides are often produced [78]. This

technique is comparably easy to perform and has been applied to prepare a variety of materials including sulfides [79], phosphates [80] and elemental metals [81-84].

C. Feldmann *et al.* [78] have applied this method to prepare nanoscale functional materials, such as color pigments, transparent conducting oxides and catalytically active oxides. The reactants mixture was heated to 180 °C-240 °C for 2-12 h. The average particles diameter can be adjusted by tuning the reaction temperature and duration of the reaction, the concentration of metal precursor and the amount of water. All the experiments yield stable suspensions of almost non-agglomerated nanoscale particles. The solid content in diethylene glycol can be up to 20 %.

### **Sol-gel synthesis**

The sol-gel process involves the evolution of inorganic networks through the formations of a colloidal suspension (sol) and gelation of the sol to form a network in a continuous liquid phase (gel). With further processes, it is possible to produce powders, films, fibers and monoliths. The sol-gel process normally consists of the hydrolysis and condensation of a precursor.

The sol-gel routes to prepare visible luminescent ZnO nanoparticle colloids were invented in the 1980s and were investigated intensively in the 1990s [85]. The most popular way is to hydrolyze zinc acetate in ethanol and produce ZnO nanoparticles with typical green-yellow emission at 500 nm-550 nm. However, the prepared ZnO colloids are very unstable. They can grow and precipitate from the mother-liquor at room temperature. E. Meulenkamp [86] has prepared ZnO nanoparticles with diameters from 2 nm to 7 nm by sol-gel synthesis. It is found that aging of particles is governed by temperature, water content and the presence of reaction products. Water and acetate can induce considerably accelerated particle growth.

Recently, several groups [87-90] have tried to employ various polymers to protect the ZnO nanoparticles and to improve their luminescent properties. H. Xiong *et al.* [88] have synthesized a novel type of polymer nanocomposites, ZnO(PEGME), in which ZnO nanoparticles and poly(ethylene glycol methyl ether) (PEGME) molecules were connected by covalent bands. The results have demonstrated that the growth and aggregation of the ZnO(PEGME) were effectively hindered by the polymer groups, so the fluorescence of ZnO(PEGME) could be adjusted from blue to yellow stably.

Compared to these conventional methods, microfluidic segmented flow is still a new technology for ZnO synthesis. In the following section, this technique will be described in detail.

## 1.2 Micro segmented flow

In microfluidics devices, small volumes of fluids (from  $10^{-9}$  to  $10^{-18}$  liter) are processed in channels with dimensions from tens to hundreds of micrometers [91-92]. Compared to conventional batch synthesis, microfluidic technologies offer a number of advantages, such as lower reagent consumption, high heat and mass transfer rates as well as safer operation. Consequently, the microfluidic devices have been widely developed and utilized for chemical and biological reactions over the past 10 years [91, 93-97].

Segmented flow microfluidics is one subcategory of microfluidics. The segmented flow contains at least two immiscible phases: one dispersed phase and one continuous phase. In principle, the droplets of the dispersed phase are immersed in the continuous phase which preferentially wets or coats the surface of the micro channel.

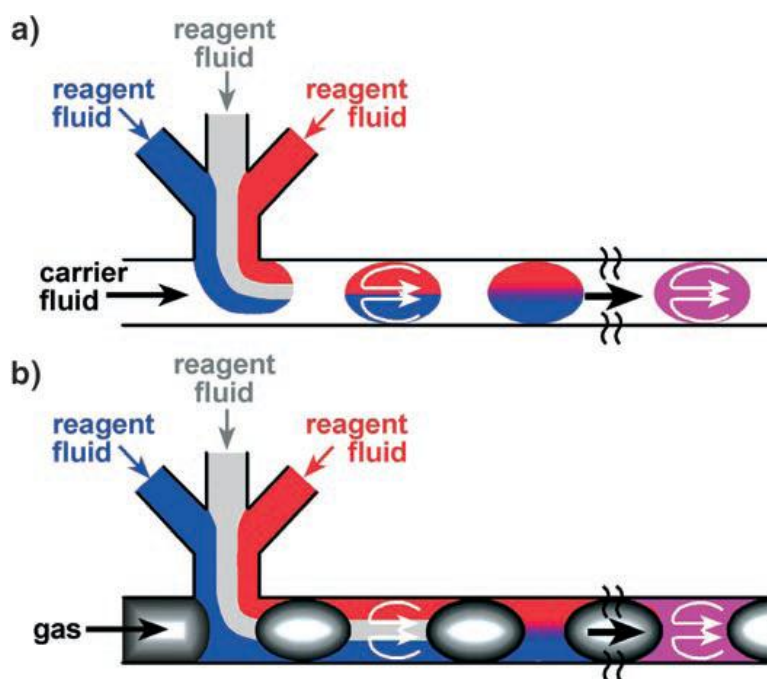


**Fig. 1.6** Two types of segmented flows in microfluidic channels: (a) liquid-liquid flow; (b) gas-liquid flow [94].

Based on the phase in which the reaction takes place, segmented flow can be divided into two categories: droplet flow (liquid-liquid flow) and bubble flow (gas-liquid flow) regimes (Fig. 1.6) [94, 98]. In the first type of segmented flow (Fig. 1.6a), the reaction occurs in droplets which do not come into contact with the microchannel since the carrier fluid wets the microchannel. In the

second type (Fig. 1.6b), the reagent fluid is separated by the gas bubbles. Reactions take place within the liquid “slugs” that form the continuous phase; reagents are exposed to the walls of the channels [94].

### 1.2.1 Segment formation and manipulation

The development of microfluidic systems which allow the formation of micro segments or microdrops has received significant attention over the past decade. Different techniques have been developed to get fine control over the size, shape and monodispersity of droplets in a microchannel network. Two of the most frequently used methods are T-junction [92, 99-101] and flow focusing geometries [102-105].

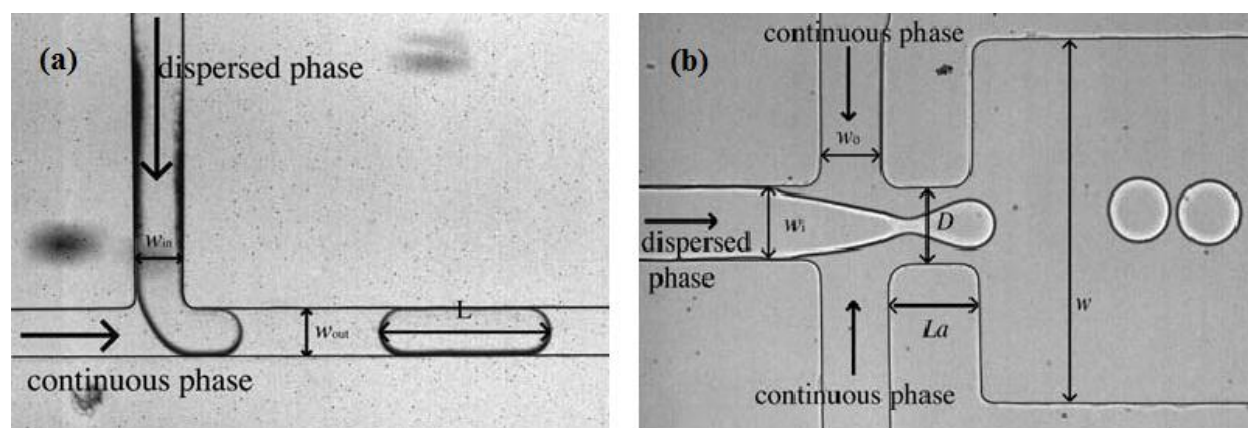


**Fig. 1.7** Examples of droplet production in (a) a T-junction and (b) a flow-focusing device [106].

Droplet formation in a T-shaped device was first demonstrated in 2001 by Thorsen *et al.* [100], who generated monodisperse droplets by use of pressure controlled flows in microchannels. A typical example of a T-junction is shown in Fig. 1.7a [106], in which the dispersed phase is injected perpendicularly into the continuous phase. The two phases form an interface at the junction when they meet each other. As fluid flow continues, the tip of the dispersed phase enters the main channel and then elongates due to the shear forces generated by the continuous phase and the subsequent pressure gradient. When the neck of the dispersed phase becomes too thin, it will eventually break to form a droplet and flow along the outlet channel [107-108]. Numerical studies have shown that the size of the droplets is strongly dependent on the fluid flow rates [99, 107], the channel design [92], the surfactant concentration [101], and the continuous-phase viscosity [92, 101].

The flow focusing geometry was first proposed by Anna *et al.* [109] and Dreyfus *et al.* [110] in 2003. As shown in Fig. 1.7b [100], the dispersed phase flows in a central channel and two continuous phases flow in two side channels. Both phases are then impelled to flow through a small orifice that is located downstream of the three channels [111]. The outer fluid applies pressure and viscous stresses which drive the inner fluid into a narrow strand, then breaks up and releases droplets [112]. The formed droplets size can be adjusted by changing the flow rates of the two phases. Moreover, the smallest droplets can be much smaller than the orifice radius [101]. This technology has been very advantageous for encapsulation and particle design. For example, Martin-Banderas *et al.* [103] have used a flow focusing device to synthesize 5  $\mu\text{m}$  fluorescence particles and multiple-core particles with a very reproducible size distribution.

Micro segments can be used as independent micro reactions for various purposes. When performing complex chemical and biological reactions, the ability of fusion (merging) of two segments to one larger segment and splitting (fission) of a segment in two parts become highly important. The fusion of segments in microfluidics can be achieved using a variety of methods. These include use of a cross junction [113], a widening channel followed by a narrower channel [114] and applying electric field [115]. Splitting of segments has been performed with several channel designs including T-junction [116], branching channels [97] and with isolated obstacles [117]. Detailed discussions can be found in reviews [97, 106, 111].

### **1.2.2 Unique features of micro segmented flow**

Compared to conventional techniques, micro segmented flow is marked by a series of unique features.

#### **Fast mixing**

In conventional vessels, mixing is limited by the site of vortices in the flow fields created by the stirring or the impeller [118]. Undesired concentration gradients are unavoidable during the batch reaction process. On the contrary, micro segmented flow allows rapid mixing due to small dimensions and substantial internal convection [119]. Complete mixing can be achieved within milliseconds, which can hardly be realized in batch reactors.

In microchannels, the flow is laminar due to high viscous forces and surface effects. The mixing

inside the microchannels is largely controlled by molecular diffusion. Although the diffusion distance is shorter within micro segments, the time required to completely mix the two fluids is still long [97]. However, segmentation of the two immiscible phases induces internal convective mixing in the microchannels, and it can ensure reagent homogeneity within each segment. In addition, clever channel designs can enhance internal mixing within segments. Song *et al.* [116] have used winding microfluidic channels to generate intensified advection. It can accelerate mixing by using unsteady fluid flow to stretch and fold a volume of fluid. With this technique, complete mixing in about 2 ms with no dispersion can be achieved. Paik *et al.* [120] have developed an electrowetting-based droplet mixer, which takes advantage of the ability to perform droplet splitting and fusion over three electrodes. This results in a mixing time of 1.7 seconds when using an electrode aspect ratio below 0.2.

### **Effective heat exchange**

The specific surface areas per unit volume in the microchannels amount to 10,000 to 50,000  $\text{m}^2/\text{m}^3$ , whereas the typical laboratory and production vessels usually do not exceed 1000  $\text{m}^2/\text{m}^3$  and 100  $\text{m}^2/\text{m}^3$ , respectively [121]. As a result of their highly increased surface to volume ratio, microreactors possess heat transfer coefficients of the order of  $6 \times 10^4 \text{ W m}^{-2} \text{ K}^{-1}$  compared to  $\sim 100 \text{ W m}^{-2} \text{ K}^{-1}$  for batch vessels [122]. Consequently, in microfluidic systems, highly efficient input or removal of heat and nearly constant reaction temperatures can be achieved due to high surface to volume ratios [118]. In addition, the segment-internal convection leads to a significant enhancement of heat transfer by a fast exchange of central and peripheral volume parts within a segment. Therefore, temperature gradients can be reduced quickly, exothermic or explosive reactions such as nitration reactions can be controlled in a safe manner [123-124].

### **Short residence time distribution**

The residence time distribution (RTD) is one of the most important parameters in continuous-flow processes. It provides information about the fractions of the reaction mixture that passes the reactor in certain time intervals below the mean residence time or above it [125]. Therefore, it is responsible for the intensity and homogeneity of heat exchange and control of reaction rate. These are highly important parameters for the preparation of nanoparticles with high quality. Compared to much larger residence time distributions in conventional stirred tank reactors, the

segmented flow technique offers narrower RTD due to recirculation within segments, and it has been applied for preparation of nanomaterials with controlled size and distribution, for example, CdSe quantum dots [126]. In addition, the determination of RTD in microreactors is of high importance. D. Boskovic *et al.* [127] have applied an experimental input-response technique to investigate the RTD characteristics of three different microreactors and found that in a split-and-recombine reactor, the RTD was significantly narrowed in a broader flow rate range due to effective convective mixing.

### **Decoupling between the reaction mixture and the wall**

The interaction between the reactants and the wall surface is strictly suppressed since the wall is wetted by the carrier liquid. In this case, the reaction solution forms high contact angles with the wall or it is completely released from the surface. Consequently, the nucleation at the wall, the adsorption of nanoparticles, film formation at the wall surface and blocking of the channel can be avoided.

### **Small reaction volume**

Microfluidics can be used to handle small volumes of fluids (typically on the picoliter to nanoliter scale). The benefits from miniaturization include low reagent consumption and reduced exposure to toxic or hazardous materials. In micro segmented flow, the reaction is confined to a single segment, allowing even smaller reagent volume and reaction time [111]. Moreover, the small reaction volumes combined with the high heat and mass transfer rates enable reactions under more aggressive conditions with higher yields than typically achieved with conventional reactors [128].

### **Faster development**

An increase in throughput of microreactors from lab to bulk production can be achieved by running a large number of identical microdevices under the same conditions according to the number-up approach [121] rather than by scale up. There are a lot of further advantages of the numbering-up concept. Research results can be faster transferred into production, plants can be constructed in a shorter time and the production capacity can be adjusted more flexibly to variations in demand [129]. Importantly, the system is easy to maintain and can be operated

continuously under safe conditions [130]. Chambers *et al.* [131] have developed a gas-liquid multi-channel microreactor for fluorination of ethyl acetoacetate on a large scale. By scale-out, 10 two-sided 30-channel reactors would provide about 3 kg of product per day.

### 1.2.3 Applications of micro segmented flow

Segmented based microfluidics has been applied to many chemical and biological reactions. In the following section, recent work mainly on synthesis of polymer and inorganic particles are reviewed.

#### Micro segmented flow synthesis of polymer particles

Polymer particles with uniform size distribution have been used for diverse applications in drug delivery, electronics and biomedical devices. Compared to conventional processes, microfluidic synthesis enables the preparation of polymer particles with improved control over their size, size distribution, shape and composition [132]. A number of recent reviews have presented an extensive overview of the latest progress in microfluidics-assisted synthesis of polymer particles [94, 132-135].

Microfluidics emulsification can be realized via different microsystems such as T-junction [136], flow-focusing devices [137], terrace-like microchannel devices [138] and capillary-based devices [139-140]. Photo-initiated polymerization [137] and solvent extraction/evaporation methods [141-142] offer convenient ways to produce particles in microfluidic devices. This technology allows to create polymer particles with a wide range of morphologies, including Janus particles, non-spherical particles and double emulsions. Recently, Kumacheva and coworkers [137] have generated Janus droplets in a microfluidic flow focusing device. The formed droplets were exposed to UV light to create Janus polymer particles (Fig. 1.8a, b). With this method, the structure of Janus particles can be controlled precisely. The combination of flow focusing and alteration of channel geometry permitted the generation of polymer particles with unique shapes: spheres, rods, disks and ellipsoids (Fig. 1.8c-e) [143]. Kim. *et al.* [144] have used a glass capillary device to prepare highly interesting double emulsions with different number of aqueous cores and photocurable resin shell (Fig. 1.8f-h). The composite particles exhibited distinct diffraction color patterns in the visible range, which can last for at least 3 months.

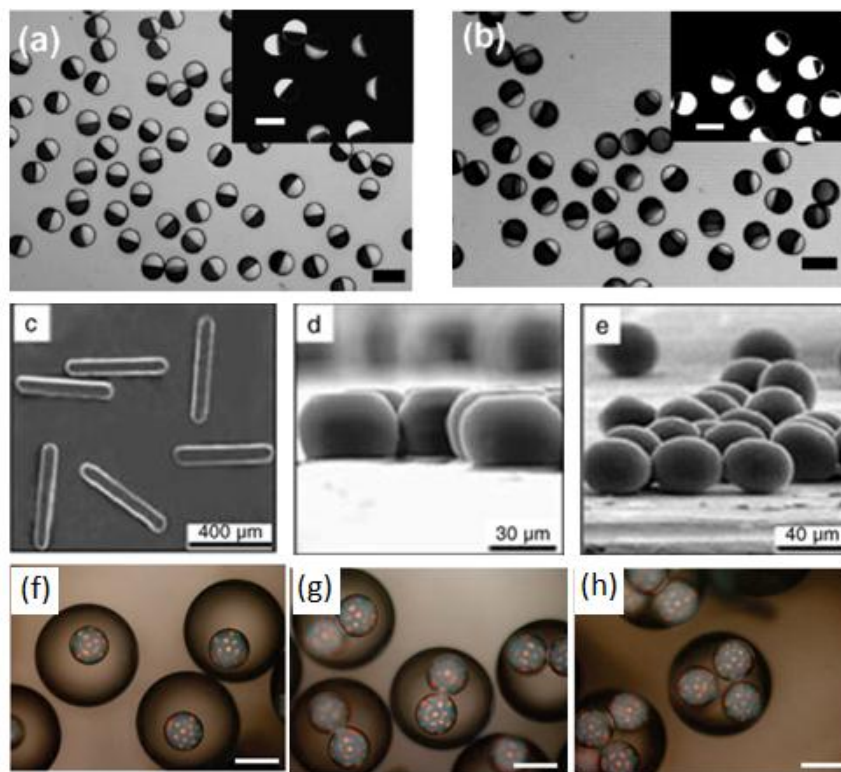


**Fig. 1.8** Optical microscopy images of (a, b) Janus particles [137], (c-e) polymer particles with different shapes [143] and (f-h) core-shell microparticles with different number of cores [144].

### Micro segmented flow synthesis of inorganic particles

Segmented based microfluidics is a rapidly growing area and it has been intensively employed for synthesis of a wide range of nanoparticles, such as metal, metal oxide and semiconductor nanoparticles. Duraiswamy *et al.* [145] have presented a droplet-based microfluidic method for the preparation of anisotropic gold nanocrystal dispersions (Fig. 1.9a). The shapes of the gold nanoparticles can be changed from spherical, rod-like to sharp-edged by tuning the flow rates of fluid streams (Fig. 1.9a<sub>1</sub>-a<sub>3</sub>). A. Knauer *et al.* have used a two-step micro continuous flow-through method to synthesize Au/Ag core/shell and Au/Ag/Au double shell nanoparticles with very narrow size distribution [146]. Ismagilov and coworkers [147] have reported a plug-based microfluidic method for CdS and CdS/CdSe semiconductor nanoparticle synthesis within millisecond time-control. The microfluidic device is shown in Fig. 1.9b. Frenz *et al.* [148] have used a droplet-based microreactor to prepare magnetic iron oxide nanoparticles with diameter of 4 nm. In all of these studies, enhanced segment-internal mixing and reduced residence time distributions result in improved particle size distribution.

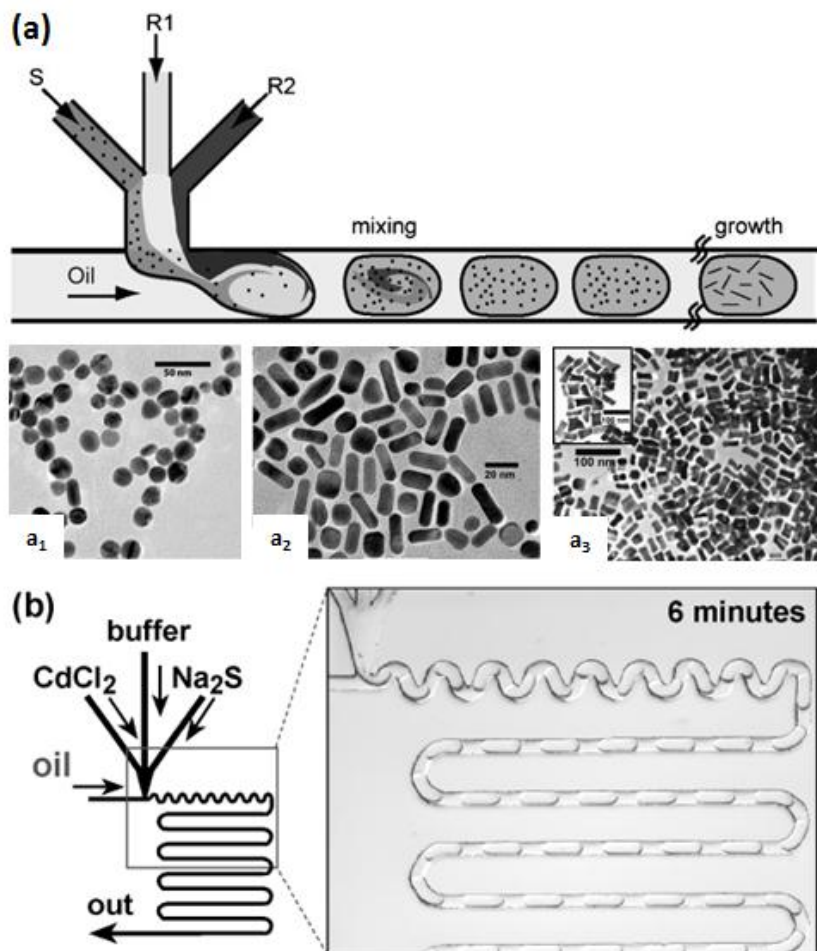


**Fig. 1.9** (a) A droplet-based microfluidics T-junction used for synthesis of gold nanoparticles. An aqueous gold nanoparticles seed suspension (S) and aqueous reagent solutions (R1 and R2) are separately delivered into one arm of a microfluidic T-junction [145]; (a<sub>1</sub>-a<sub>3</sub>) TEM images of gold particles with spherical, rod and sharp-edged gold nanoparticles [145]; (b) Schematic diagram and micrograph of a microfluidic device for CdS and CdS/CdSe nanoparticles synthesis within millisecond time control [147].

### 1.3 Aim and objective

As mentioned in section 1.1, ZnO micro and nanoparticles have generated a great deal of interest due to their potential applications. The production of high quality ZnO particles with well-defined size, size distribution and morphology becomes increasingly important because their specific physical and chemical properties strongly depend on particle geometry. Although many different techniques have been developed to synthesize ZnO particles, most preparations are carried out in batch and required either long reaction time or high reaction temperature. In comparison, the micro segmented flow technique offers several advantages, for example, short diffusion paths, fast mixing and high heat exchange rate, which can remarkably improve the process control in chemical reactions. Consequently, it allows the continuous discovery and development of new products with higher yield and lower consumption of resources. In addition, for industrial applications, it would be interesting to transfer batch methods into a continuous synthesis.

To the best of our knowledge, there has been no report about micro segmented flow synthesis of ZnO micro and nanoparticles so far. Therefore, the aim of this doctoral work is to investigate the application of micro segmented flow technique for the formation of ZnO micro and nanoparticles and also produce ZnO particles with improved homogeneity benefiting from micro reaction technology. Consequently, this research should follow the tasks listed below:

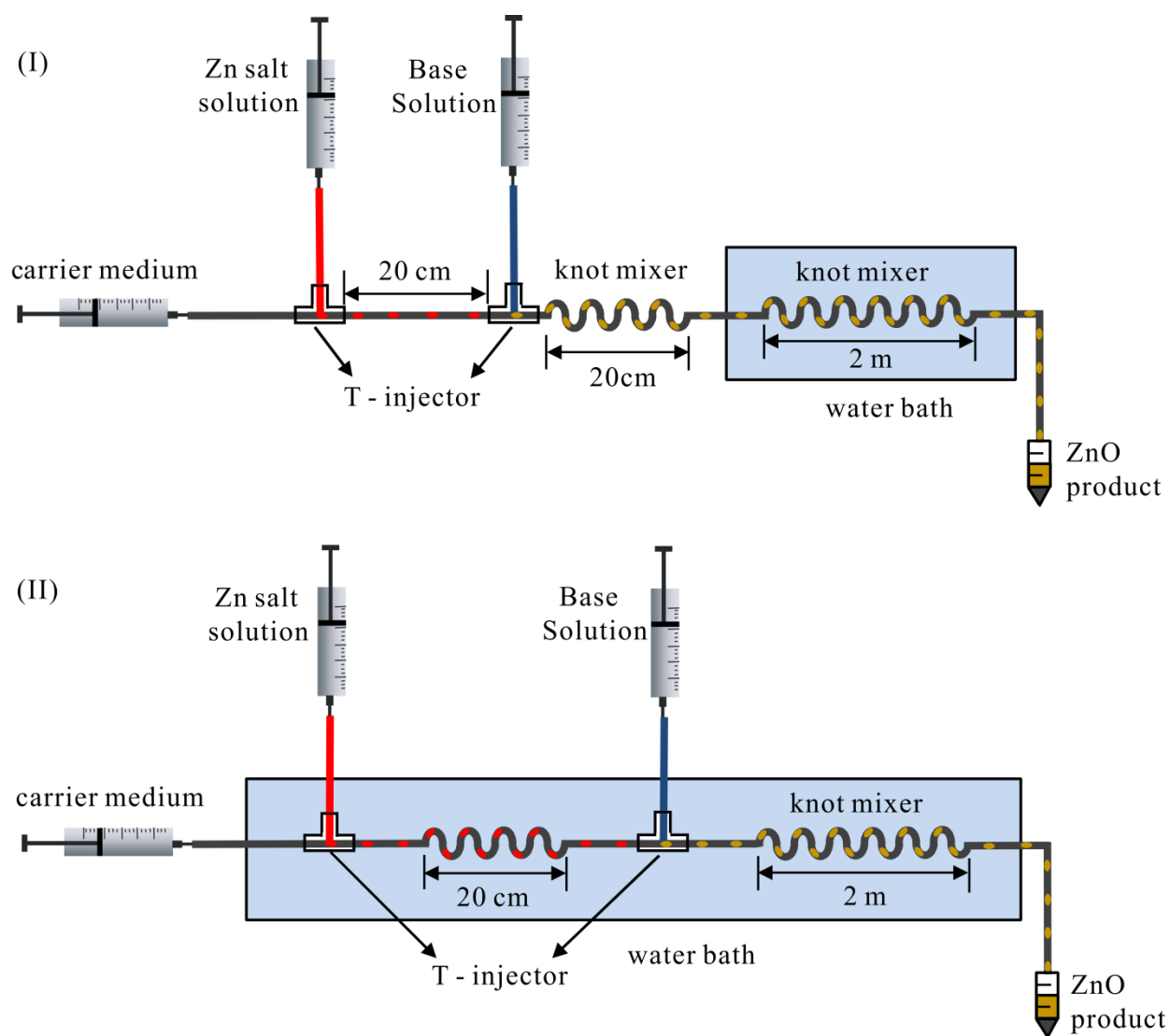
- Selection of the microfluidic components for a laboratory micro reaction system
- Development and optimization of the microfluidic set-ups
- Characterization of the microfluidic system and the micro segmented flow
- Test and selection of batch experimental methods for ZnO particles synthesis
- Adaption of the optimized batch protocols to micro segmented flow system
- Variation of the flow conditions for reproducible production of ZnO particles with high homogeneity
- Optimization of the experimental parameters for preparation of ZnO particles with different shape and size
- Characterization of the produced particles to investigate their size, shape, optical properties and local structure properties

## 2 Materials and methods

### 2.1 Microfluidic systems for synthesis of ZnO particles

As discussed in section 1.3, a laboratory micro reaction system should be built for generation and modification of ZnO particles. For this aim, four different experimental set-ups have been developed, which will be described in detail below.

#### Microfluidic system A: working temperature below 100 °C

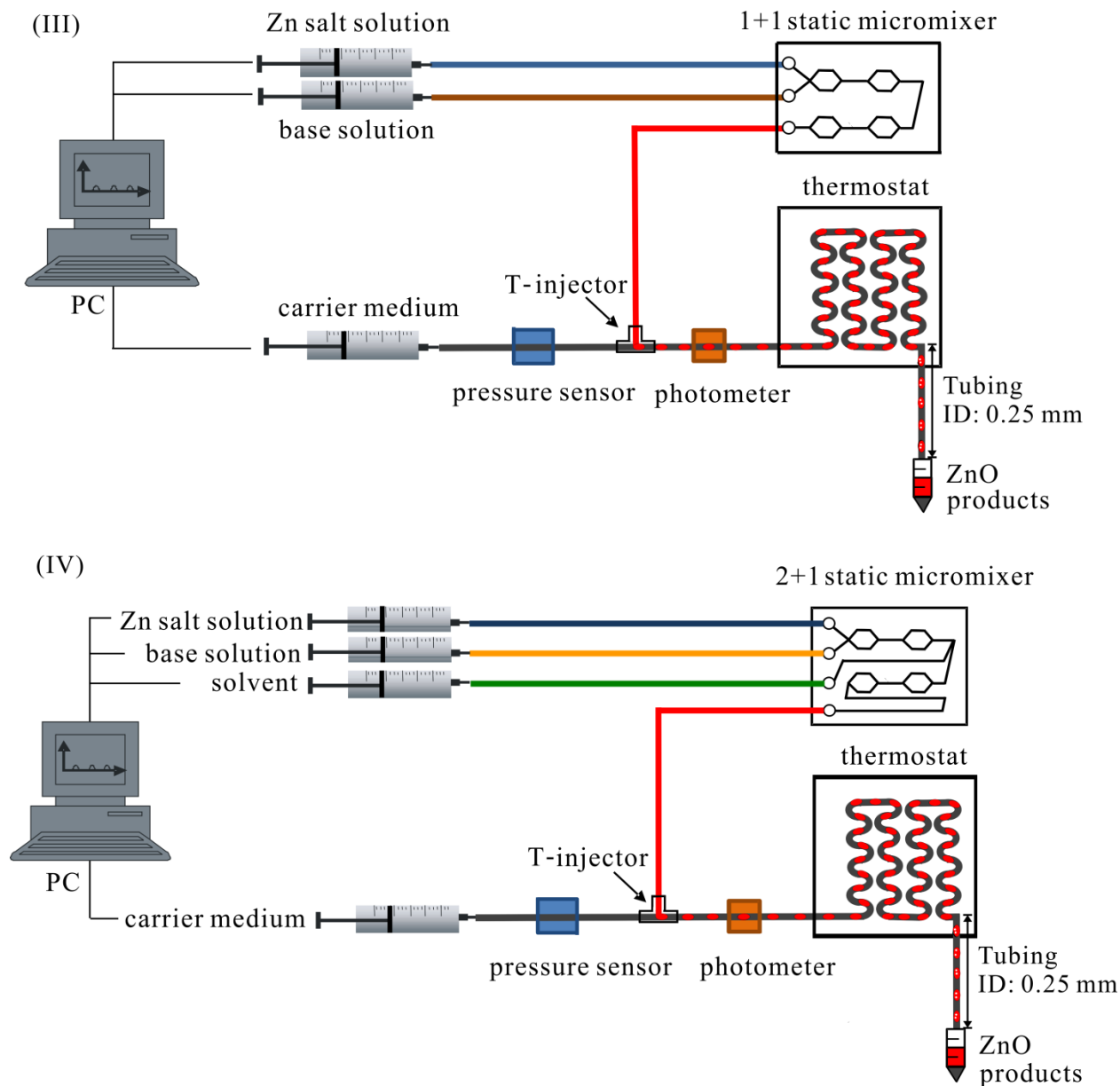


**Fig. 2.1** Microfluidic arrangements used for continuous synthesis of ZnO particles below 100 °C: (I) set-up for homogeneous mixing conditions; (II) set-up for homogeneous thermal reaction conditions.

Two microfluidic arrangements for synthesis of ZnO particles below 100 °C are shown in Fig. 2.1. Both experimental set-ups had three computer-controlled syringe pumps (TSE Systems, [www.tse-systems.com](http://www.tse-systems.com)) including plastic syringes (B. Braun Melsungen AG, Germany, [www.bbraun.de](http://www.bbraun.de)) with volumes of 5 mL for the reactants and 10 mL for the carrier liquid. Two ETFE injectors (P-632 Tee Assy Tefzel 1/16", Besta-Technik GmbH) were used for segment formation (the first injector) and dosing reactant (the second injector). PTFE knot mixers (ID: 0.5 mm, Bohlender GmbH, Germany, [www.bola.de](http://www.bola.de)) were applied to enhance the segment-internal convection in order to improve the heat transfer inside the segments. The reaction was initiated by placing the knot mixers into a commercial water bath thermostat (Thermo Haake, P5) at temperature below 100 °C. The tubes and the injectors were compatible with the used chemicals and the high pH value.

The difference between these two set-ups lies in the order of mixing and heating. In the first set-up (Fig. 2.1I), the reactants were brought together before increasing the temperature. The formation of fluid segments was realized by injection of the first reaction solution into a stream of carrier liquid (tetradecane or perfluoromethyldecalin) and the addition of the second reactant solution occurred outside the water bath at room temperature. One advantage of this set-up is the homogenization of concentration inside the segments before the initiation of ZnO formation at elevated temperature. The disadvantage of this arrangement is given by the fact that temperature gradients arise from conduction of the segments through the water bath.

The second micro segmented flow arrangement was designed in order to achieve the best conditions for heat transfer (Fig. 2.1II). All process steps, including initial segment formation, mixing and reaction activation, were carried out together inside the water bath at elevated temperature. One advantage of this arrangement is the homogenous temperature distribution during the mixing of reactants. In contrast to the first set-up, concentration gradients occur during the start of reaction since the mixing takes place at reaction temperature.

**Microfluidic system B: working temperature up to 150 °C**

**Fig. 2.2** Microfluidic arrangements used for continuous synthesis of ZnO micro and nanoparticles at temperature up to 150 °C with 1+1 static micromixer (III) and 2+1 static micromixer (IV).

The synthesis of ZnO particles at temperature up to 150 °C was achieved by the following multistep micro continuous flow processes using set-up III and IV (Fig. 2.2):

- (1) Homogeneous mixing of the reactant solutions by a static micro mixer
- (2) Formation of segmented flow by injection of the reaction mixture into a carrier stream of

tetradecane or perfluoromethyldecalin (PP9)

(3) Reaction initiation by fast heating in a thermostat

(4) Particle growth in a final residence loop

The biggest difference between these two microfluidic systems is the application of a static micromixer in the microfluidic system B. The static micromixer was used to achieve a fast, uniform mixing of the reactants before the formation of the segments. Kirner *et. al* [149] have reported that this type of static micromixer possesses good mixing efficiency because the split and recombine units facilitate an efficient interdiffusion of the educts. As described previously [150], this device was prepared by silicon/glass technology using thin film deposition and micro-lithographic patterning. It consists of a three-layer arrangement (glass/Si/glass). The detailed construction and preparation technology of the static micromixer is described in reference [149].

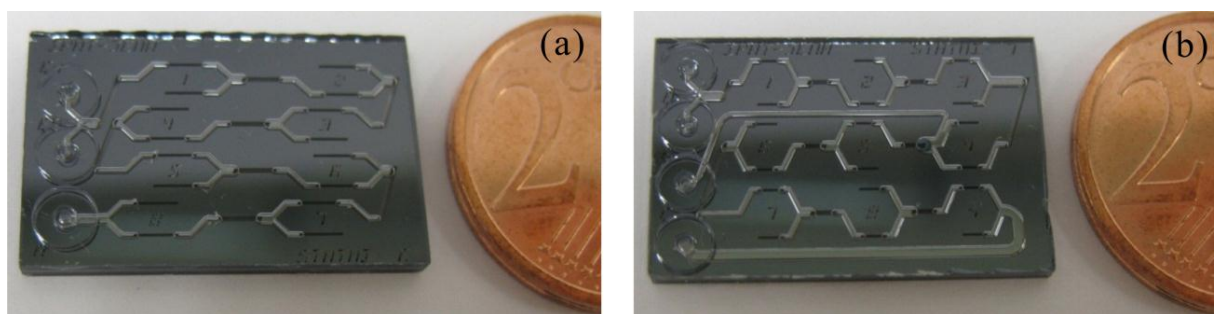


**Fig. 2.3** Images of (a) 1+1 static micromixer and (b) 2+1 static micromixer.

Both chips used in this work were fabricated by the Institute of Photonic Technology (IPHT), Jena. These two devices have the same chip format, but they are distinguished by the number of fluid ports as well as the number and arrangement of the mixing units. The chip size is 22 mm  $\times$  14 mm. The flow channels possess a channel width of 178  $\mu\text{m}$ -700  $\mu\text{m}$  and a channel depth of 160  $\mu\text{m}$ . The chip reactor can be connected to the syringe via flexible PTFE tubing. The 1+1 static micromixer in Fig. 2.3a (Statmix 6, IPHT Jena) includes three fluid ports and eight split-and-recombine units. The internal volume of the chip device including the fluid interconnectors amounts to about 8.5  $\mu\text{L}$  [151]. While the 2+1 static micromixer in Fig. 2.3b (Statmix 7, IPHT Jena) has three inlets and one outlet. It starts with four split-and-recombine units for both of the first reactants, followed by five split-and-recombine units after the addition of the third reactant stream [152]. The internal volume of this chip is about 10  $\mu\text{L}$ .

Another feature of this microfluidic system is the combined application of the micro flow-through pressure sensor and photometer for the simultaneous detection of the pressure and the segments inside the tube. The pressure sensor (PROFI MESS, PU-02, [www.profiness.de](http://www.profiness.de)) was mounted between the syringe for the carrier medium and the injector. It can measure the pressure inside the microfluidic system up to 40 bar. The scheme of a micro flow-through photometer is shown in Fig. 2.4. A light emitting diode (LED, Agilent, Santa Clara CA, United States) with a peak wavelength of 610 nm was used for the extinction measurement. The incident light was absorbed and scattered by the tube and the fluid segment content inside the tube. The intensity of the transmitted light was detected by a photodiode (Typ SFH 206 K, Siemens, München, Germany). Due to the different refractive index between the carrier medium and the chemicals inside the segments, the segment size, segment distance and segment number can be determined during the experiment.

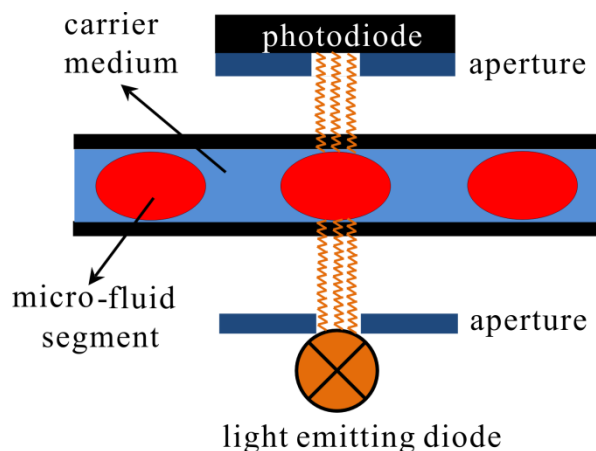


**Fig. 2.4** Scheme of the micro flow-through photometer.

In addition, a thermostat was fabricated in the workshop in the Physics Institute, TU-Ilmenau. It allows the application of temperature up to 150 °C (Fig. 2.5). The dimensions of this thermostat are 10 cm × 10 cm × 10 cm and it is made of aluminum. Two static micromixers and one T-injector can be mounted on its surface. In this work, PTFE tube coils (Bohlender GmbH, Germany, [www.bola.de](http://www.bola.de)) with inner diameter of 1 mm and length of around 1 m were placed inside the thermostat. The winding channels in the thermostat can enhance the internal mixing and heat transfer within the segments.

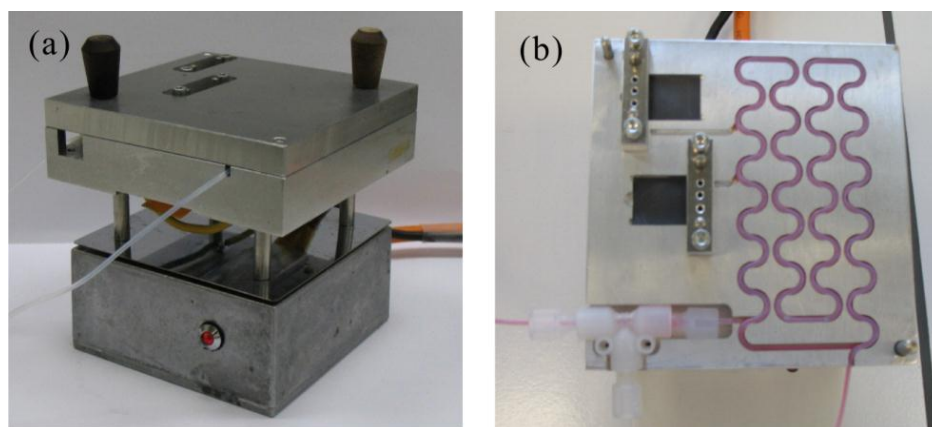


**Fig. 2.5** Images of the thermostat: (a) general view; (b) top view without lid.

Besides, this microfluidic system contained three or four computer-controlled syringe pumps (TSE Systems, [www.tse-systems.com](http://www.tse-systems.com)) and glass syringes (SGE, Australia, [www.sge.com](http://www.sge.com)) with volumes of 5 mL for the reactants and 10 mL for the carrier liquid. The use of a valve or connection to a smaller diameter tube (ID: 0.25 mm, IDEX Health & Science, [www.idex-hs.com](http://www.idex-hs.com)) allowed the application of reaction temperature above the boiling point of the solvent. Therefore, the continuous-flow hydrothermal synthesis can be executed up to 150 °C.

## 2.2 Particle synthesis

### 2.2.1 ZnO micro and nanoparticles

ZnO micro and nanoparticles were prepared by micro segmented flow synthesis. The corresponding microfluidic arrangements have been discussed in section 2.1. Zinc salt and base in different solvents were used as reactants. The flow conditions and experimental parameters were adjusted to produce ZnO particles with controlled shape and size. The total flow rates with corresponding velocities and the total residence time used for ZnO synthesis are summarized in Table 2.1. Detailed experimental conditions are described in Chapter 3.

**Table 2.1** The total flow rates with corresponding velocities and total residence time used for ZnO synthesis.

Set-up	Total flow rate	Velocity	Total residence time
I, II	100 $\mu\text{L}/\text{min}$	0.5 m/min	236 s
	200 $\mu\text{L}/\text{min}$	1.0 m/min	118 s
	1000 $\mu\text{L}/\text{min}$	5.1 m/min	24 s
	5000 $\mu\text{L}/\text{min}$	25.5 m/min	5 s
III	1000 $\mu\text{L}/\text{min}$	1.3 m/min	48 s
	2200 $\mu\text{L}/\text{min}$	2.8 m/min	22 s
	5000 $\mu\text{L}/\text{min}$	6.4 m/min	9 s
IV	650 $\mu\text{L}/\text{min}$	0.8 m/min	76 s
	5000 $\mu\text{L}/\text{min}$	6.4 m/min	9 s

### 2.2.2 Au nanoparticles

Au nanoparticles were prepared by using the Turkevich method [153-154], in which a mixture of 1 mL 0.5 mM  $\text{HAuCl}_4$  and 1 mL 1.7 mM trisodium citrate solution was heated to boiling in a capped glass bottle under vigorous stirring. After boiling for 3 min, the solution was kept stirring

without heating until it cooled to room temperature. The obtained Au nanoparticles solution revealed a wine-red color and showed an absorption maximum at 518 nm. The DCS spectrum has determined that the obtained Au nanoparticles had a mean diameter of 12.0 nm with a size distribution of 2.7 nm.

### **2.2.3 ZnO/Au composite particles**

ZnO/Au composite particles were synthesized by growth of Au nanoparticles on ZnO particles according to previous publications [155-156]. The prepared ZnO particles in ethanol were first dispersed in diluted sodium citrate solution and then centrifuged and washed with diluted sodium citrate solution several times. Then 1.6 mg of washed ZnO particles were mixed with 3.6 mL 1 mM of sodium citrate solution followed by dropwise addition of 1 mM HAuCl<sub>4</sub> under vigorous stirring. After stirring at room temperature for 40 h, the color of the mixture solution changed to dark blue, which indicated the formation of ZnO/Au composite particles. Finally, the product was centrifuged and washed with distilled water three times. Two different molar ratios of ZnO/Au (10/1 and 25/1) were applied to adjust the surface coverage of Au nanoparticles on ZnO particles.

### **2.2.4 ZnO/4-MBA/Au composite particles**

First, 41 mg of prepared ZnO particles were immersed in 3 mL 5 mM of 4-mercaptobenzoic acid (4-MBA) ethanol solution and stirred for 3 h at room temperature. The product was centrifuged and rinsed with ethanol and deionized water to obtain 4-MBA modified ZnO particles (ZnO/4-MBA). Then the ZnO/4-MBA particles were dispersed in synthesized Au nanoparticles solution, stirred for 1 h at room temperature and finally rinsed three times with deionized water to obtain ZnO/4-MBA/Au composites. In order to control the surface coverage of Au nanoparticles on ZnO/4-MBA particles, three different molar ratios of ZnO/Au (10/1, 20/1 and 40/1) were applied.

### 2.3 Chemicals

In this work, all chemicals were used as received without further purification as shown in Table 2.2. Deionised water (Aqua purificator G 7795, Miele, Germany) was used for all preparations.

**Table 2.2** List of chemicals used for the experiments.

Chemical name	Abbreviation/ Chemical formula	Company and purity/concentration
4-Aminothiophenol	C <sub>6</sub> H <sub>7</sub> NS	Merck, Germany; 97 %
Boron nitride	BN	Aldrich, USA; 99 %
Dimethyl sulfoxide	DMSO	Carl Roth GmbH, Germany; 99.5 %
Ethanol	EtOH	Merck, Germany; 99.9 %
Ethylenediamine	EDA	Acros organics, USA; 99 %
Ethylene glycol	EG	Acros Organics, USA; 99.97 %
Isopropanol	IPA	Fischer Scientific, UK; 99.9 %
Lithium hydroxide	LiOH	Alfa Aesar, Germany, 99.995 %
Perfluoromethyldecalin	PP9	F2 Chemical Ltd, UK
Polyacrylamide (MW 10 000)	PAM	Sigma Aldrich, USA; 50 wt% in H <sub>2</sub> O
Polyethylene glycol (MW 600)	PEG	Merck, Germany
Potassium carbonate	K <sub>2</sub> CO <sub>3</sub>	Merck, Germany; 99 %
Silver nitrate	AgNO <sub>3</sub>	Merck, Germany; 99 %
Sodium borohydride	NaBH <sub>4</sub>	Merck, Germany
Sodium hydroxide	NaOH	Merck, Germany; 99 %
Tetrachloroauric acid trihydrate	HAuCl <sub>4</sub> · 3H <sub>2</sub> O	Carl Roth GmbH, Germany; 99.5 %
Tetradecane	TD	Acros Organics, USA; 99 %
Tetramethylammonium hydroxide in isopropanol/methanol	TMAH	Merck, Germany; 0.1 M
Triethanolamine	TEA	Acros Organics, USA; 99 %

Trisodium citrate	$\text{Na}_3\text{C}_6\text{H}_5\text{O}_7$	Merck, Germany; 99 %
Zinc acetate dihydrate	$\text{Zn}(\text{Ac})_2 \cdot 2\text{H}_2\text{O}$	Acros Organics, USA; 98 %
Zinc oxide	$\text{ZnO}$	Aldrich, USA; 99.99 %

## 2.4 Characterization

In this section, a brief description of different techniques used to characterize the synthesized particles is given. Generally speaking, ultraviolet/visible (UV/Vis) spectroscopy and photoluminescence (PL) spectra are used to measure the absorption spectra and emission/excitation spectra of the synthesized particles, respectively. The shape and size of the formed particles is determined by scanning electron microscope (SEM) and transmission electron microscope (TEM). Differential centrifugal sedimentation (DCS) and small angle X-ray scattering (SAXS) are used to measure the size and size distribution of nanoparticles. X-ray diffraction (XRD) and X-ray absorption spectroscopy (XAS) are applied to investigate the crystal structure and local atomic structures of the formed particles, respectively. In addition, the weight changes of the formed particles and the molecules on metal or semiconductor surfaces are investigated by thermogravimetric analysis (TGA) and Raman spectroscopy, respectively.

### 2.4.1 pH meter

The pH value of the product solutions after synthesis was measured by a cyberscan PC 510 Bench pH meter (EUTECH instruments, [www.eutechinst.com](http://www.eutechinst.com)) with pH electrode.

### 2.4.2 UV/Vis spectroscopy

UV/Vis spectroscopy is a technique for chemical and structure analysis in the ultraviolet-visible region (generally from 200 nm to 800 nm). The basic parts of the spectrometer are a light source, a sample holder, a monochromator and a detector. It measures the intensity ( $I$ ) of the light passing through a sample and compares it to the intensity ( $I_0$ ) of the incident light. The ratio of  $I/I_0$  is called the transmittance. This method is often used to quantitatively determine the concentration of a sample based on Beer-Lambert's law:

$$A = \log_{10}(I/I_0) = \varepsilon \cdot c \cdot L \quad (2.1)$$

where  $A$  is the measured absorbance,  $\varepsilon$  the molar absorptivity,  $c$  the concentration of the absorbing species, and  $L$  the path length of the cuvette or sample holder.

In this work, the absorption spectra of Au and ZnO particles were recorded by a double beam UV/Vis spectrophotometer (Specord 200, Analytik Jena, Germany) with scanning speed of 10

nm/s over a scanning wavelength range of 200-800 nm.

### **2.4.3 Photoluminescence (PL) spectroscopy**

PL spectroscopy is a contactless, nondestructive method used to analyze the electronic structures of materials. In general, the process of PL involves a material that absorbs photons with energy greater than that of the material band gap. The absorbed photons excite the electrons in the sample to a higher energy level. Then the electrons return to a lower energy state accompanied by the emission of photons. The emitted photons are photoluminescence. Features in the emission spectra can be used to identify surface, interface, and impurity levels of the samples [157]. Typical applications of this technique include band gap determination, defect detection and analysis of recombination mechanisms.

In this study, photoluminescence (PL) spectra were measured with a Jasco FP-6200 Spectrofluorometer at room temperature.

### **2.4.4 Scanning electron microscopy (SEM)**

SEM is an instrument that scans a sample surface with a high-energy electron beam in a vacuum chamber. The electron beam comes typically from a tungsten filament and has energy from 0.5 keV to 40 keV. When the electron beam strikes the sample, the electrons interact with the atoms and emit signals that contain information about the sample. The most common used signals are the secondary electrons (SE), the backscattered electrons (BSE) and X-rays. The SE signal comprises essential information on the morphology and topography of the samples. The BSE signal is most valuable for illustrating the contrasts in composition in multiphase samples. The characteristic X-rays are mainly used for elemental analysis. Almost all solid surfaces can be analyzed by SEM. It has a large depth of field, which allows more of a sample to be in focus at one time. The SEM also can produce images with high spatial resolution, which means that closely spaced features can be examined at high magnification. All of these advantages have made SEM one of the most useful instruments in different research areas today.

In this work, SEM (JEOL JSM-6380) and FE-SEM (Hitachi S-4800) were used to characterize the size and morphology of the synthesized particles. The product solutions were applied on silicon chip, particles were adsorbed and then rinsed with water and ethanol. The average

diameter and aspect ratio of the particles were determined by measuring at least 100 randomly selected particles by use of SEM images. For flower-shaped ZnO particles, the diameters were measured along the longest distance between two branches of the flowers. The number-average diameter ( $D_n$ ), the weight-average diameter ( $D_w$ ), the polydispersity index (PDI), and the coefficient of variation (CV) were calculated using the following formulas [158]:

$$D_n = \frac{\sum_{i=1}^N d_i}{N} \quad D_w = \frac{\sum_{i=1}^N d_i^4}{\sum_{i=1}^N d_i^3} \quad \text{PDI} = \frac{D_w}{D_n} \quad \text{CV} = \frac{\sigma}{\overline{d_n}} \quad (2.2)$$

where  $N$  is the total number of particles counted,  $d_i$  is the diameter of the  $i$ th particles,  $\sigma$  is standard derivation and  $\overline{d_n}$  is the average particle diameter.

#### 2.4.5 Transmission electron microscopy (TEM)

TEM is a microscopy technique where a high-energy electron beam (typically 100-300 KeV) interacts with an ultrathin specimen and transmitted through it. During this process, an image is obtained. Then the magnified image is focused onto an imaging device, such as a fluorescent screen or detected by a sensor such as a CCD camera. Due to the very short wavelength of the electrons given by equation 2.3, today's TEM systems offer a resolutions up to 0.2 nm, and the sample can be magnified between 500 and 500,000 times. This makes TEM a powerful tool for analysis of structure and devices with nanometer scale dimensions.

$$\lambda = \frac{h}{\sqrt{2m_0eV(1 + \frac{eV}{2m_0c^2})}} \quad (2.3)$$

where  $\lambda$  is the electron wavelength,  $h$  is the Planck's constant,  $m_0$  is the rest mass of the electron,  $e$  is the charge of the electron,  $V$  is the acceleration voltage and  $c$  is the speed of light in a vacuum.

In this work, TEM investigations were carried out on a Philips Tecnai S20 or JEOL JEM-2010 transition electron microscope with an accelerating voltage of 200 kV. The average diameter of the particles was determined from the TEM images by the same method as described in 2.4.4.

### 2.4.6 Differential centrifugal sedimentation (DCS)

DCS is a novel and powerful tool to measure the size and size distribution of particles in the range of 0.01  $\mu\text{m}$  to 40  $\mu\text{m}$ . This technique is based on the sedimentation of particles in a fluid. The diameter of the particles can be determined by measuring the time required for the particles to sediment a known distance according to the modified form of Stokes' law:

$$D = \sqrt{\frac{18\eta \ln\left(\frac{R_f}{R_o}\right)}{(\rho_p - \rho_f)\omega^2 t}} \quad (2.4)$$

where  $D$  is the particle diameter,  $\eta$  is the fluid viscosity,  $R_f$  is the final radius of rotation,  $R_o$  is the initial radius of rotation,  $\rho_p$  is the particle density,  $\rho_f$  is the fluid density,  $\omega$  is the rotational velocity,  $t$  is the time required to sediment from  $R_o$  to  $R_f$ .

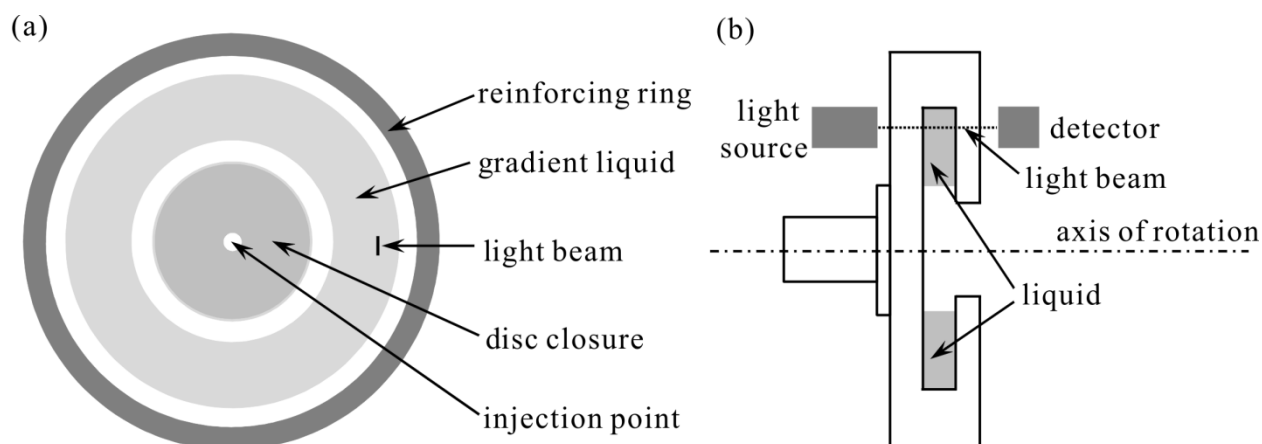


**Fig. 2.6** Scheme of the DCS instrument: (a) Front view of the disc; (b) cross section view of the disc [159].

The most common design for DCS instrument is a hollow, optically clear disc that is driven by a variable speed motor. The scheme of the DCS instrument is shown in Fig. 2.6 [159]. The disc is set in motion at constant speed and then the disc chamber is filled with a fluid which contains a slight density gradient. When particles approach the outside edge of the rotating disc, they scatter a portion of a light beam that passes through the disc. The change in light intensity is continuously recorded and converted by the operating software into a particle size distribution. There are a number of advantages associated with this technique, such as ultra high resolution

capability, high sensitivity, and accurate, reliable and reproducible results. It has been applied for characterization of a wide range of chemical and biological samples.

In this work, the particle size and size distribution of Au and Ag nanoparticles were analyzed by differential centrifugal sedimentation (DCS, DC 20000, CPS Instrument Inc., Newtown, PA, USA).

#### 2.4.7 Small angle X-ray scattering (SAXS)

SAXS is a powerful technique in colloidal science for determining the size, size distribution and shape of nanoparticles in solution. With this technique, different types of samples such as powders, emulsions or liquids can be investigated in the nanometer range. A schematic diagram of a SAXS set-up is shown in Fig. 2.7. A monochromatic beam of X-rays is defined by several pinholes before it hits the sample. Some X-rays are scattered by the sample while most of them go through the sample without interacting with it. The scattering pattern is recorded using an image plate or a 2D detector. It contains the information about the structure of the sample. In a SAXS experiment, the scattered intensity is measured as a function of the scattering vector  $q$ . By plotting  $\ln(I)$  as a function of  $q^2$  at small  $q$  values, the particle size and size distribution can be determined based on the Guinier approximation.

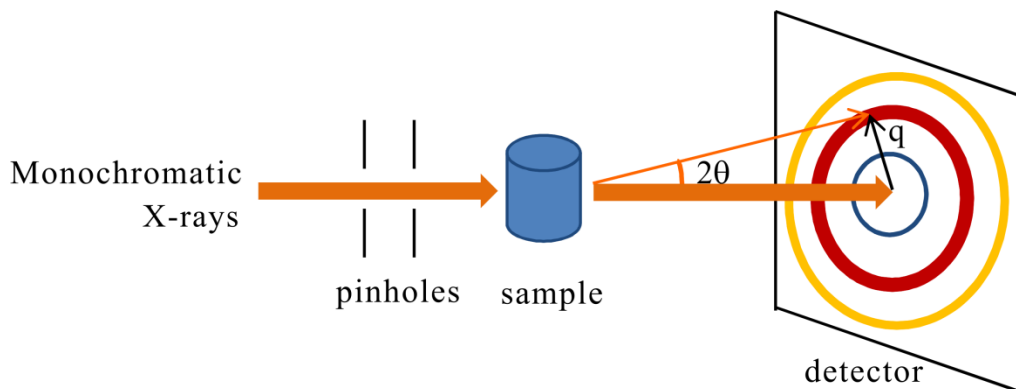


**Fig. 2.7** The schematic diagram of a small angle X-ray scattering experiment.

Although many techniques can be used to characterize the particle size, most of them provide incomplete structural information. For example, TEM only probes a small number of particles and is subject to sample preparation; dynamic light scattering and atomic force morphology (AFM) do not measure the core diameter directly [160]. In comparison, SAXS benefits from

deriving quantitative information from a statistically significant population of particles at one time [161]. It has proved to be a fast and precise method for determining particle sizes and size distributions.

In this work, SAXS measurements were carried out at the Center for Advanced Microstructures and Devices (CAMD), Louisiana State University, Baton Rouge, Louisiana, USA, using bending magnet radiation and a LNLS (Laboratorio Nacional de Luz Sincrotron, Brazil) double crystal monochromator. The wavelength of the monochromatic light was 1.55 Å. The samples in ethanol were sealed in glass capillaries purchased from Charles Supper Company (www.charles-supper.com) with an outside diameter of 1.0 mm and wall thickness of 10 µm. The scattering pattern was acquired with a two-dimensional Gabriel type multiwire gas detector with a 200 mm active diameter and a resolution of 200-250 µm fwhm in a 1024×1024 array. During the measurements, the sample and the detector chamber were kept under vacuum to minimize background scattering. Scattering intensities were acquired in a  $q$  range from 0.0066 Å<sup>-1</sup> to 0.164 Å<sup>-1</sup>. The scattering of a solvent-filled capillary was subtracted from these curves.

SAXS data were processed using the IGOR Pro v. 6.03A software. Normalized solvent plots were subtracted from corresponding ZnO nanoparticles scattering curves. In order to evaluate the size of particles, the Guinier approximation was applied to the SAXS data.

#### **2.4.8 X-ray diffraction (XRD)**

XRD is one of the most important tools used in solid state chemistry and materials science. It is a non-destructive technique for qualitative and quantitative analysis of crystalline compounds and for the determination of their structural properties. A schematic diagram of an XRD set-up is shown in Fig. 2.8. X-rays are generated in a sealed tube under vacuum or in a storage ring. When the X-ray beam hits the sample, the crystal lattice diffracts the X-rays in certain directions. A movable detector scans the diffraction pattern. In normal mode, the detector is set to scan over a  $2\theta$  range of 5° to 70° at a constant angular velocity. The relationship between the angle of diffraction and the distance between the individual lattice planes is described by Bragg's law:

$$n\lambda = 2d\sin\theta \tag{2.5}$$

where  $n$  is an integer number (order of the diffraction peak),  $\lambda$  the wavelength of the incident X-

rays,  $d$  the spacing between the planes in the crystal lattice, and  $\theta$  the scattering angle.

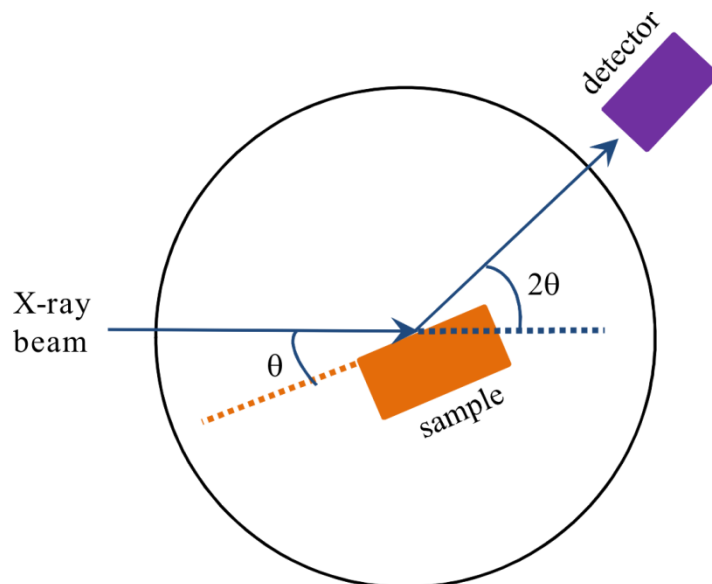


**Fig. 2.8** A schematic diagram of an XRD set-up.

In this work, XRD analysis was carried out on a Siemens D-5000 X-ray diffractometer using  $\text{Cu-K}\alpha$  radiation ( $\lambda = 0.15478 \text{ nm}$ ) with a step size of  $0.02^\circ$ .

### 2.4.9 X-ray absorption spectroscopy (XAS)

X-ray absorption spectroscopy (XAS) includes both X-ray absorption near edge structure (XANES) and extended X-ray absorption fine structure (EXAFS). XANES can determine the valence state and coordination geometry of the absorbing atom. EXAFS can be used to determine the distance between the absorbing atom and the neighboring atoms as well as the types and numbers of atoms in different coordination shells. XRD measurements can also reveal the structure of crystalline material, but it relies on long range order to detect crystalline structures at a length scale of around 5 nm or more. EXAFS can analyze the environment of the selected element within 6 Å [162]. For most systems, the application of XRD and XAS is complementary.

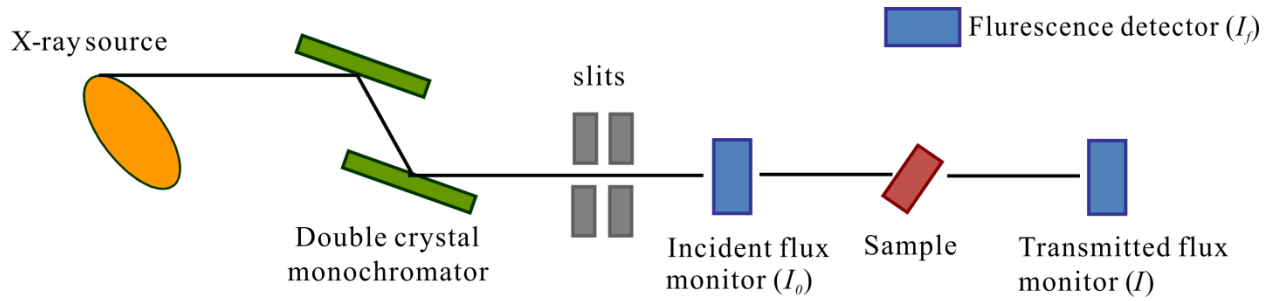


**Fig. 2.9** A schematic diagram of a typical XAS experiment set-up.

A schematic diagram of a XAS experimental set-up is shown in Fig. 2.9. The broad electromagnetic spectrum from a synchrotron is monochromatized using a double crystal monochromator (DCM) based on Bragg's law (2.4). Slits are used to define the beam. XAS can be measured in two different ways: in transmission mode, the intensity of the X-ray beam is measured before ( $I_0$ ) and after passing through the sample ( $I$ ) by using ion chamber gas detectors; in fluorescence mode, the fluorescence radiation ( $I_f$ ) from the sample is measured. If the sample has uniform thickness, the linear absorption coefficient  $\mu(E)$  for a specific photon energy  $E$  is given by the following equations:

$$\text{Transmission mode: } \mu(E) = \ln\left(\frac{I_0}{I}\right) \quad (2.6)$$

$$\text{Fluorescence mode: } \mu(E) \propto \frac{I_f}{I} \quad (2.7)$$

To analyze modulations in the EXAFS range (well above the absorption edge), the fine structure is extracted and normalized in the following way:

$$\chi(E) = \frac{\mu(E) - \mu_0(E)}{\Delta\mu_0(E_0)} \quad (2.8)$$

where  $\mu(E)$  is the linear absorption coefficient as a function of the photon energy,  $\mu_0(E)$  is a background function representing the absorption by an isolated atom, and  $\Delta\mu_0(E)$  is the measured jump in the absorption  $\mu(E)$  at the absorption edge.

EXAFS is an interference effect and depends on the wave number  $k$  of the photoelectron.

Therefore, it is common to convert the X-ray energy to  $k$ :

$$k = \sqrt{\frac{2m(E - E_0)}{h^2}} \quad (2.9)$$

where  $E_0$  is the absorption edge energy,  $h$  is Planck's constant and  $m$  is the electron mass.

Then the EXAFS data are Fourier transformed to  $r$  space. The peaks in the Fourier transform represent the different shells of scattering atoms. After fitting the experimental data into the theoretical EXAFS calculations, the structure information about the local environment of the absorbing atom can be extracted. More detailed information about XAS can be found in a literature [162-163].

In this work, EXAFS measurements were also taken at CAMD. The storage ring was operated at 1.3 GeV with beam currents between 100 and 200 mA. The measurements were made at the Wiggler Double Crystal Monochromator (WDCM) beamline. The monochromator was equipped with a set of water cooled Ge 220 crystals. The ZnO microparticles powders were ground with boron nitride to optimize the absorption, homogeneously spread on self-adhesive Kapton tape, covered with another layer of Kapton tape and measured in transmission mode with ionization chambers filled with air. Liquid samples (ZnO nanoparticles in ethanol) were dropped on 0.5 cm  $\times$  1.0 cm filter paper. After most of the solvent had evaporated, the filter paper was placed between Kapton tapes and measured in fluorescence mode using a Canberra 13-element germanium solid state detector. Each sample was scanned four times with a 17  $\mu$ m thick Zn foil placed after the sample for calibration. Data reduction was performed using the Athena (v.0.8.061) software package. For data fitting, the WinXAS program was used.

### 2.4.10 Thermogravimetric analysis (TGA)

TGA measures the weight changes of a material as a function of temperature or time under a controlled atmosphere. A TGA normally consists of a precision balance with a pan loaded with the sample. That pan in a furnace is heated or cooled during the experiment. The mass of the sample is monitored during the experiment. TGA is commonly used to determine the composition of materials, degradation temperatures, and to predict their thermal stability at temperatures up to 1000 °C. It can investigate materials that exhibit weight change due to

decomposition, dehydration or oxidation.

In this work, TGA was used to characterize the composition of ZnO particles. It is recorded using Netzsch STA 409 EP from 30 °C to 750 °C with a heating rate of 10 °C/min under flowing air.

#### **2.4.11 Raman spectroscopy**

Raman spectroscopy is a technique for identification and analysis of molecular species. It is based on the detection of the scattered light. Generally speaking, when light interacts with a sample, most of it is elastically scattered (Rayleigh scattering) and the scattered light has the same wavelength as the incident light. However, if the sample relaxes to a vibrational energy level that differs from the initial state, the scattered light is shifted in energy. Such inelastic scattering process is called Raman scattering.

A typical Raman system consists of four major components [164]: (1) excitation source, usually a visible-light laser; (2) optics for sample illumination system and collection of sample-scattered light; (3) a monochromator to select the wavelength; and (4) a signal processing system consisting of a detector and a data processing unit.

Surface enhanced Raman scattering (SERS) is a surface sensitive technique that results in the enhancement of Raman scattering by molecules adsorbed on the surface of colloidal metal surfaces. The enhancement factor can be as much as  $10^{14}$ - $10^{15}$ , which makes this technique sensitive enough to detect single molecules. It also can be used to investigate the vibrational properties of adsorbed molecules yielding structural information on the molecule and its local interactions. The exact reason for such dramatic improvement is still not completely understood. It is now generally accepted that SERS can be explained by two mechanisms [165-167]: the electromagnetic (EM) mechanism and chemical mechanism. The EM mechanism arises from the presence of surface plasmons on the substrate, while the chemical mechanism involves the charge transfer between the molecule and the metal surface.

In this work, the Raman spectra were recorded by using a Jasco RFT-6000 Raman spectrometer with a resolution of  $4\text{ cm}^{-1}$ . The 1064 nm radiation from a Nd:YAG laser was used as excitation source.

### 3 Results and discussion

This chapter mainly presents the results of ZnO micro and nanoparticles synthesized by micro segmented flow technique. The effects of the flow conditions and experimental parameters on the size and shape of the ZnO particles are discussed. The mechanism of formation of ZnO particles under hydrothermal condition is proposed. Furthermore, EXAFS is used to study the local structure of the ZnO micro flowers and nanoparticles. Finally, ZnO composite particles prepared by two different methods are presented.

#### 3.1 Continuous synthesis of ZnO particles by micro segmented flow technique in aqueous and dimethylsulfoxide (DMSO) solutions

In this section, the preparation of ZnO particles carried out both in batch and micro segmented flow systems is described. The optimal batch protocols are adapted to micro segmented flow systems and the effect of the reactant concentration, temperature and flow rates on the formed ZnO particles is investigated.

##### 3.1.1 Batch synthesis of ZnO particles

Batch experiments were carried out by mixing the solutions of 5.0 M NaOH and 0.5 M Zn(Ac)<sub>2</sub> in a glass bottle and then keeping them in a thermostated water bath at 90 °C for 1 h. Two different volume ratios of NaOH/Zn(Ac)<sub>2</sub> were chosen to get two different final concentration ratios.

In the first experiment, a concentration ratio of 5:1 was applied by mixing 0.5 mL 5.0 M NaOH and 1 mL 0.5 M Zn(Ac)<sub>2</sub>. A mixture of board-like particles (Fig. 3.1a) and plate-like particles (Fig. 3.1b) was obtained. In the second experiment, 1 mL 5.0 M NaOH and 1 mL 0.5 M Zn(Ac)<sub>2</sub> were mixed to obtain a final concentration ratio of 10, and it resulted in a significant change in the obtained particles type shown in Fig. 3.1c-e. The shapes of the formed particles include single needles, needle aggregations and stars of rods. Obviously, the enhancement of reactant ratio from 5 to 10 is responsible for the shape of the resulting particles shifting from more plate-like to more rod- and needle-like structures. In addition, the homogeneity of shapes and sizes of particles is also improved at higher reactant ratio.

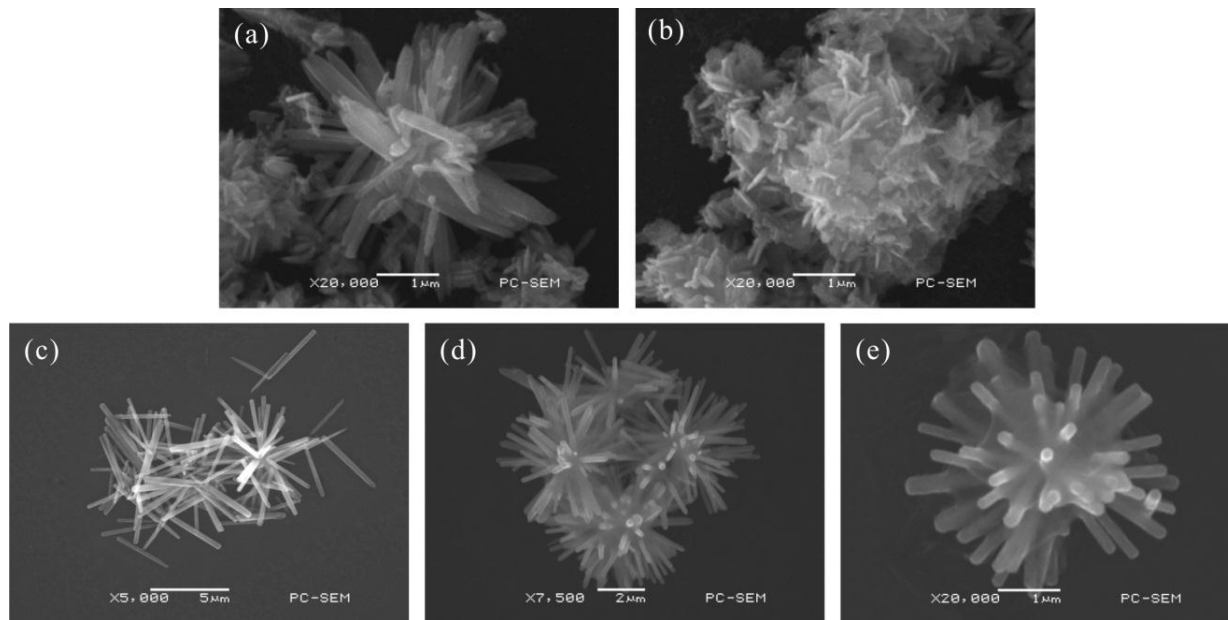


**Fig. 3.1** ZnO particles obtained in batch experiments with different concentration ratios of NaOH/Zn(Ac)<sub>2</sub>: (a, b) 5/1; (c, d, e) 10/1.

### 3.1.2 Micro segmented flow synthesis of ZnO particles in aqueous solution

Micro reaction technology is an interesting alternative to batch synthesis for the generation of particles since the mass and heat transfer rates are limited by the large volumes of conventional reactors. Moreover, the concentration gradients during the mixing and inhomogeneous distribution of temperature can cause a loss of homogeneity during the particles synthesis in batch reactor. In comparison, the micro segmented flow technique can provide much better conditions for fast mass and heat transfer due to high surface area to volume ratios. It allows for an improvement of the parameter control in chemical reactions [142]. Therefore, it is expected that the homogeneity of ZnO particles can be improved if a micro continuous flow process is applied.

Table 3.1 presents the experimental conditions for the preparation of ZnO particles by micro segmented flow synthesis in aqueous solution. The detailed description of the used set-ups is shown in section 2.1. Two different total flow rates (200  $\mu\text{L}/\text{min}$  and 5000  $\mu\text{L}/\text{min}$ ) were applied, and the corresponding residence time was calculated to be 118 s and 5 s, respectively.

**Table 3.1** Experimental conditions for synthesis of ZnO particles in aqueous solution.

Set-up	Zn(Ac) <sub>2</sub>	NaOH	T	Total flow rate	Yield	Product
I	0.1 M	1.0 M	70 °C	200 µL/min	/	Fig. 3.2a
	0.5 M	5.0 M	70 °C	200 µL/min	/	Fig. 3.2b
	0.1 M	1.0 M	90 °C	200 µL/min	73.3 %	Fig. 3.2c
	0.1 M	1.0 M	90 °C	5000 µL/min	80.0 %	Fig. 3.2d
II	0.1 M	1.0 M	70 °C	200 µL/min	64.8 %	Fig. 3.3a
	0.1 M	1.0 M	70 °C	5000 µL/min	70.1 %	Fig. 3.3b
	0.5 M	5.0 M	70 °C	200 µL/min	20.4 %	Fig. 3.3c
	0.5 M	5.0 M	70 °C	5000 µL/min	9.0 %	Fig. 3.3d

The first series of micro flow-through experiments were carried out in set-up I, where the reactant solutions were mixed at room temperature resulting in a concentration ratio of 10:1. Then the fluid segments were conducted through a knot-mixer embedded in a thermostated water bath at lower temperature (70 °C) and lower total flow rate (200 µL/min). In contrast to batch experiments at 90 °C, formation of more compact nanoparticles is observed. At lower concentrations (0.1 M Zn(Ac)<sub>2</sub>, 1 M NaOH), ZnO particles with average diameters of 60 nm and 210 nm were obtained and larger micron particles dominated the product shown in Fig. 3.2a. In comparison, the shape and size of the formed particles dramatically changed if the reactant concentrations were enhanced to 0.5 M Zn(Ac)<sub>2</sub> and 5 M NaOH. As shown in Fig. 3.2b, small compact nanoparticles were dominant besides a few large particles. DCS measurements showed that the mean particle size of the dominating nanoparticles is 23 nm.

In the second experiment, the reactant concentrations and temperature were kept constant (0.1 M Zn(Ac)<sub>2</sub>, 1 M NaOH; 90 °C) and the effect of total flow rate on the formed particles was investigated. As shown in Fig. 3.2c, at lower total flow rate (200 µL/min), the aggregates of small nanoparticles and aggregates of submicron particles were obtained. However, the products became much more regular and homogeneous if the total flow rate was strongly enhanced to 5000 µL/min (Fig. 3.2d). Only a small part of the product was formed as aggregates of small

nanoparticles, but compact particles with an average diameter of 234 nm prevailed in the product. The yield was also enhanced from 73.3 % to 80.0 % when the total flow rate increased from 200  $\mu\text{L}/\text{min}$  to 5000  $\mu\text{L}/\text{min}$ .

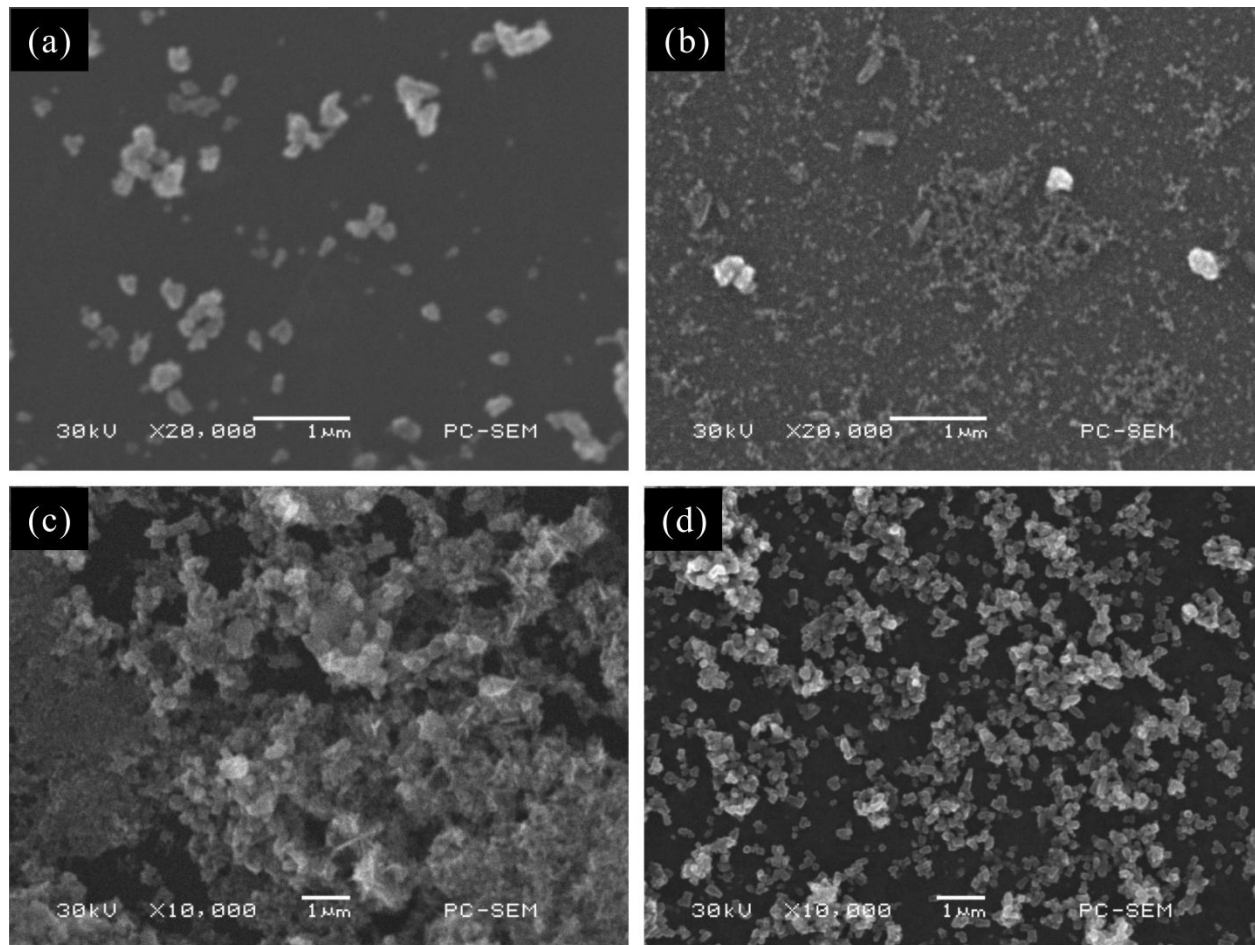


**Fig. 3.2** SEM images of ZnO particles obtained by micro flow-through synthesis with set-up I. (a) 0.1 M  $\text{Zn}(\text{Ac})_2$ , 1.0 M NaOH, 200  $\mu\text{L}/\text{min}$ , 70  $^\circ\text{C}$ ; (b) 0.5 M  $\text{Zn}(\text{Ac})_2$ , 5.0 M NaOH, 200  $\mu\text{L}/\text{min}$ , 70  $^\circ\text{C}$ ; (c) 0.1 M  $\text{Zn}(\text{Ac})_2$ , 1.0 M NaOH, 200  $\mu\text{L}/\text{min}$ , 90  $^\circ\text{C}$ ; (d) 0.1 M  $\text{Zn}(\text{Ac})_2$ , 1.0 M NaOH, 5000  $\mu\text{L}/\text{min}$ , 90  $^\circ\text{C}$ .

An improvement of product homogeneity was found with set-up II at reduced temperature (70  $^\circ\text{C}$ ) if a high flow rate (5000  $\mu\text{L}/\text{min}$ ) was applied. In this case, the reactants were mixed at room temperature by injecting NaOH solution into the segments of  $\text{Zn}(\text{Ac})_2$  solution. The improvement of the product quality at high flow rate was achieved by lower reactant content (0.1 M  $\text{Zn}(\text{Ac})_2$ , 1 M NaOH) and higher reactant concentration (0.5 M  $\text{Zn}(\text{Ac})_2$ , 5 M NaOH). As shown in Fig. 3.3, rather different particle types were synthesized. Flower-like particles with an average diameter of 470 nm were formed at lower concentration (Fig. 3.3b), while spherical aggregations with

diameter of about 1.1  $\mu\text{m}$  composed of needle-shaped particles were obtained at high concentrations (Fig. 3.3d). It can be assumed that the nucleation rate in set-up II is higher than that of set-up I since set-up II provides best conditions for heat transfer. Rapid nucleation rate results in more ZnO nuclei formed at the initial stage. These nuclei may aggregate together, and then each of them individually grows to form flower-like or needle flower-like particles [23].

The comparison between products of synthesis procedures at high and at lower flow rates confirms the high importance of flow conditions. An increase in the flow rate also caused an increase of the yield from 64.8 % to 70.1 % at lower reactant concentration, while a reduction in yield was found under very strong alkaline conditions at enhanced flow rate. The increase of the segment-internal convection could be responsible for the strong influence of flow rate on the quality of ZnO crystals. At a high flow rate, the segment-internal convection is strongly enhanced. This leads to an acceleration of reactant mixing and heat transfer. Therefore, the concentration gradient decreases and homogeneous nucleation can be achieved, which results into regular and uniform products.

#### **3.1.3 Micro segmented flow synthesis of ZnO particles in DMSO solution**

The micro flow-through technique was also tested for the synthesis of ZnO particles in a non-aqueous medium. Accordingly, a mixture of zinc acetate and polyethylene glycol (PEG) in DMSO (molar ratio of  $\text{Zn}^{2+}/\text{PEG} = 2/1$ ) was used as the reactant solution, and a DMSO solution of tetramethylammonium hydroxide (TMAH) and ethylenediamine (EDA) was used as the precipitation agent. The same final concentration of  $\text{Zn}(\text{Ac})_2$  and TMAH (0.05 M) were applied to prepare ZnO in set-up II at 80  $^{\circ}\text{C}$  in a thermostated water bath. The total flow rates used here were 100  $\mu\text{L}/\text{min}$  and 1000  $\mu\text{L}/\text{min}$ , and the corresponding residence time was calculated to be 236 s and 24 s, respectively.

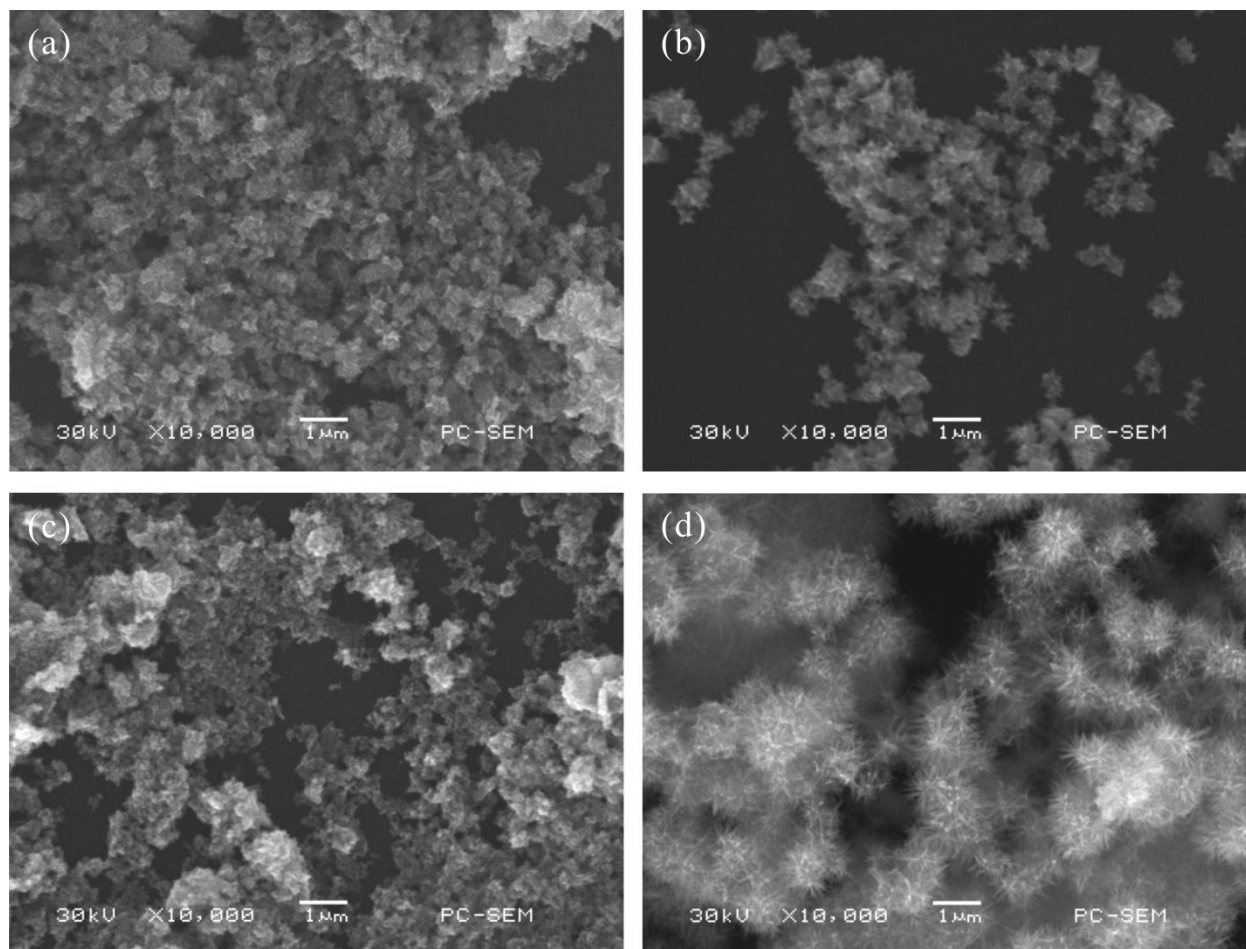


**Fig. 3.3** SEM images of ZnO particles obtained by micro flow-through synthesis with set-up II. (a) 0.1 M  $\text{Zn}(\text{Ac})_2$ , 1.0 M NaOH, 200  $\mu\text{L}/\text{min}$ , 70  $^\circ\text{C}$ ; (b) 0.1 M  $\text{Zn}(\text{Ac})_2$ , 1.0 M NaOH, 5000  $\mu\text{L}/\text{min}$ , 70  $^\circ\text{C}$ ; (c) 0.5 M  $\text{Zn}(\text{Ac})_2$ , 5.0 M NaOH, 200  $\mu\text{L}/\text{min}$ , 70  $^\circ\text{C}$ ; (d) 0.5 M  $\text{Zn}(\text{Ac})_2$ , 5.0 M NaOH, 5000  $\mu\text{L}/\text{min}$ , 70  $^\circ\text{C}$ .

In all the experiments, submicron crystals and aggregates of small spherical nanoparticles were found in the products. The small nanoparticles frequently formed plate-like film fragments with a size of a few microns. The optical properties of the nanoparticles were investigated by fluorescence microscopy and fluorescence spectroscopy. All particles showed a bright yellow fluorescence, which was probably due to the OH-groups in the ZnO crystals typically formed during hydrothermal synthesis [168]. The fluorescence emission band with a maximum at 550 nm was found under 340 nm excitation.

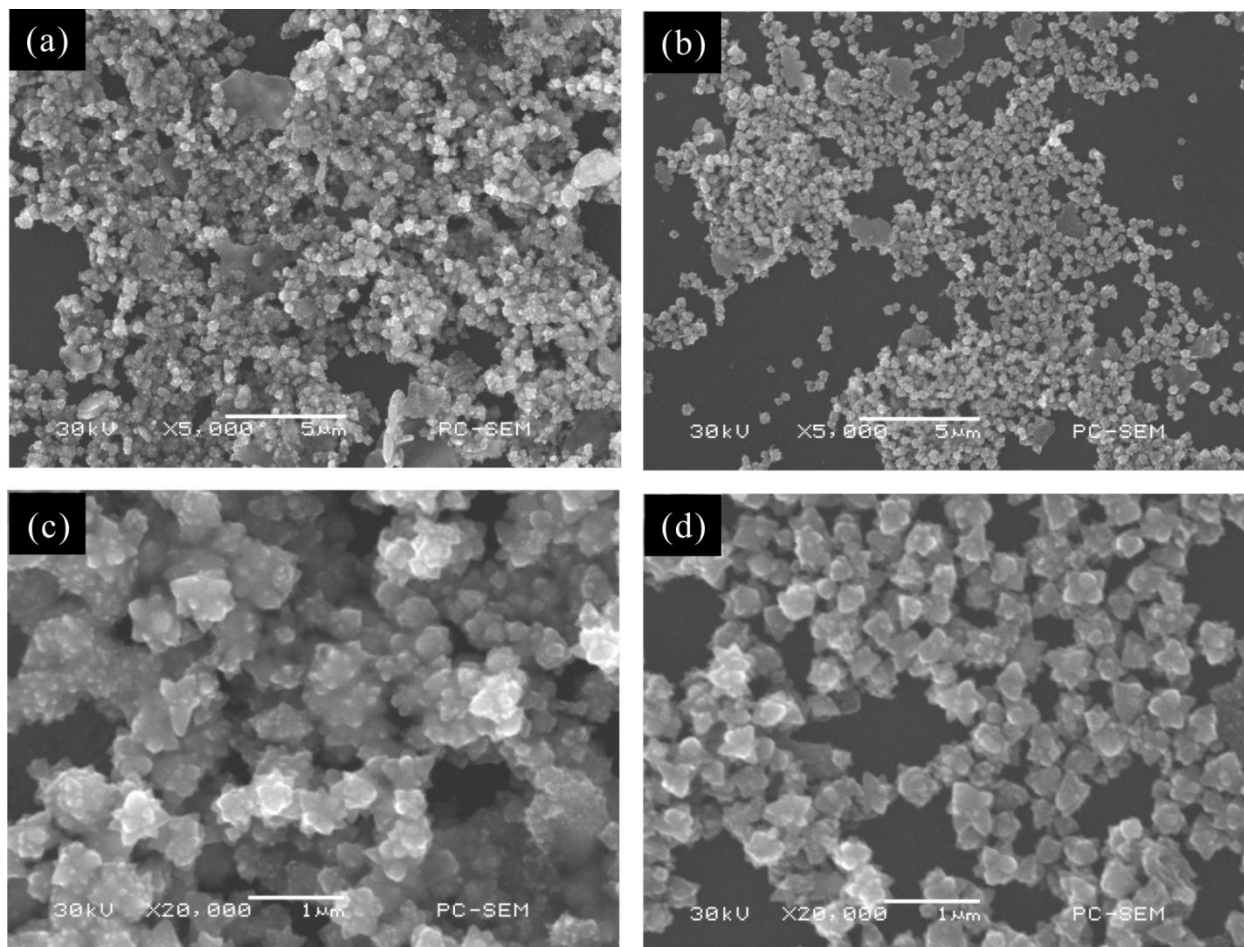


**Fig. 3.4** Submicron ZnO particles obtained by micro flow-through synthesis in DMSO solution at 80 °C by reaction of  $\text{Zn}(\text{Ac})_2$  with TMAH and EDA in the presence of PEG: (a, c): total flow rate: 100  $\mu\text{L}/\text{min}$ ; (b, d): total flow rate: 1000  $\mu\text{L}/\text{min}$ .

A significant influence of flow rate on the particle shape is illustrated in Fig. 3.4. The submicron particles were larger and more strongly attached to each other at lower total flow rate (100  $\mu\text{L}/\text{min}$ ) as shown in Fig. 3.4a, c. Some plate-like particles were also observed under this condition. However, when the total flow rate was enhanced to 1000  $\mu\text{L}/\text{min}$ , the submicron particles were much more homogeneous in size and shape. Obviously, the particles reflected the initial situation of formation of flowers. The average diameter of the overwhelming part of the submicron particles was around 477 nm (Fig. 3.4b, d).

In summary, the experiments demonstrate that different types of ZnO micro and nanoparticles can be synthesized in aqueous and DMSO solution by micro segmented flow method. The characters of the product are influenced by the reaction procedure, temperature and reactant

concentration. In addition, the flow rate has played an important role in the size, shape and homogeneity of the obtained ZnO particles. The enhancement of flow rate can lead to more uniform particles.

### 3.2 Hydrothermal micro segmented flow synthesis of ZnO microparticles with different morphologies

Production of high quality ZnO particles with different shape and size gets increasing importance since their specific physical and chemical properties are strongly dependent on particles geometry. Therefore, it is necessary to search for new methods of producing ZnO crystals with well-defined geometry and high homogeneity. In this section, the micro segmented flow technique is applied to prepare ZnO particles under condition of hydrothermal method. The influence of the reaction parameters, such as reactant concentration, molar ratio of reactants, and solvent has been varied to produce ZnO particles with different shapes and sizes.

Table 3.2 presents the details of the experimental conditions. All the experiments were carried out in set-up III (section 2.1) without any fluidic problems. The segmented flow supports a regular transport of fluids and suppresses strong aggregation of the formed particles and blocking of tubes. In set-up III, the static micro mixer is the most sensitive element of the microfluidic arrangement. However, no critical particle formation was observed in this device since the reactant solution passed the mixer rapidly (0.3 s) and the rate of particle formation was very low in this reaction phase. After segment formation and heating in the thermostat, a strong nucleation, particle growth and a resulting high particle density occur. The embedding of the formed particles suspension inside the fluid segments allows a safe handling of the formed product. Furthermore, because of the low wettability of the wall surface of microtubes by the aqueous reactant solution and the continuous movement of particles, particle sedimentation and blocking can be avoided.

Fig. 3.5 shows XRD patterns of three ZnO products prepared by micro segmented flow synthesis. All the diffraction peaks can be exactly indexed to the hexagonal wurtzite ZnO, which is in good agreement with the values in the standard card (JCPDS card 36-1451). No characteristic diffraction peaks from other phases or impurities were found.

**Table 3.2** Experimental conditions for hydrothermal synthesis of ZnO particles.

i	Zn(Ac) <sub>2</sub>	NaOH	TD <sup>a</sup>	pH <sup>b</sup>	Solvent	T	Product	
Flow rate	1000 $\mu\text{L}/\text{min}$	1000 $\mu\text{L}/\text{min}$	3000 $\mu\text{L}/\text{min}$					
Conc.	0.10 M	1.00 M		13.23	H <sub>2</sub> O	150 °C	Fig. 3.11c	
		1.25 M		13.21	H <sub>2</sub> O	150 °C	Fig. 3.6a	
		1.50 M		13.17	H <sub>2</sub> O	150 °C	Fig. 3.6b Fig. 3.11e	
		1.75 M		13.12	H <sub>2</sub> O	150 °C	Fig. 3.6c	
	0.05 M	0.50 M		13.41	H <sub>2</sub> O	150 °C	Fig. 3.8d	
		0.75 M		13.36	H <sub>2</sub> O	150 °C	Fig. 3.8e	
		1.00 M		13.31	H <sub>2</sub> O	150 °C	Fig. 3.8f	
		0.50 M	<sup>c</sup>	12.65	H <sub>2</sub> O/ isopropanol = 1/1 (v/v)	120 °C	Fig. 3.11f	
	0.02 M	0.20 M		13.30	H <sub>2</sub> O	150 °C	Fig. 3.8a	
		0.30 M		13.26	H <sub>2</sub> O	150 °C	Fig. 3.8b	
		0.40 M		13.22	H <sub>2</sub> O	150 °C	Fig. 3.8c	
	Flow rate	250 $\mu\text{L}/\text{min}$	250 $\mu\text{L}/\text{min}$	500 $\mu\text{L}/\text{min}$				
	Conc.	0.15 M	1.50 M		13.34	H <sub>2</sub> O	90 °C	Fig. 3.6d

ii	Zn(Ac) <sub>2</sub>	TEA	TD <sup>a</sup>	pH <sup>b</sup>	Solvent	T	Product
Flow rate	1000 μL/min	1000 μL/min	3000 μL/min				
Conc.	0.05 M <sup>d</sup>	0.50 M		9.00	H <sub>2</sub> O	150 °C	Fig. 3.11a
	0.02 M	0.50 M		9.56	H <sub>2</sub> O	120 °C	Fig. 3.11b
Flow rate	250 μL/min	250 μL/min	500 μL/min				
Conc.	0.05 M	0.40 M		9.47	H <sub>2</sub> O/ DMSO = 1/9 (v/v)	150 °C	Fig. 3.11d

<sup>a</sup> TD: tetradecane  
<sup>b</sup> pH value measured after hydrothermal synthesis  
<sup>c</sup> perfluoromethyldecalin (PP9) used as carrier fluid  
<sup>d</sup> 1 wt% polyacrylamide was dissolved in Zn(Ac)<sub>2</sub> solution

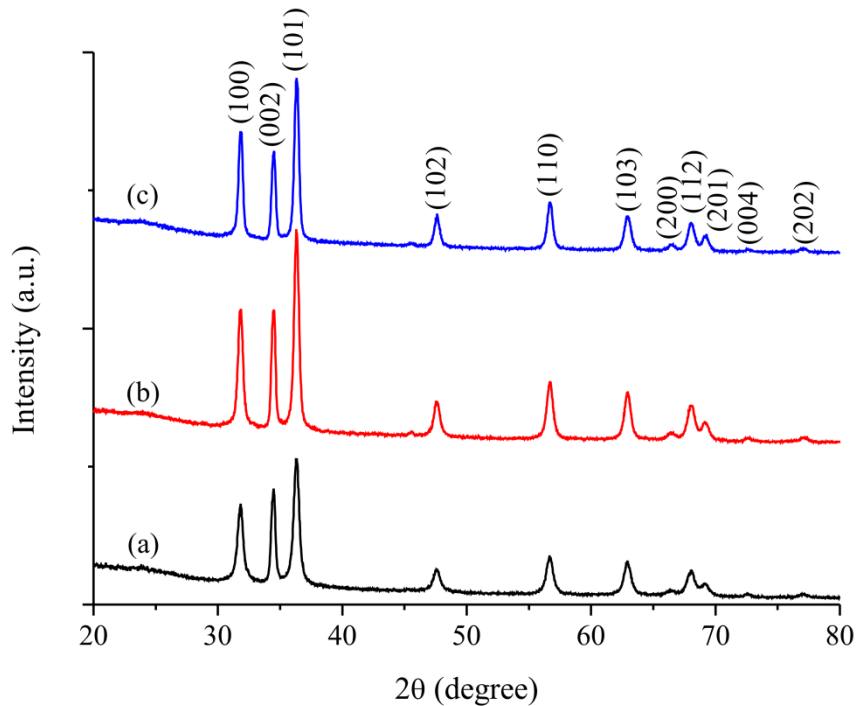


**Fig. 3.5** XRD patterns of the prepared ZnO particles at 150 °C with total flow rate of 5000 μL/min: (a) 0.05 M Zn(Ac)<sub>2</sub>, 0.5 M NaOH; (b) 0.05 M Zn(Ac)<sub>2</sub>, 0.75 M NaOH; (c) 0.05 M Zn(Ac)<sub>2</sub>, 1.0 M NaOH.

The reaction conditions strongly influence the shape and size of the obtained particles. Star-like particles with three, four, five, six or seven branches or flower-like particles with different numbers and shapes of leaves were obtained at zinc acetate concentrations of 0.1 M and above. Triangular shaped flowers were formed at moderate reactant concentrations (0.1 M  $\text{Zn}(\text{Ac})_2$ , 1.25 M NaOH), high temperature (150 °C) and high flow rate (5000  $\mu\text{L}/\text{min}$ ) shown in Fig. 3.6a. A slight enhancement of NaOH concentration (1.5 M) resulted in flower-like crystals with larger leaves (Fig. 3.6b). In addition, a transition from flower-like to star-like particles was observed if the concentration of NaOH was further enhanced to 1.75 M (Fig. 3.6c). More compact flower-like crystals with a high number of leaves oriented in all directions were obtained at reduced temperature (90 °C), moderate flow rate (1000  $\mu\text{L}/\text{min}$ ) and slightly enhanced  $\text{Zn}(\text{Ac})_2$  concentration (Fig. 3.6d).

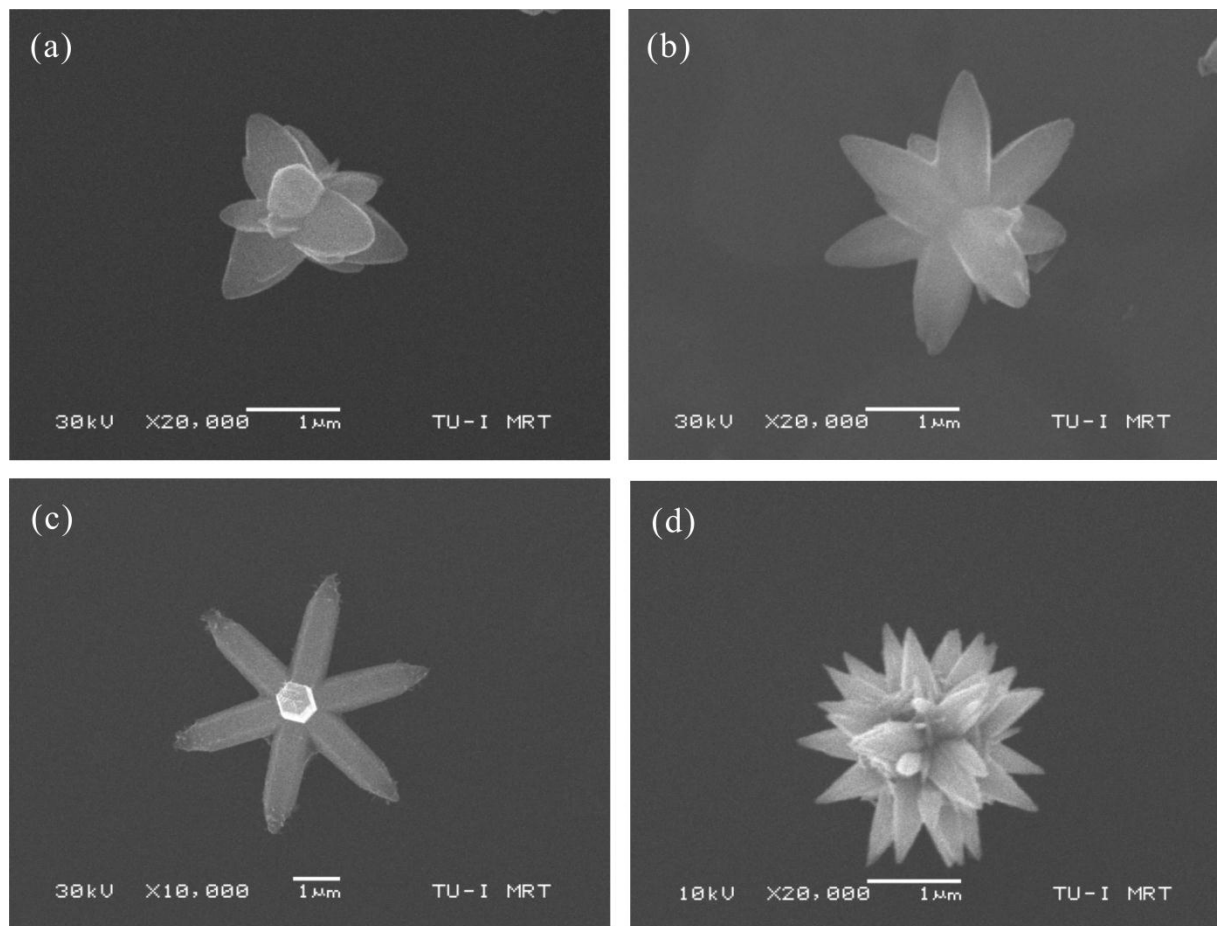


**Fig. 3.6** Star- and flower-like ZnO microparticles under different experimental conditions: (a) 5000  $\mu\text{L}/\text{min}$ , 150 °C, 0.1 M  $\text{Zn}(\text{Ac})_2$ , 1.25 M NaOH; (b) 5000  $\mu\text{L}/\text{min}$ , 150 °C, 0.1 M  $\text{Zn}(\text{Ac})_2$ , 1.5 M NaOH; (c) 5000  $\mu\text{L}/\text{min}$ , 150 °C, 0.1 M  $\text{Zn}(\text{Ac})_2$ , 1.75 M NaOH; (d) 1000  $\mu\text{L}/\text{min}$ , 90 °C, 0.15 M  $\text{Zn}(\text{Ac})_2$ , 1.5 M NaOH.

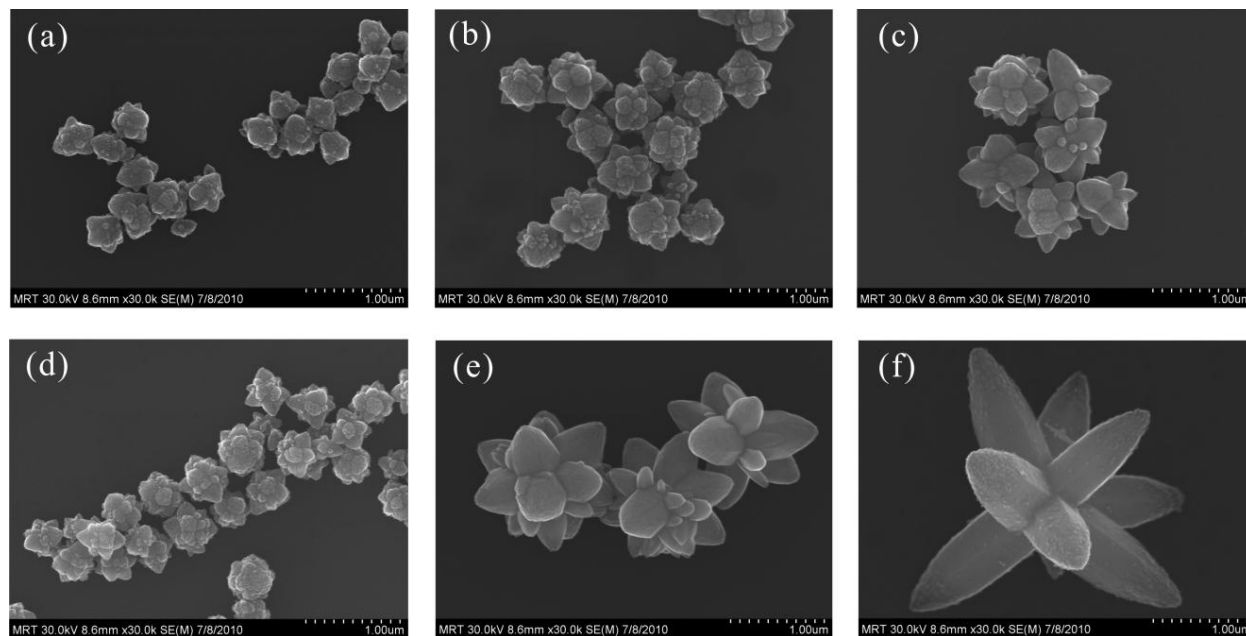


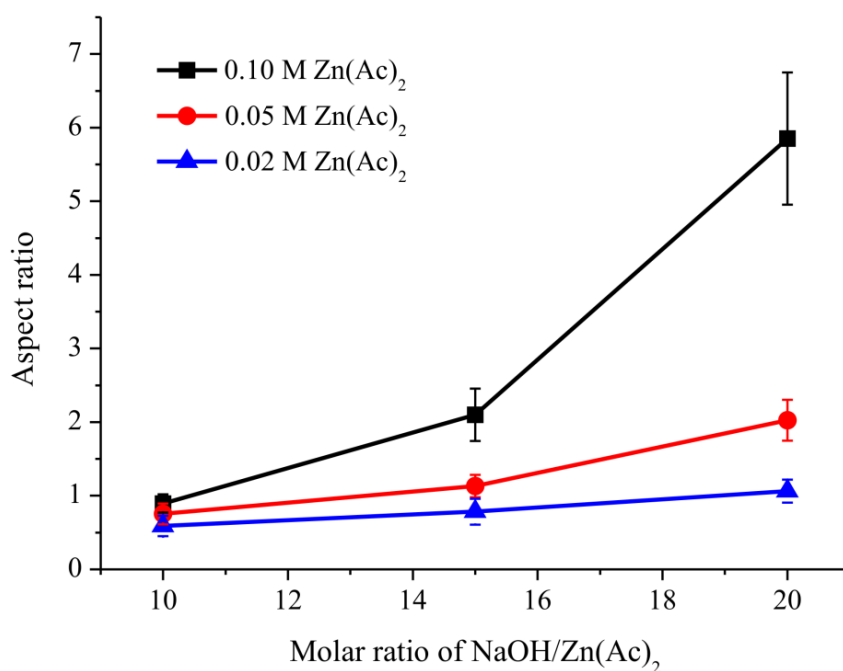
**Fig. 3.7** Increase of particle size due to an enhancement of reactant ratio of NaOH/Zn(Ac)<sub>2</sub> demonstrated by SEM images: (a) 0.02 M Zn(Ac)<sub>2</sub>, 0.2 M NaOH; (b) 0.02 M Zn(Ac)<sub>2</sub>, 0.3 M NaOH; (c) 0.02 M Zn(Ac)<sub>2</sub>, 0.4 M NaOH; (d) 0.05 M Zn(Ac)<sub>2</sub>, 0.5 M NaOH; (e) 0.05 M Zn(Ac)<sub>2</sub>, 0.75 M NaOH; (f) 0.05 M Zn(Ac)<sub>2</sub>, 1.0 M NaOH.

As known from the literature [23, 169-170], the particle size and shape strongly depend on the applied reactant concentrations. In the micro segmented flow synthesis presented here, the diameter of the ZnO particles can be easily tuned by variation of the molar ratio of NaOH/Zn(Ac)<sub>2</sub>. As shown in Fig. 3.7, an obvious increase in particle size was achieved if the reactant molar ratio of NaOH/Zn(Ac)<sub>2</sub> was enhanced from 10 to 20. When Zn(Ac)<sub>2</sub> concentration was 0.02 M, flower-shaped ZnO particles with sizes from 0.428 μm to 0.846 μm were obtained. In comparison, when the Zn(Ac)<sub>2</sub> concentration was enhanced to 0.05 M, the mean diameter of the synthesized ZnO particles dramatically increased dramatically from 0.458 μm to 3.523 μm as the concentration of NaOH was varied from 0.5 M to 1.0 M. In addition, it was interesting to note that the morphology of the prepared particles changed from multi-petal flower shape with short branches to star shape with fewer, long branches.

Table 3.3 summarizes the size and size distribution of the obtained ZnO particles with Zn(Ac)<sub>2</sub> concentration of 0.02 M and 0.05 M. The results demonstrate that the achieved particle size increased with enhancing the molar ratio of NaOH/Zn(Ac)<sub>2</sub>. The polydispersity index (PDI) of the products was between 1.03 and 1.07. Obviously, the available concentration of Zn(II) ions determines the particular effect of hydroxide ions on the fast axial crystal growth.

**Table 3.3** Effect of the reactant concentration on the size and size distribution of ZnO particles.

Zn(Ac) <sub>2</sub>	NaOH	Mean diameter (μm)	Standard Derivation (μm)	CV (%)	PDI
0.02 M	0.20 M	0.428	0.053	12.5	1.04
	0.30 M	0.642	0.083	12.9	1.05
	0.40 M	0.846	0.110	13.0	1.05
0.05 M	0.50 M	0.458	0.054	11.7	1.04
	0.75 M	1.541	0.230	14.9	1.07
	1.00 M	3.523	0.339	9.6	1.03

**Fig. 3.8** Effect of the reactant ratios on the aspect ratio of the flower- and star-like ZnO particles for three different Zn(Ac)<sub>2</sub> concentrations.

This enforced crystal growth and the dependence on the concentration of Zn(Ac)<sub>2</sub> correlate well with the increase in the aspect ratio of the branches or flower leaves of the formed crystals shown in Fig. 3.8. The aspect ratio can be weakly tuned between about 0.6 and 1.1 by an increase of the reactant ratio from 10 to 20 if a Zn(Ac)<sub>2</sub> concentration of 0.02 M was applied.

However, an increase of the  $\text{Zn}(\text{Ac})_2$  concentration by a factor of 2.5 can tune the aspect ratio from 0.8 to 2.0 if the molar ratio of reactants was varied between 10 and 20. A further increase of  $\text{Zn}(\text{Ac})_2$  concentration to 0.1 M resulted in an extended tuning range for the aspect ratio from 0.9 to 5.9. The increase in aspect ratio was due to the stronger dependence of the axial growth on the molar ratio of the reactants compared to the lateral growth of the single ZnO branches. This fact is well reflected by the dependence of the flower branch length on the reactant ratio of  $\text{NaOH}/\text{Zn}(\text{Ac})_2$  shown in Fig. 3.9. This dependence increased strongly with enhancing  $\text{Zn}(\text{Ac})_2$  concentration. In particular, when the  $\text{Zn}(\text{Ac})_2$  concentration was 0.05 M, an increase of branch lengths from about 148 to 1380 nm was observed.

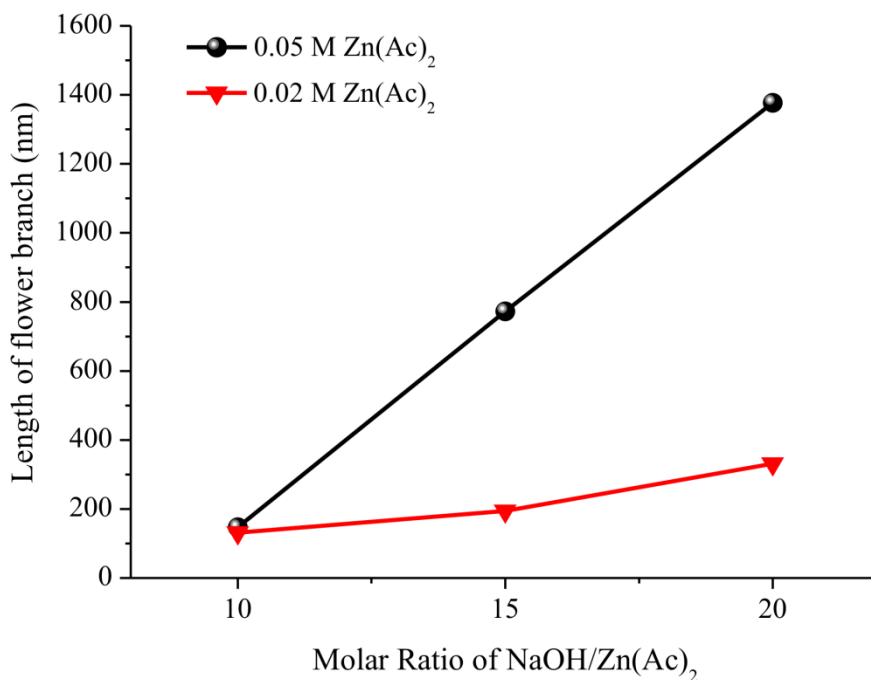
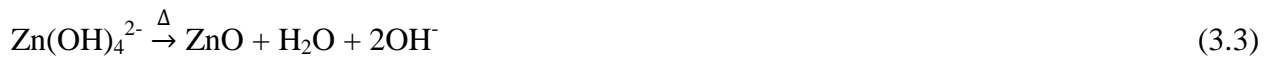


**Fig. 3.9** Dependence of the branch length of ZnO particles on the molar ratios of  $\text{NaOH}/\text{Zn}(\text{Ac})_2$ .

It is well known that ZnO is a polar crystal, whose positive polar face (0001) is rich in Zn and negative polar face (000 $\bar{1}$ ) is rich in O. The Zn-(0001) face is catalytically active for the growth of nanostructures, while the O-(000 $\bar{1}$ ) is inert [171-172]. Therefore, the growth rate along the (0001) direction is the fastest compared to other growth facets [173]. From Table 3.2, it is observed that pH values varied from 13.1 to 13.4 with NaOH as base and water as solvent. Under

these basic conditions,  $\text{Zn(OH)}_4^{2-}$  is the dominant species in the solution. As we know, under hydrothermal conditions, the growth unit of ZnO crystal is  $\text{Zn(OH)}_4^{2-}$ . With the increase in temperature, ZnO nuclei are formed from the dehydration of  $\text{Zn(OH)}_4^{2-}$  ions [174]. The growth units  $\text{Zn(OH)}_4^{2-}$  are then directly incorporated into the formed nuclei, which grow further into the ZnO crystals. The generally accepted chemical mechanism for ZnO formation is shown below:



According to the experimental results above, the formation mechanism of ZnO flower-like particles under hydrothermal conditions is proposed and illustrated in Fig. 3.10. The molar ratio of  $\text{NaOH}/\text{Zn(Ac)}_2$  plays an important role for the formation of ZnO particles. At lower molar ratio of  $\text{NaOH}/\text{Zn(Ac)}_2$ , the nucleation rate is relatively high according to equation (3.3) and a large amount of ZnO nuclei is produced. These ZnO nuclei may aggregate together due to excess saturation [23] or under the driving forces of surface energy [18]. Each nucleus then individually grows anisotropically along its c-axis. Due to the lower concentration of the building unit  $\text{Zn(OH)}_4^{2-}$ , the crystal growth rate is relatively slow. Hence, the obtained flower-like particles have smaller diameter with short branches. In comparison, at higher molar ratio of  $\text{NaOH}/\text{Zn(Ac)}_2$ , the nucleation rate is slow, but the crystal growth is very fast. It can provide sufficient supply of  $\text{Zn(OH)}_4^{2-}$ , which is required for the formation of the desired ZnO structures. Owing to the small amount of nuclei and sufficient growth units, large flower-like ZnO particles with longer branches are formed.

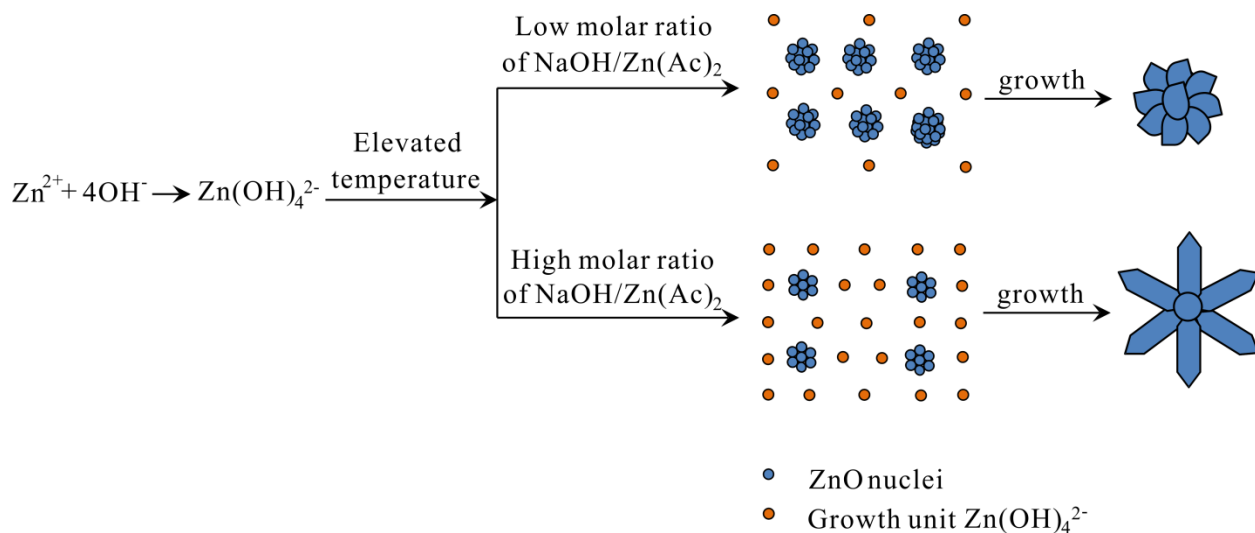


**Fig. 3.10** A schematic diagram of the formation of ZnO flower-like particles under hydrothermal conditions.

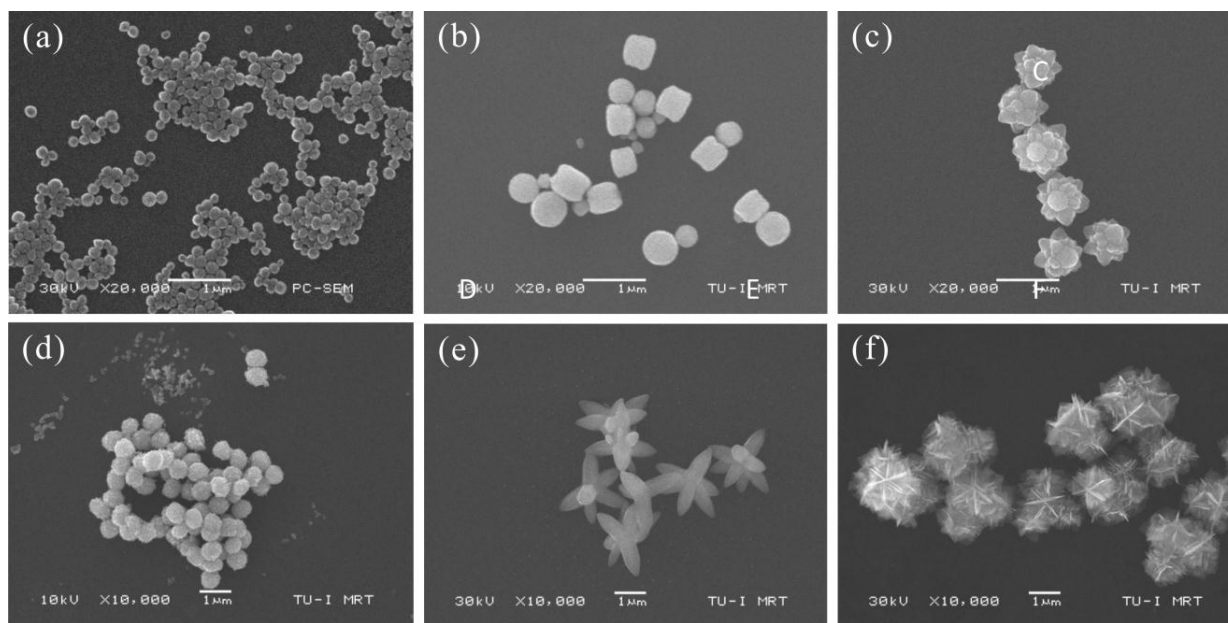


**Fig. 3.11** ZnO microparticles obtained by hydrothermal micro segmented flow synthesis under different conditions. The detailed experimental conditions are described in Table 3.2.

The spectrum of particle shapes can be further enlarged if the surfactants, polymer additives [175] or different water/solvent mixtures are applied. Perfluorinated alkanes (PP9) have to be used as carrier liquids for the segmented flow in case of the application of solvents in order to avoid mixing of solvents and carrier solution. Small spheres (about 150 nm in diameter) were formed in the presence of 1 % polyacrylamide (Fig. 3.11a). The addition of triethanolamine

caused the formation of cylinder-like particles at 120 °C (Fig. 3.11b). Spherical particles were found in a solvent mixture of DMSO and water (9:1) in the presence of triethanolamine (Fig. 3.11d). Larger spherical aggregates were obtained in a 1:1 water/isopropanol mixture at 120 °C (Fig. 3.11f). These crystal shapes were quite different from the flower-like and star-like particles obtained in pure water solutions (Fig. 3.11c, e). The change of the crystal shape can be ascribed to the polarities and saturated vapor pressures of the solvents, which influence the solubility of the precursor in the particular solvent, initial nucleation, agglomeration and preferred orientation of the crystals [176-177]. In analogy to the micro continuous flow procedures in solvent-modified water solutions, all solvent-affected synthesis procedures led to the products with a high homogeneity of particle formation. The product quality was only reduced when non-regular segmentation took place. In all other cases, a narrow distribution of particle sizes and shapes was obtained.

In summary, the experiments demonstrate that the micro segmented flow is suitable for micro continuous-flow hydrothermal synthesis of a wide spectrum of ZnO microparticles. The fluid segments were formed regularly up to flow rates of 5000  $\mu\text{L}/\text{min}$ . The homogeneous formation of the fluid segments ensured constant process conditions and very narrow residence time behavior in the flow synthesis. As a result, the products with high homogeneity in shape and size were obtained. The synthesis technique can be applied for the formation of star-like, flower-like or spherical particles. The aspect ratio of crystals in stars and flowers can be tuned between 0.6 and 5.9. The particle type can be adjusted by choosing the suitable absolute concentration of reactants and by the ratio of  $\text{NaOH}/\text{Zn}(\text{Ac})_2$ .

### **3.3 Effect of the water content on growth and optical properties of ZnO particles generated by micro segmented flow synthesis**

In ZnO particles synthesis, there are a lot of experimental parameters which can influence the particle size and shape. This section mainly focuses on the effect of the water content in binary solvent mixtures on the obtained particles under two different experimental conditions by micro segmented flow synthesis.

Preliminary investigations of the effect of solvents on the formation of ZnO micro and nanoparticles by hydrothermal synthesis have shown qualitatively the impact of water on the quality of the formed particles. In particular, the transition between more compact and star-like or flower-like particles is strongly affected by the presence of water. Therefore, here the effect of water on ZnO particles has been studied in ethylene glycol by use of polyol-mediated synthesis [97, 160, 178-179].

Despite the higher probability of wall interactions, micro reaction technology is an interesting alternative to batch synthesis for the generation of nanoparticles. The polyol-mediated synthesis can profit from fast heat and mass transfer which can be realized under micro flow conditions. It is expected that the homogeneity of ZnO particles can be improved if a micro continuous flow process is applied. In contrast to homogenous fluids, the application of micro segmented flow is particularly promising for ZnO nanoparticles synthesis because the surface of the tube wall is hydrophobic and shows good wetting conditions for the inert carrier liquid and a high contact angle with the reaction mixture. In this case, the interaction between reactants and the wall can be drastically reduced. Furthermore, the initiation of nucleation or the deposition of particles at the wall surface can be suppressed [180]. In addition, the segment-interval convection caused by the motion of fluid segments can be used to accelerate the heat transfer and to enhance fast mixing [94, 116, 181]. This process is intensified by increasing the flow rate, which would lead to the reduction of reaction time.

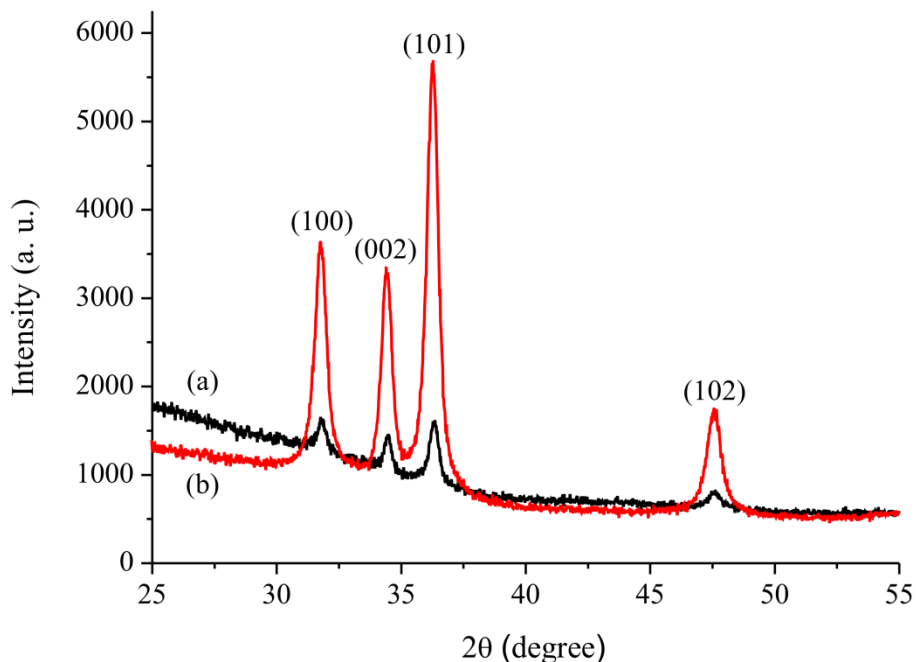
**Table 3.4** Experimental conditions for synthesis of ZnO particles in binary solvent mixture of water/EG.

Experimental Condition		Zn(Ac) <sub>2</sub> in EG	NaOH in EG	Solvent	TD <sup>a</sup>	T	H <sub>2</sub> O content	Products
i	Conc. (M)	0.02	0.2	H <sub>2</sub> O	3000	100 °C		
	Flow rate (μL/min)	850	850	300			15 v%	Fig. 3.13a-c
		750	750	500			25 v%	Fig. 3.13d- f
		650	650	700			35 v%	Fig. 3.13g-i
		500	500	1000			50 v%	Fig. 3.13j-l
		250	250	1500			75 v%	Fig. 3.13m-o
		100	100	1800			90 v%	Fig. 3.13p-r
ii	Conc. (M)	0.05	1	EG/H <sub>2</sub> O	500	90 °C		
	Flow rate (μL/min)	30	30	90			15 v%	Fig. 3.16a, b
							25 v%	Fig. 3.16c, d
							30 v%	Fig. 3.16e, f
							45 v%	Fig. 3.16g, h
							60 v%	Fig. 3.16i, j
<sup>a</sup> TD: tetradecane								

Table 3.4 presents the used experimental parameters in detail. For experimental condition (i), the formation of ZnO particles was carried out at higher total flow rate (5000 μL/min) and enhanced temperature (100 °C) with lower concentration ratio of NaOH/Zn(Ac)<sub>2</sub> (10/1). Different water contents from 5 v% to 90 v% were achieved by adjusting the flow rates of the reactant solutions. In comparison, for experimental condition (ii), the experiments took place at lower total flow rate (650 μL/min) and reduced temperature (90 °C) with higher concentration ratio of NaOH/Zn(Ac)<sub>2</sub> (20/1). The segment size for condition (i) and (ii) was about 0.77 μL or 1.1 μL, respectively. By changing the solvent ratio of water/EG, different water contents were achieved while the total flow rate was kept constant during the synthesis procedure.

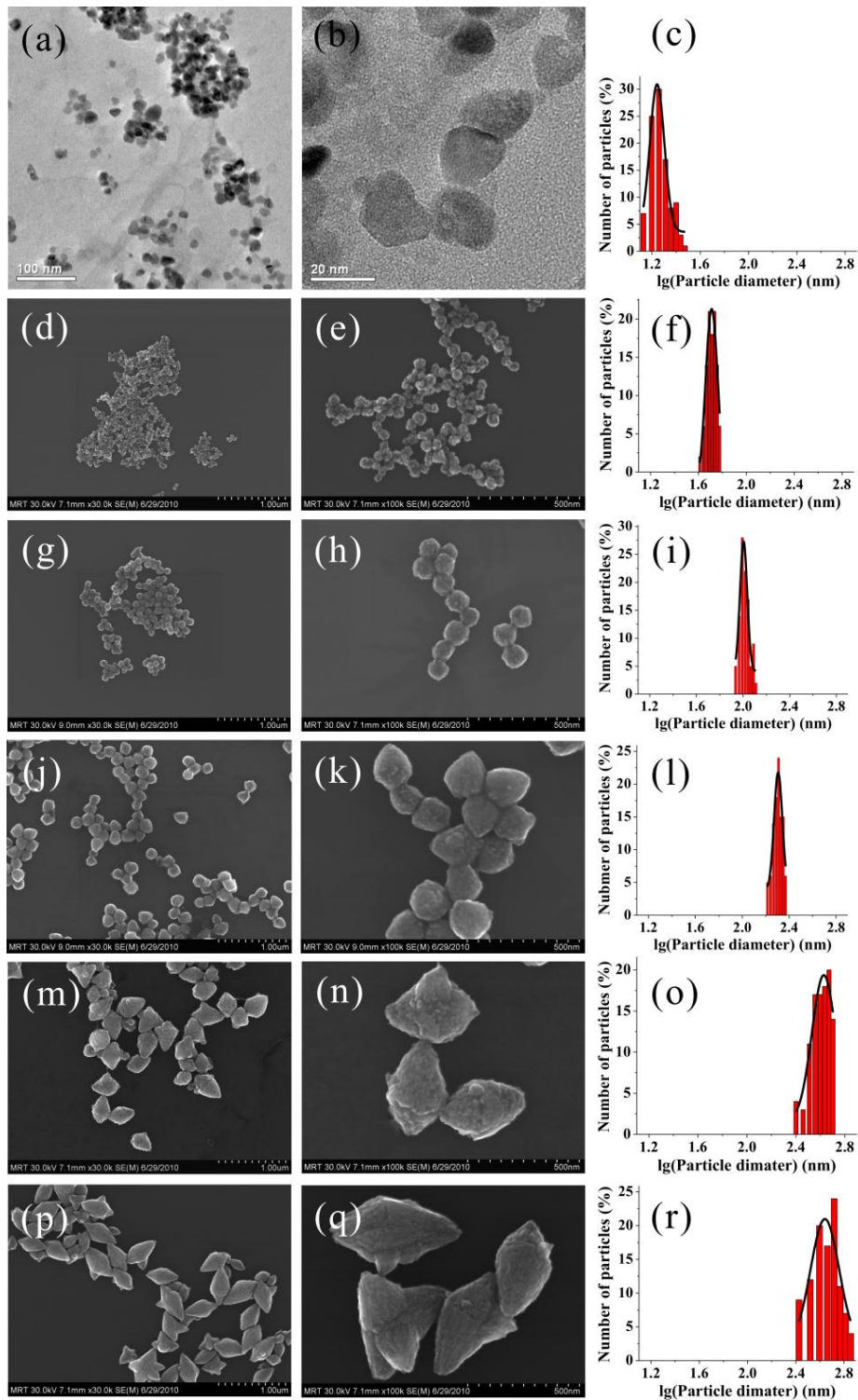
All experiments were carried out using set-up IV, which had been described in detail in section

2.1. A 2+1 static micro mixer was used to mix the reactants. Its volume was around 10  $\mu\text{L}$  and the mixing time was calculated to be 0.3 s and 4 s for condition (i) and (ii), respectively.



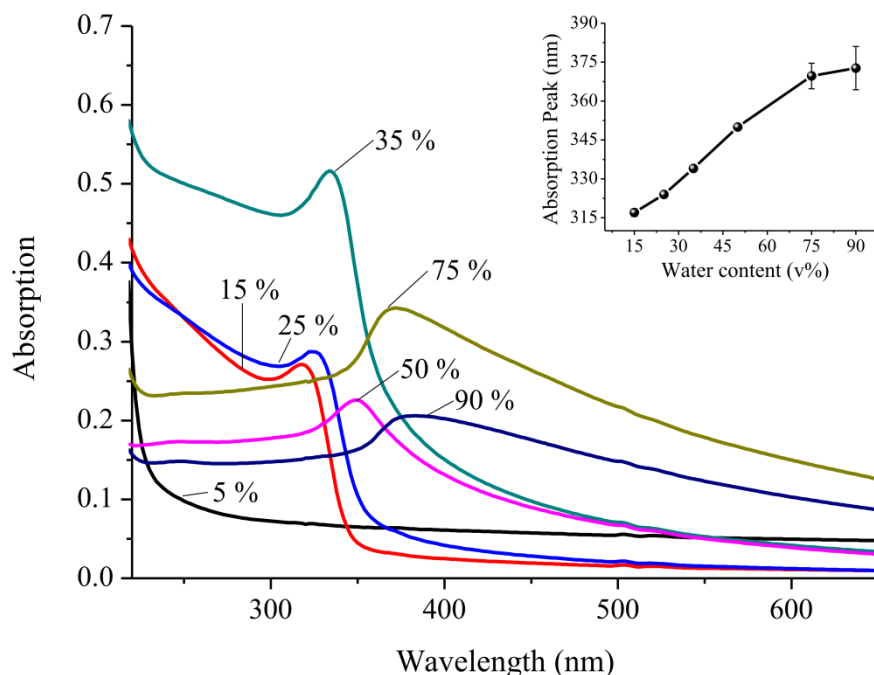
**Fig. 3.12** XRD patterns of the synthesized ZnO particles: (a) water content: 50 v% under condition (i); (B) water content: 30 v% under condition (ii).

Fig. 3.12 shows the XRD patterns of two typical as-prepared ZnO products. All the diffraction peaks in Fig. 3.12 can be exactly indexed to the hexagonal wurtzite ZnO with lattice parameters of  $a = 3.25 \text{ \AA}$  and  $c = 5.21 \text{ \AA}$  ( $c/a = 1.60$ ), which was in good agreement with the values in the standard card (JCPDS card 36-1451). In addition, no characteristic diffraction peaks from other phases or impurities were found.



**Fig. 3.13** Effect of the water content on the shape, size and size distribution of the ZnO particles synthesized under experimental condition (i) (0.02 M  $\text{Zn}(\text{Ac})_2$ , 0.2 M NaOH, 100 °C, 5000  $\mu\text{L}/\text{min}$ ) demonstrated by TEM and SEM images: (a, b, c) 15 v%; (d, e, f) 25 v%; (g, h, i) 35 v%; (j, k, l) 50 v%; (m, n, o) 75 v%; (p, q, r) 90 v%.

From the TEM and SEM images from experimental condition (i) shown in Fig. 3.13, it can be seen that the shape and size of the obtained particles strongly depend on the water content in the system. When the water content was below 35 v%, homogeneous quasi-spherical ZnO nanoparticles were synthesized (Fig. 3.13a-h). Their average particle size increased from 18 nm to 102 nm when the water content was enhanced from 15 v% to 35 v%. The size distribution graphs of these particles are shown in Fig. 3.13c, f, i. Furthermore, the particle shapes shifted from nut-like (Fig. 3.13j, k) to ellipsoidal (Fig. 3.13m, n, p, q) when the water content was increased from 50 v% to 90 v%. Meanwhile, the average particles diameter increased significantly from 196 nm to 436 nm, and the particle size distribution became broad (Fig. 3.13o, r).



**Fig. 3.14** UV/Vis spectra of ZnO particles obtained with different water contents under experimental condition (i) (0.02 M Zn(Ac)<sub>2</sub>, 0.2 M NaOH, 100 °C, 5000 μL/min). The insert graph shows the absorption peaks of ZnO particles in the presence of different water contents.

Besides the particle size, the effect of water content also influences the UV/Vis spectra of the products. From Fig. 3.14, it can be observed that the absorption peak of the obtained ZnO particles shifted from 317 nm to 373 nm when the water content was increased from 15 v% to 90

v%. In particular, when the water content was 5 v%, there was no absorption peak since no precipitation occurred. From the inset graph in Fig. 3.14, the increase of the wavelength of the absorption peaks with enhancing water contents can be observed, which was associated with particle growth [182]. It has already been reported that the dependence of particle size on the optical absorption spectra can be determined by using the effective mass model. The details of the calculation can be found in the references [183-184].

These results are consistent with that of polyol-mediated synthesis in batch [78], where water plays an important role in determining the particle shape and size since water can induce hydrolysis and condensation reactions for the Zn precursor [185]. At lower water contents, ethylene glycol as a chelating agent, can adsorb on the surface of the nucleus and limit the particle growth and avoiding agglomeration. Therefore, the quasi-spherical particles with homogeneous size distribution were obtained when the water content was below 35 v%. If the water content was sufficiently high to hydrolyze the Zn complexes, enhanced growth rate was expected. Therefore, the resulting particles became larger and inhomogeneous due to a lower concentration of ethylene glycol, the assumed complexing agent that inhibits the particle growth and aggregation.

In order to investigate the composition of the obtained ZnO particles, TG-DTA analysis were carried out to measure two samples with the water contents of 35 v% and 50 v% under condition (i) (Fig. 3.15). In Fig. 3.15a, the weight loss between 30 °C-400 °C was observed in the TG curve. The weight loss at 30 °C-200 °C was associated with the removal of physically absorbed water, while the weight loss at 200 °C-400 °C can be attributed to the decomposition of ethylene glycol on ZnO particles. No further weight loss was observed when the temperature was higher than 400 °C. In the TG curve of Fig. 3.15b, the weight loss between 30 °C-400 °C was similar to that of Fig. 3.15a. However, further weight loss was found between 400 °C-750 °C, which could be caused by the burnout of strongly bound ethylene glycol due to the lower water content under this condition. On both of the DTA curves, two exothermic peaks were observed at about 280 °C and 340 °C, respectively. These peaks were associated with decomposition of the EG adsorbed on the particles. The total weight loss for these two measurements was 2.2 % with the water content of 50 v% and 5.5 % with the water content of 35 v%, respectively. It supported our assumption mentioned before that the particle size can be suppressed at lower water content

since higher content of ethylene glycol can adsorb on the surface of the particles.

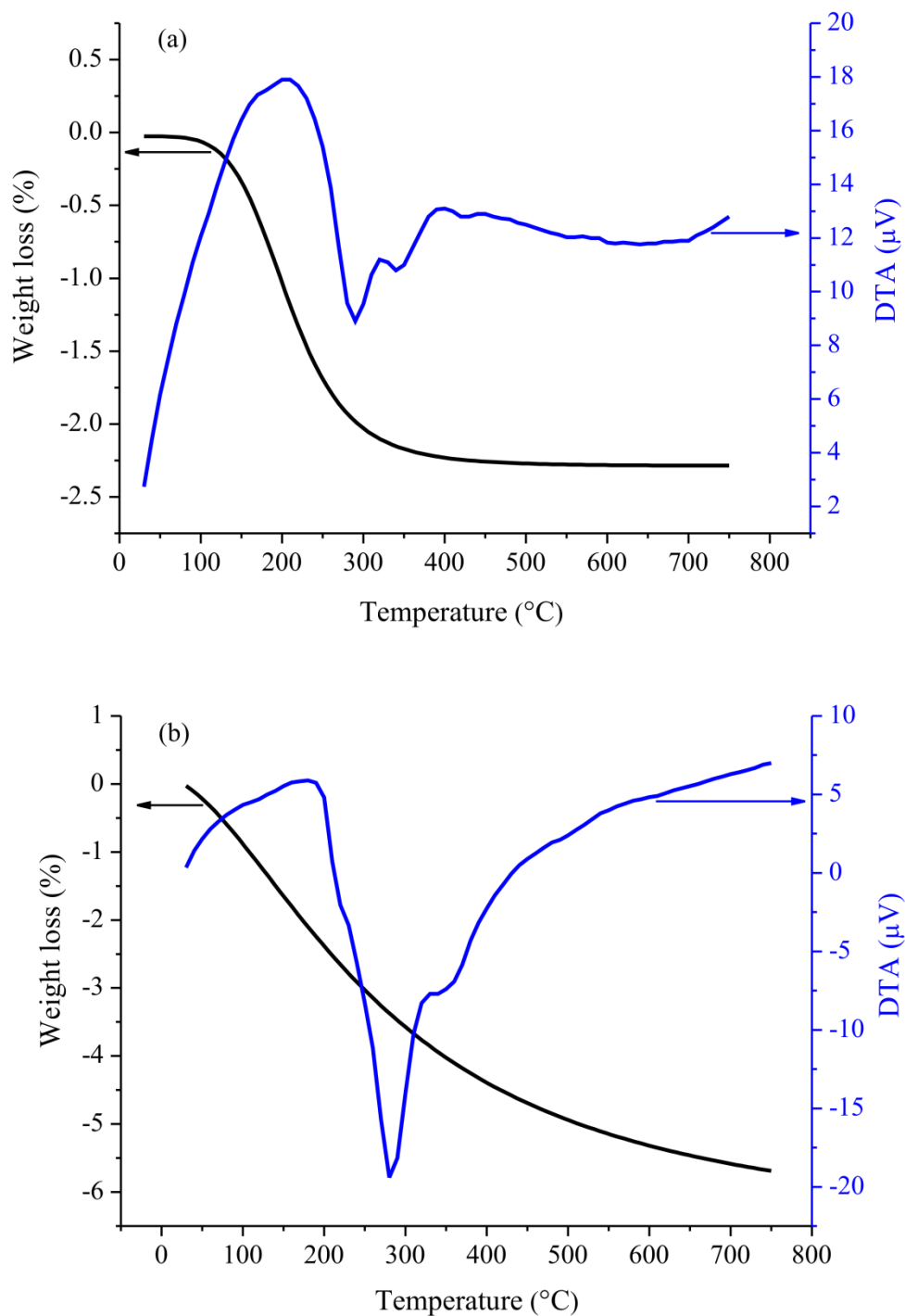


**Fig. 3.15** TG-DTA curves of the ZnO products under condition (i): (a) water content: 50 v%; (b) water content: 35 v%.

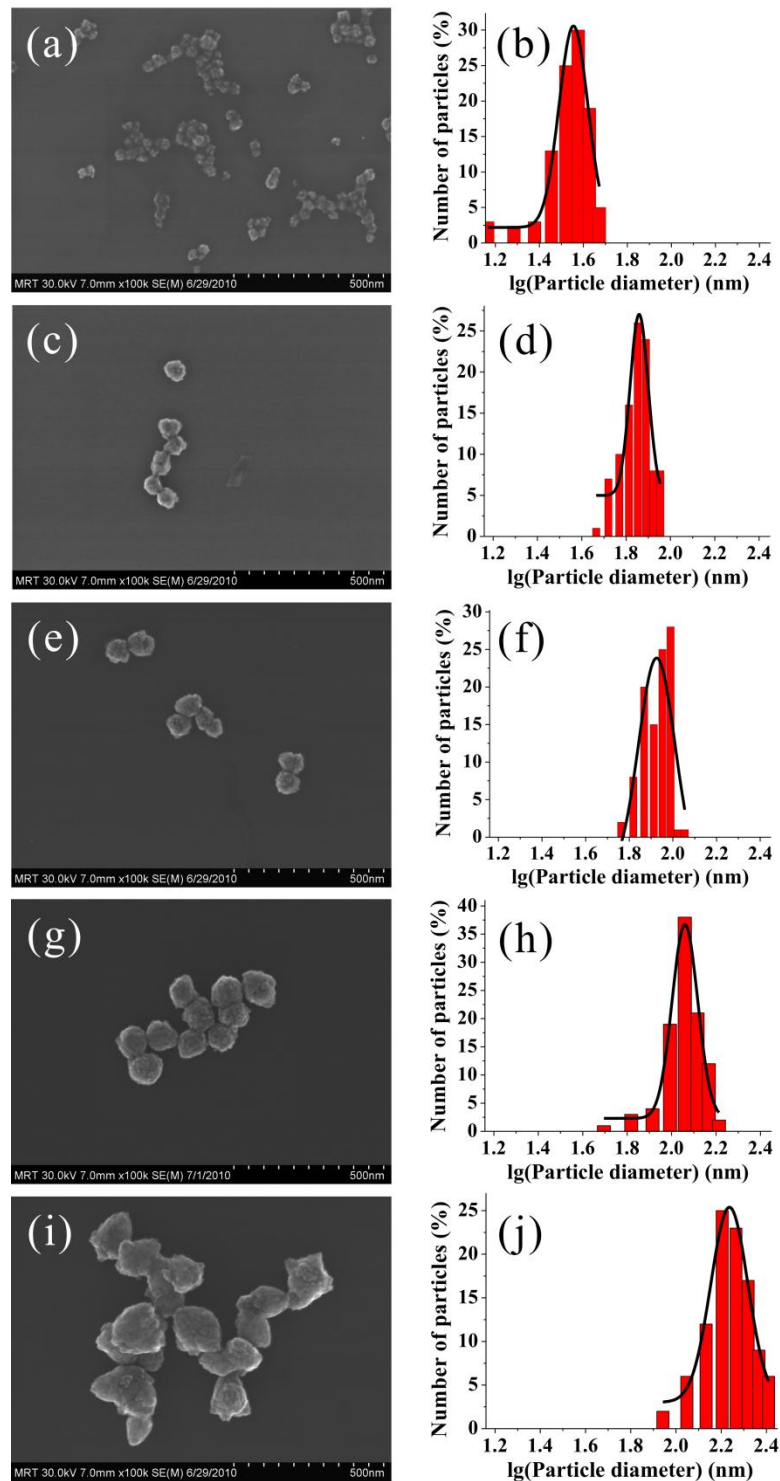


**Fig. 3.16** Effect of the water content on the shape, size and size distribution of ZnO particles synthesized under experimental condition (ii) (0.05 M  $\text{Zn}(\text{Ac})_2$ , 1 M NaOH, 90 °C, 650  $\mu\text{L}/\text{min}$ ) demonstrated by SEM images: (a, b) 15 v%; (c, d) 25 v%; (e, f) 30 v%; (g, h) 45 v%; (i, j) 60 v%.

On the other hand, under experimental condition (ii), quasi-spherical ZnO nanoparticles were obtained for the water contents between 15 v% and 45 v%. A. Dakhlaoui [186] and B.G. Wang *et al.* [187] also have observed that at higher alkaline ratio, the ZnO particles appear in spherical shape. SEM images under this condition are shown in Fig. 3.16, which demonstrate the increasing of particle size with enhancing the water content. The size distribution graphs show that the obtained particles had narrow size distribution.

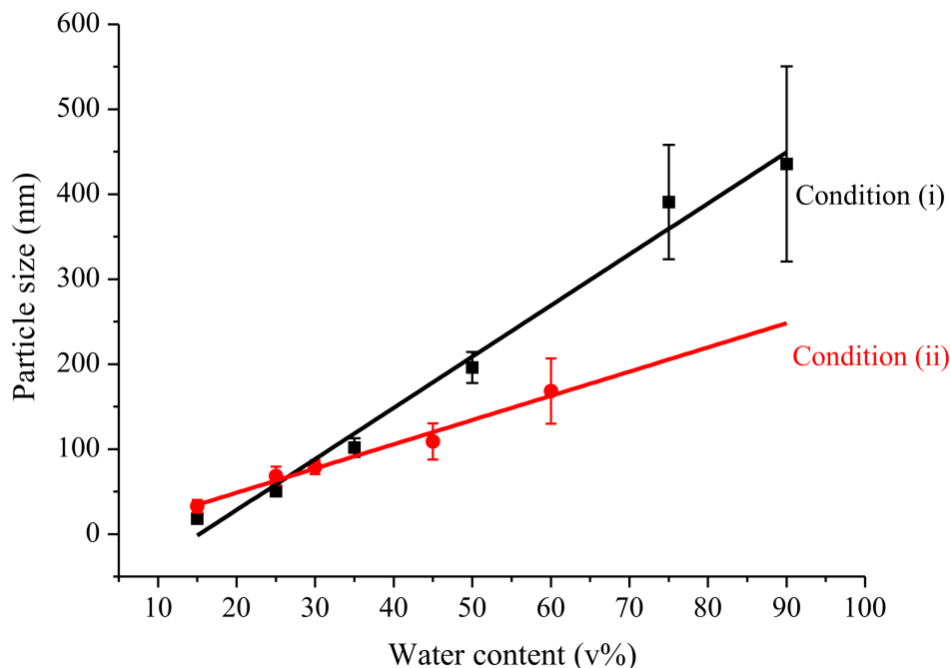


**Fig. 3.17** Comparison of the effect of the water content on the particle size under experimental conditions (i) and (ii).

Fig. 3.17 compares the effect of the water content on the particle size under both experimental conditions. It indicated that the obtained particle size was strongly dependent on the water content in binary solvent mixtures. Furthermore, the effect of the water content on particle size at experimental condition (i) was more noticeable than condition (ii).

UV/Vis absorption spectra for ZnO products under condition (ii) are shown in Fig. 3.18. All spectra were marked by the characteristic peak in the UV range (at about 340 nm). However, the peak shift with the water content was much smaller than that in the case of conditions (i). In

addition, the shift of absorption in the longer wavelength range was considerably reduced. The insert graph in Fig. 3.18 reveals the absorption peak wavelength of obtained ZnO particles as a function of the water content. It is similar to the insert graph in Fig. 3.14. Fig. 3.19 investigates the effect of the water content on absorption peak wavelength under condition (i) and (ii). It matches well with Fig. 3.17 since the absorption peak wavelength is dependent on particle size.

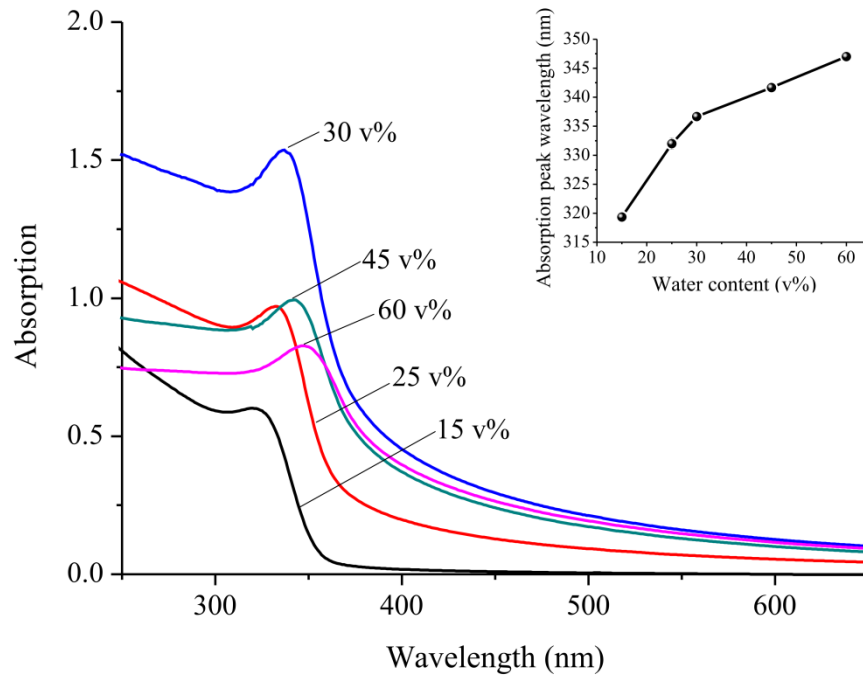


**Fig. 3.18** UV/Vis spectra of ZnO particles obtained with different water contents under experimental condition (ii). The insert graph shows the absorption peak wavelength as a function of the water contents.

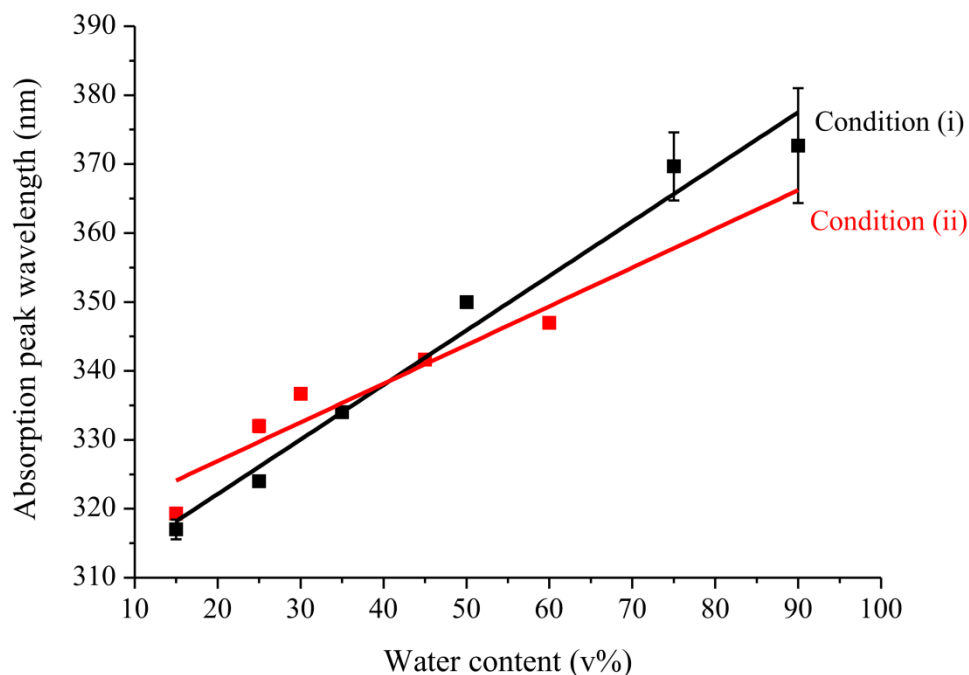


**Fig. 3.19** Comparison of the effect of the water content on the absorption peak wavelength under experimental condition (i) (0.02 M  $\text{Zn}(\text{Ac})_2$ , 0.2 M NaOH, 100 °C, 5000  $\mu\text{L}/\text{min}$ ) and (ii) (0.05 M  $\text{Zn}(\text{Ac})_2$ , 1 M NaOH, 90 °C, 650  $\mu\text{L}/\text{min}$ ).

In summary, this work has shown that the preparation of high quality ZnO nanoparticle by using  $\text{Zn}(\text{Ac})_2$  and NaOH in binary solvents of water and EG is possible to be realized in the micro segmented flow system. By changing the water contents in the reactant solutions from 5 v% to 90 v%, the diameter of the ZnO particles was tuned from 18 nm to 436 nm. In particular, at the water contents below 50 v%, ZnO nanoparticles with homogeneous size distribution were obtained. The high homogeneity of the produced particles can be attributed to the fast mixing and the efficient heat transfer inside the small droplets of reaction mixture caused by the flow-induced segment-internal convection. UV/Vis absorption spectra confirm the change of the particle quality in case of increasing the water contents. Therefore, the micro segmented flow synthesis is a useful technology to prepare ZnO nanoparticles and should be an interesting option to prepare other metal or metal oxide nanopowders.

### 3.4 Local structure studies of ZnO micro flowers and nanoparticles obtained by micro segmented flow synthesis

In nanoscience, an accurate characterization of the particle size is important for better understanding of the physical properties of materials. Small angle X-ray scattering (SAXS) has proved to be a quick and precise method to determine the size, size distribution and shape of nanoparticles in solution [160]. This technique can measure different types of samples such as powders, emulsions or liquids in the nanometer range. It also benefits from deriving quantitative information from a statistically significant population of particles at one time [161]. Biswas *et al.*[188] used SAXS to characterize ZnO nanorods. The values of the average length and diameter of ZnO nanorods obtained by SAXS are consistent with those determined by TEM.

In addition, it is necessary to study the local structure properties of materials since structural changes, including distortions and disorders as well as surface and size effects, contribute to their properties [189]. It is well known that extended X-ray absorption fine structure (EXAFS) spectroscopy can reveal the bond length, bond length disorder and atomic species located around the absorbing atom [190]. EXAFS has been used to investigate the structural order in ZnO films [191] and grain boundaries in ZnO nanostructures [192]. However, there has been no report about local structure studies of ZnO micro flowers by EXAFS so far.

In this section, the micro segmented flow technique is applied to synthesize ZnO micro flowers and nanoparticles. The size of ZnO nanoparticles is characterized by TEM and SAXS. Furthermore, EXAFS is used to investigate the local atomic structure of ZnO micro flowers and understand the blue shift of the visible emission from ZnO nanoparticles.

The detailed experimental conditions to prepare ZnO micro and nanoparticles are provided in Table 3.5. All the experiments were carried out in set-up III shown in section 2.1. When the reaction started, the static micromixer first mixed the two reactants at room temperature. The mixing time was calculated to be 0.3 s and 0.7 s for conditions (i) and (ii), respectively. After mixing, the micro fluid segments were formed by injection of the reaction mixture into a stream of carrier medium: tetradecane or perfluoromethyldecalin (PP9). Particle growth took place in the final tube coils inside the thermostat. The total residence time was calculated to be 9 s and 22 s for condition (i) and (ii), respectively. Experimental condition (i) was applied to prepare ZnO

microparticles by use of hydrothermal method. It was carried out at a total flow rate of 5000  $\mu\text{L}/\text{min}$  and a constant temperature of 150  $^{\circ}\text{C}$ . In comparison, experimental condition (ii) was based on the sol-gel method [86, 193-194], which are widely applied for synthesis of ZnO nanoparticles. It occurred at a lower total flow rate (2200  $\mu\text{L}/\text{min}$ ) at room temperature. Under both conditions, two different molar ratios of reactants were used to tune the particle size.

**Table 3.5** Experimental conditions for synthesis of ZnO flower-like microparticles and nanoparticles.

	Zn salt/solvent	Base/solvent	Carrier medium	Temperature
i	Zn(Ac) <sub>2</sub> /H <sub>2</sub> O	NaOH/H <sub>2</sub> O	TD <sup>a</sup>	
Flow rate	1000 $\mu\text{L}/\text{min}$	1000 $\mu\text{L}/\text{min}$	3000 $\mu\text{L}/\text{min}$	150 $^{\circ}\text{C}$
(a)	0.05 M	0.50 M		
(b)	0.05 M	1.00 M		
ii	Zn(Ac) <sub>2</sub> /EtOH	LiOH/EtOH	PP9 <sup>b</sup>	
Flow rate	350 $\mu\text{L}/\text{min}$	350 $\mu\text{L}/\text{min}$	1500 $\mu\text{L}/\text{min}$	RT (20 $^{\circ}\text{C}$ )
(c)	0.02 M	0.04 M		
(d)	0.02 M	0.15 M		
<sup>a</sup> TD: tetradecane				
<sup>b</sup> PP9: perfluoromethyldecalin (C <sub>11</sub> F <sub>20</sub> )				

The SEM images of ZnO microparticles (a) and (b) are presented in Fig. 3.20a, b. The formation of uniform, flower-shaped particles can be observed. The average length of the flower branch changed from 0.15  $\mu\text{m}$  (Fig. 3.20a) to 1.38  $\mu\text{m}$  (Fig. 3.20b). Fig. 3.20c, d presents the TEM images of ZnO nanoparticles prepared under condition (ii). The mean particle diameter in sample d was about 3.9 nm, which was smaller than that in sample c (4.6 nm).

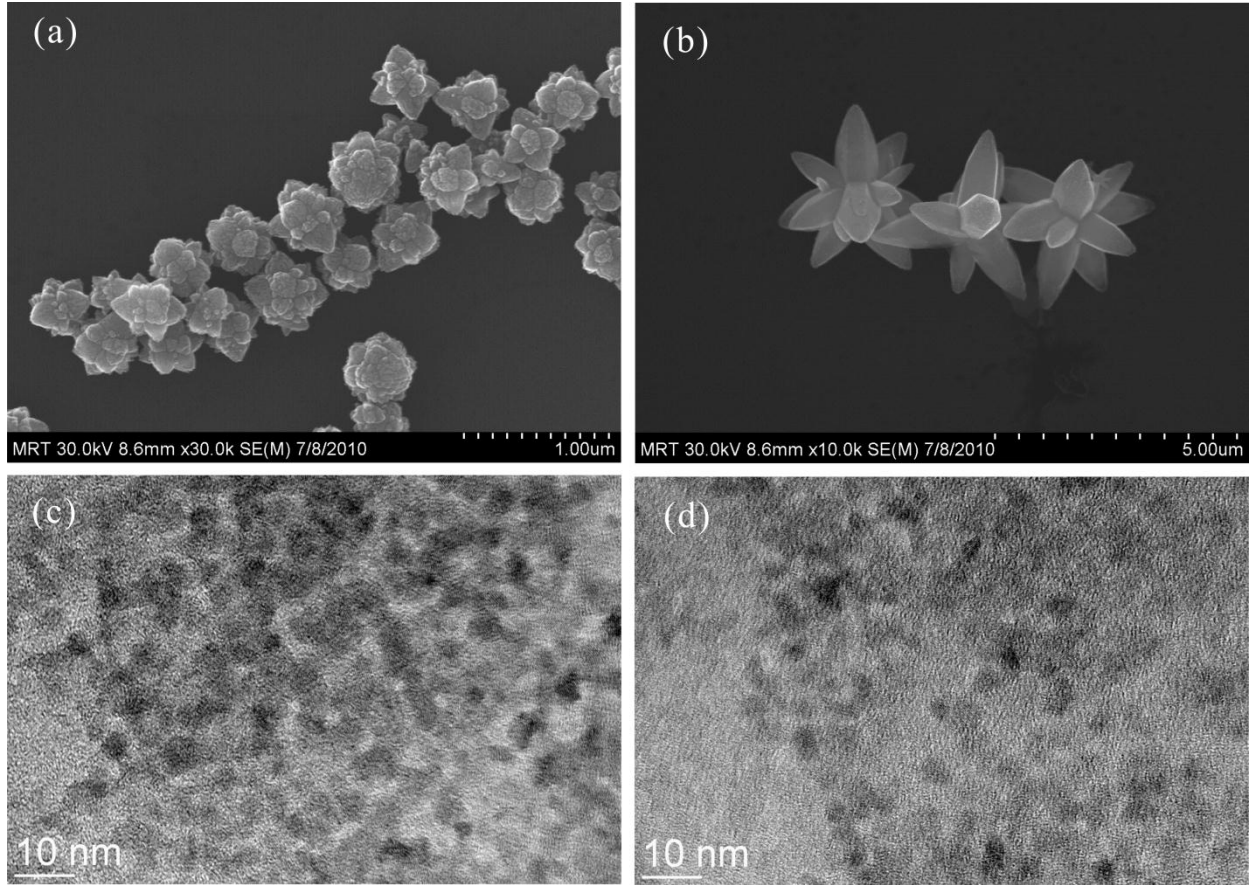


**Fig. 3.20** SEM images of ZnO microparticles (a) and (b) under experimental condition (i) and TEM images of ZnO nanoparticles (c) and (d) under experimental condition (ii).

SAXS was also applied to determine the diameters of the ZnO nanoparticles in order to compare the results with the TEM data. The SAXS analysis of the particle size was based on Guinier approximation for low scattering angles [195]:

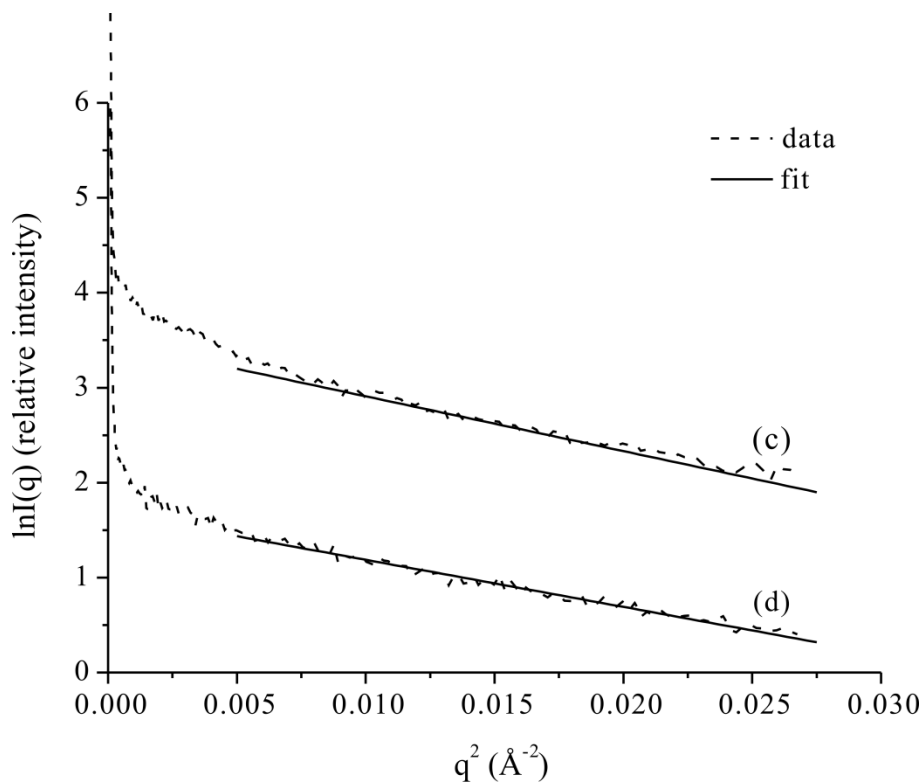
$$I(q) = (\Delta\rho)^2 V^2 \exp(-q^2 R_g^2/3) \quad (3.4)$$

where  $\Delta\rho$  is the electron density difference,  $V$  is the volume of the particle,  $R_g$  is the Guinier gyration radius and  $q$  is the scattering vector.

$R_g$  can be obtained from Guinier plots ( $\ln I(q)$  vs.  $q^2$ ) and the particle diameter  $D$  can be calculated by assuming the particle shape is spherical [196-197]:

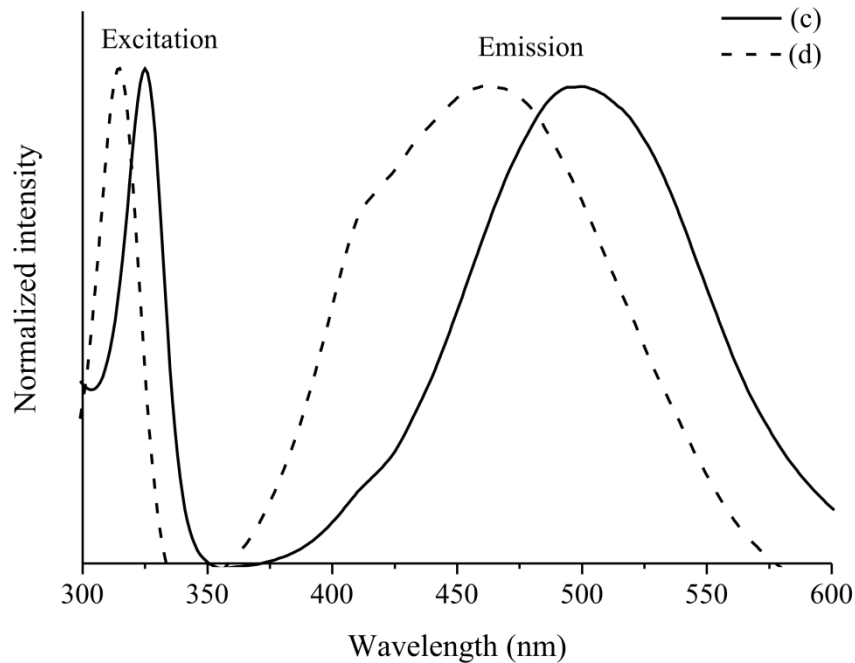
$$D = 2 \sqrt{\frac{5}{3}} R_g \quad (3.5)$$

Fig. 3.21 shows the Guinier plots for the ZnO nanoparticles.  $R_g$  was determined from the slope of the fit line (solid line) within  $0.001 \text{ \AA}^{-2} < q^2 < 0.0045 \text{ \AA}^{-2}$  and  $0.002 \text{ \AA}^{-2} < q^2 < 0.0065 \text{ \AA}^{-2}$  for nanoparticles c and d, respectively. The diameters of the nanoparticles calculated according to equation (3.5) were 5.0 nm and 4.2 nm for ZnO nanoparticles (c) and (d), respectively. The SAXS results were close to the diameters obtained from the TEM measurements.



**Fig. 3.21** Guinier plots corresponding to the SAXS patterns for ZnO nanoparticles (c) and (d). The dotted and the solid lines are the experimental data and the fit lines, respectively.

The normalized photoluminescence (PL) spectra of ZnO nanoparticles in ethanol are shown in Fig. 3.22c, d, which exhibited green and blue emission at 500 nm and 463 nm under excitation at 325 nm, respectively. Apparently, their emission peaks blue shifted as their particle size decreased from 5.0 nm to 4.2 nm. The excitation peaks also shifted from 325 nm (c) to 315 nm (d). Such relationship between particle size and emission color has been reported in the literatures [198-202].



**Fig. 3.22** Photoluminescence spectra of ZnO nanoparticles (c) and (d) in ethanol solution. The emission spectra were obtained under 325 nm excitation and the excitation spectra were obtained by setting the observation wavelength at its corresponding emission peak (500 nm and 462 nm for samples c and d, respectively).

Although various visible emission spectra from ZnO nanoparticles have been detected by different methods, the nature of the visible emission is still not fully understood. In order to explore the mechanism of the size-dependent visible optical properties of ZnO particles, EXAFS spectroscopy was employed to study their local structures and to compare it with that of ZnO microparticles. Fig. 3.23 shows the EXAFS results for ZnO micro (sample a, b) and nanoparticles (sample c, d) as a function of the photoelectron wave number  $k$ . We can observe that the amplitudes of the oscillations became smaller and the features of the curves were drastically diminished as the particle size was reduced from micrometer to nanometer. This can be attributed to larger structural disorder in ZnO nanoparticles.

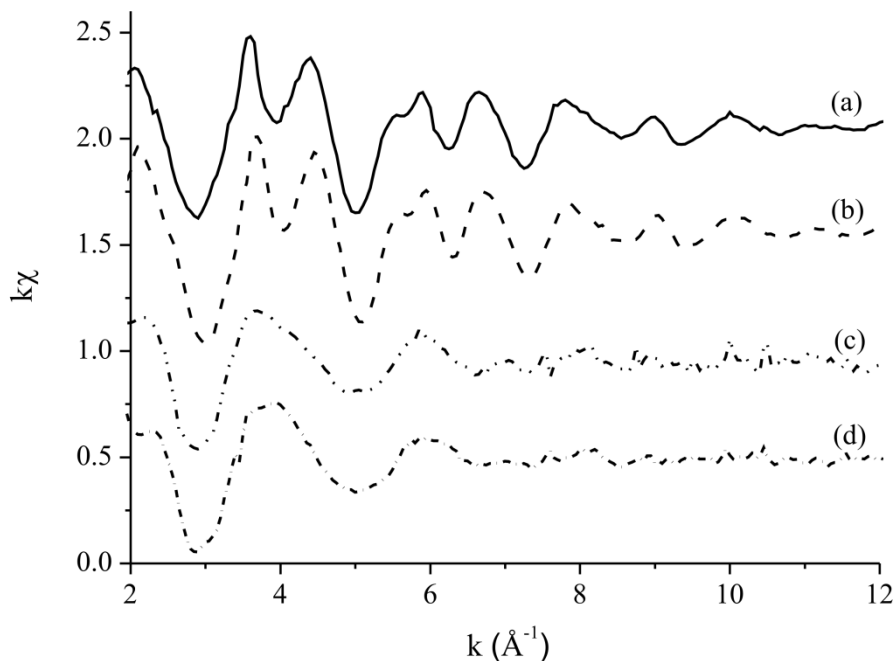


**Fig. 3.23** EXAFS from ZnO micro (a, b) and nanoparticles (c, d) as a function of the photoelectron wave number  $k$  at room temperature.

For a quantitative comparison of the local structure properties of the ZnO micro and nanoparticles, the XAFS data was Fourier transformed into  $r$  space and fitted to theoretical EXAFS calculations [203], shown in Fig. 3.24. The first peaks at  $\sim 1.5 \text{ \AA}$  correspond to the first coordination shell of oxygen, and the second peaks at  $\sim 2.8 \text{ \AA}$  are due to the second coordination shell of Zn. The magnitude of the first peaks from ZnO nanoparticles (Fig. 3.24c, d) is slightly reduced while the second peaks are significantly damped compared to those of ZnO microparticles (Fig. 3.24a, b), which is in accordance with a previous report [192].

The best fit results are summarized in Table 3.6. The errors for  $N$ ,  $d$  and  $\sigma^2$  were within  $\pm 0.6 \%$ ,  $\pm 0.0002 \text{ \AA}$  and  $\pm 1.0 \%$ , respectively and they were negligible. A commercial ZnO powder with a purity of 99.99 % was used as reference for the fit study. According to Tran *et al.*[191], in a wurtzite structure of ZnO unit cell, every Zn atom is surrounded by 4 oxygen atoms (first shell) and 12 zinc atoms (second shell). The fit results indicate that both ZnO micro and nanoparticles had almost full coordination number for the Zn-O pair. However, the  $\sigma^2$  value of ZnO nanoparticles (c, d) was around 1.8 times larger than that of ZnO microparticles (a, b) and

powder. It is well known that the Debye-Waller factor takes into account both thermal and static disorders. Therefore, larger  $\sigma^2$  values suggest a considerable degree of structural disorder in the Zn-O pairs for ZnO nanoparticles.

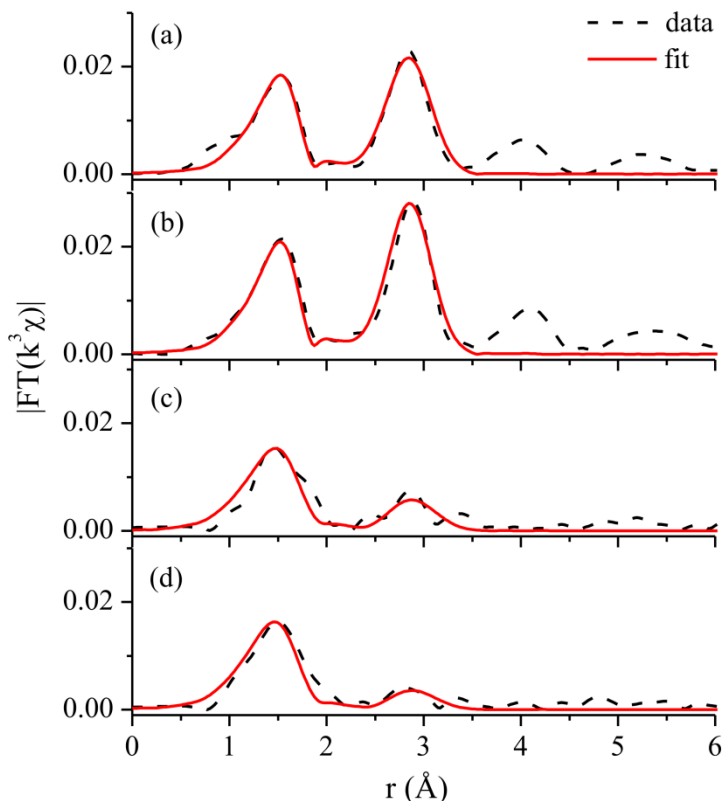


**Fig. 3.24** Magnitude of Fourier transformed EXAFS from ZnO micro (a, b) and nanoparticles (c, d) as a function of the distance from a Zn atom. The dotted and the solid lines are the experimental data and the best fit, respectively. Data in the range of  $r = 1.1\text{-}3.5$  Å were used for the fit.

The fits for the Zn-Zn pairs showed high vacancy for ZnO nanoparticles since there were only 2.81 and 1.80 Zn atoms for nanoparticle c and d, respectively. In comparison, there were around 11 Zn atoms for ZnO microparticles. For ZnO nanoparticles with diameter of around 4-5 nm, the reduction of coordination number induced by surface truncation is negligible. Thus, the reduction of the coordination number can be ascribed only to the presence of vacancies. It resulted in a great enhancement of disorder in the crystal structure [192]. In addition, the bond length of the Zn-Zn pairs for ZnO nanoparticles was slightly elongated compared to ZnO powder and microparticles. It also implied that there was a considerable amount of bond length distortion

existing in the second coordination shell for ZnO nanoparticles.

**Table 3.6** Fit results for ZnO micro and nanoparticles. Zn-O pair is the first coordination shell and Zn-Zn pair is the second coordination shell. N is the coordination number, d is the distance between the central Zn atom and the atoms in the corresponding coordination shell and  $\sigma^2$  is the Debye-Waller factor. For the model calculation, lattice constants of  $a = b = 3.2501 \text{ \AA}$ ,  $c = 5.2071 \text{ \AA}$  were used.

Sample	Zn-O			Zn-Zn		
	N	d ( $\text{\AA}$ )	$\sigma^2$ ( $\text{\AA}^2$ )	N	d ( $\text{\AA}$ )	$\sigma^2$ ( $\text{\AA}^2$ )
Powder	4.02	1.9640	0.0040	11.26	3.2081	0.0075
(a)	3.83	1.9750	0.0044	11.04	3.2126	0.0083
(b)	4.03	1.9637	0.0040	11.34	3.2069	0.0070
(c)	3.92	1.9877	0.0074	2.81	3.2371	0.0076
(d)	3.97	1.9746	0.0072	1.80	3.2383	0.0081

By combining EXAFS data with SAXS results, it shows that a decrease in ZnO nanoparticles size from 5.0 nm to 4.2 nm led to a higher vacancy in the second coordination shell, and increased Zn-Zn bond length. These vacancies and distortions in the local structures of ZnO nanoparticles could contribute to the blue shift of their visible emission.

In summary, the experiments demonstrate that the micro segmented flow technique is suitable for continuous flow synthesis of ZnO particles. It is also the first demonstration of ZnO nanoparticles prepared by micro continuous flow synthesis at room temperature. Due to the low concentration of the ZnO nanoparticles solution, the crystal structure of formed nanoparticles has not been analysed by XRD. Therefore, other species inside the product solution except for ZnO nanoparticles is unknown. The synthesized ZnO nanoparticles exhibited interesting emission colors changing from green to blue as the particle size decreased. The EXAFS measurements indicated high vacancies and a large degree of structural disorder in the nanoparticles compared to the microparticles. These structural changes should affect the visible emission of ZnO nanoparticles.

### 3.5 Synthesis and characterization of ZnO composite particles

Semiconductor-metal composite materials have attracted considerable attention due to their potential applications in diverse areas such as photocatalysis [204-205], solar energy conversion [206], nonlinear optics [207] and chemical sensing [208-209]. Recently, ZnO-metal composites have gained more interest since these materials are able to combine the excellent performance of ZnO in optics, electronics and photonics with the efficient surface plasmon resonance of metals. Different strategies have been explored to obtain ZnO-metal composite with various morphologies, such as oxidation of Zn alloy melts [210], growing metal nanoparticles by chemical reduction [55] or photoreduction [211], seed-mediated growth method [204] and combined thermal evaporation and sputtering [93]. In this section, solution-based method and a simple assembly strategy have been applied to prepare ZnO-Au assemblies since they are very easy to operate and do not require high temperature. The formed ZnO/Au composite particles have been characterized by SEM, UV/Vis absorption spectroscopy and Raman spectroscopy.

#### 3.5.1 Solution-based method

The ZnO flower-like microparticles were prepared by  $\text{Zn}(\text{Ac})_2$  and NaOH in the mixture solvent of water and ethylene glycol (EG) by use of the set-up IV described in section 2.1. The detailed experimental conditions to prepare ZnO particles are provided in Table 3.7. The formation of ZnO particles was carried out with total flow rate of 5000  $\mu\text{L}/\text{min}$  at 150  $^\circ\text{C}$ .

**Table 3.7** Experimental conditions for synthesis of ZnO flower-like microparticles.

	$\text{Zn}(\text{Ac})_2/\text{EG}^a$	NaOH/EG	$\text{H}_2\text{O}$	Carrier medium	T
Conc.	0.1 M	2.0 M	TD <sup>b</sup>	TD <sup>b</sup>	150 $^\circ\text{C}$
Flow rate	500 $\mu\text{L}/\text{min}$	500 $\mu\text{L}/\text{min}$	1000 $\mu\text{L}/\text{min}$	3000 $\mu\text{L}/\text{min}$	
<sup>a</sup> EG: ethylene glycol					
<sup>b</sup> TD: tetradecane					

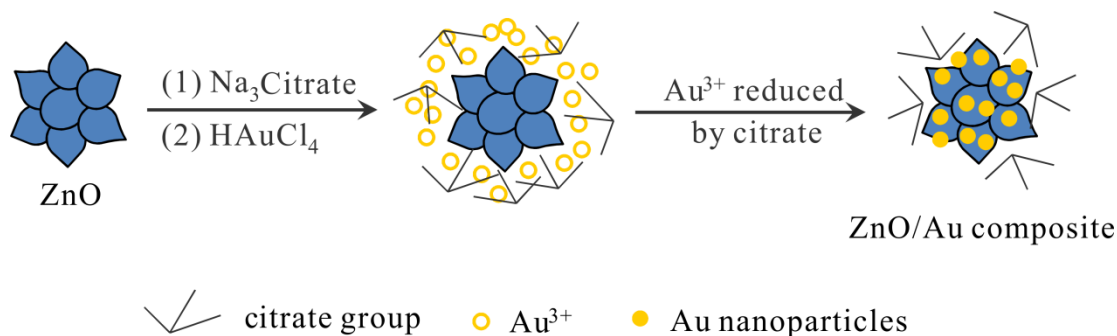


**Fig. 3.25** Schematic illustration of the synthesis of ZnO/Au composite particles.

The scheme of preparation of ZnO/Au composite particles is illustrated in Fig. 3.25. First at all, the prepared ZnO particles were dispersed in sodium citrate aqueous solution to obtain citrate-protected ZnO particles. Then  $\text{HAuCl}_4$  solution was added and mixed with it. The formation of ZnO/Au composite particles were realized by nucleation and growth of reduced Au nanoparticles on the surface of ZnO particles.

The SEM images of ZnO microparticles are shown in Fig. 3.20a, b. It can be seen that the ZnO flower-like particles were composed of different number of branches and their diameter was around 700 nm. ZnO/Au composite particles with varying amounts of Au nanoparticles are presented in Fig. 3.20c-f. The SEM images have clearly shown that Au nanoparticles with average diameter of around 36 nm were deposited on the surface of ZnO particles. However, the shape and size distribution of Au nanoparticles were not uniform and homogeneous. Some of them were aggregates which were made up of small Au nanoparticles. When the molar ratio ZnO to Au was decreased from 25/1 to 10/1, more Au nanoparticles were found on the surface of ZnO particles.

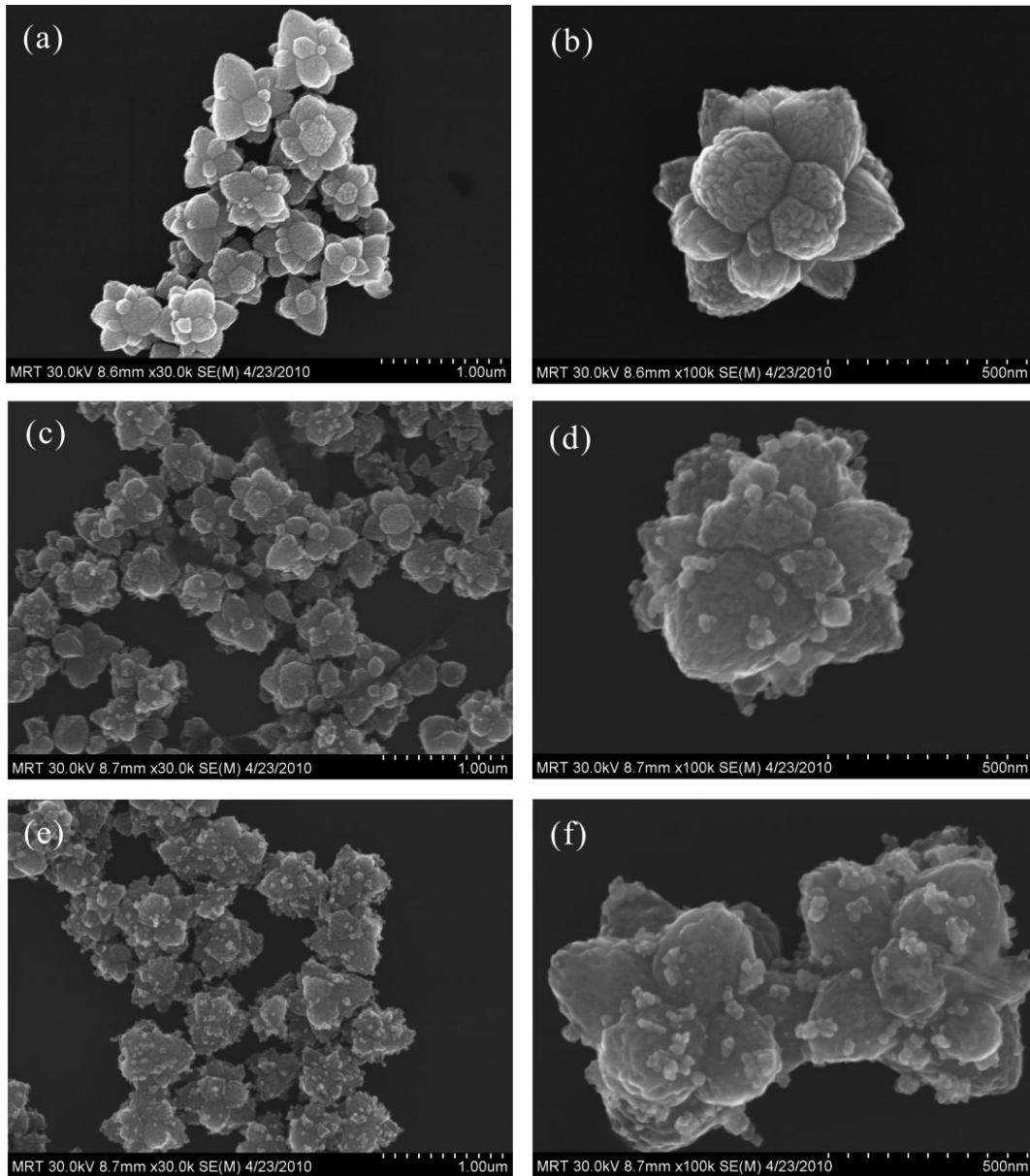


**Fig. 3.26** SEM images of ZnO (a, b) and ZnO/Au composite particles with different molar ratios of ZnO to Au: (c, d) 25/1; (e, f) 10/1.

The optical properties of the synthesized ZnO and ZnO/Au composite particles are investigated by UV/Vis spectra shown in Fig. 3.27. A weak, broad band between 520 nm and 600 nm (Fig. 3.27c) shows the plasmon resonance peak of Au nanoparticles in ZnO/Au composite particles with molar ratio of ZnO to Au of 10/1. Similar peak was not observed in Fig. 3.27b since less Au nanoparticles were deposited on the surface of ZnO particles.

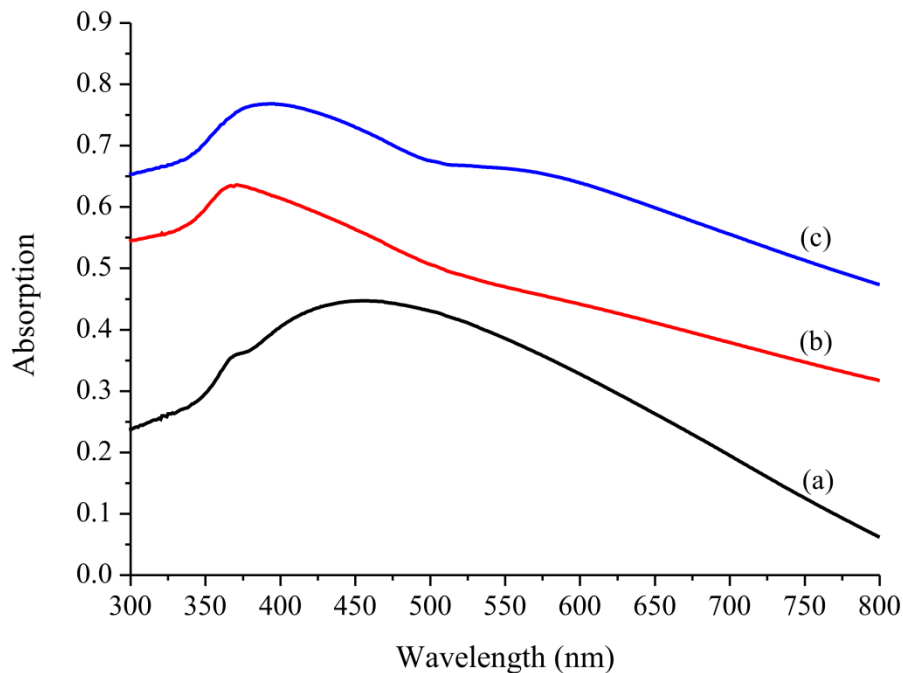


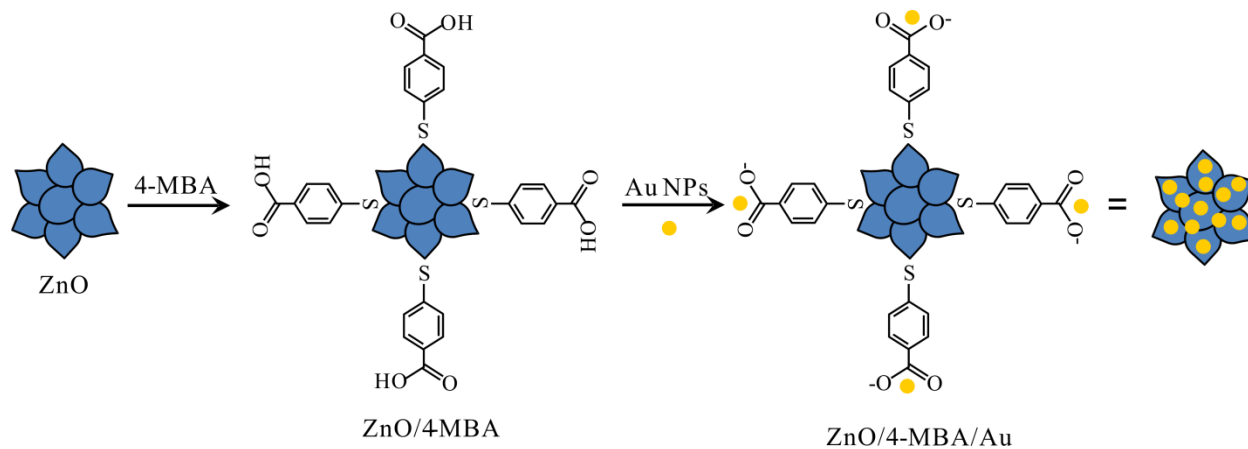
**Fig. 3.27** UV/Vis spectra of ZnO particles (a) and ZnO/Au composite particles with different molar ratios of ZnO/Au: (b) 25/1; (c) 10/1.

### 3.5.2 Assembly method

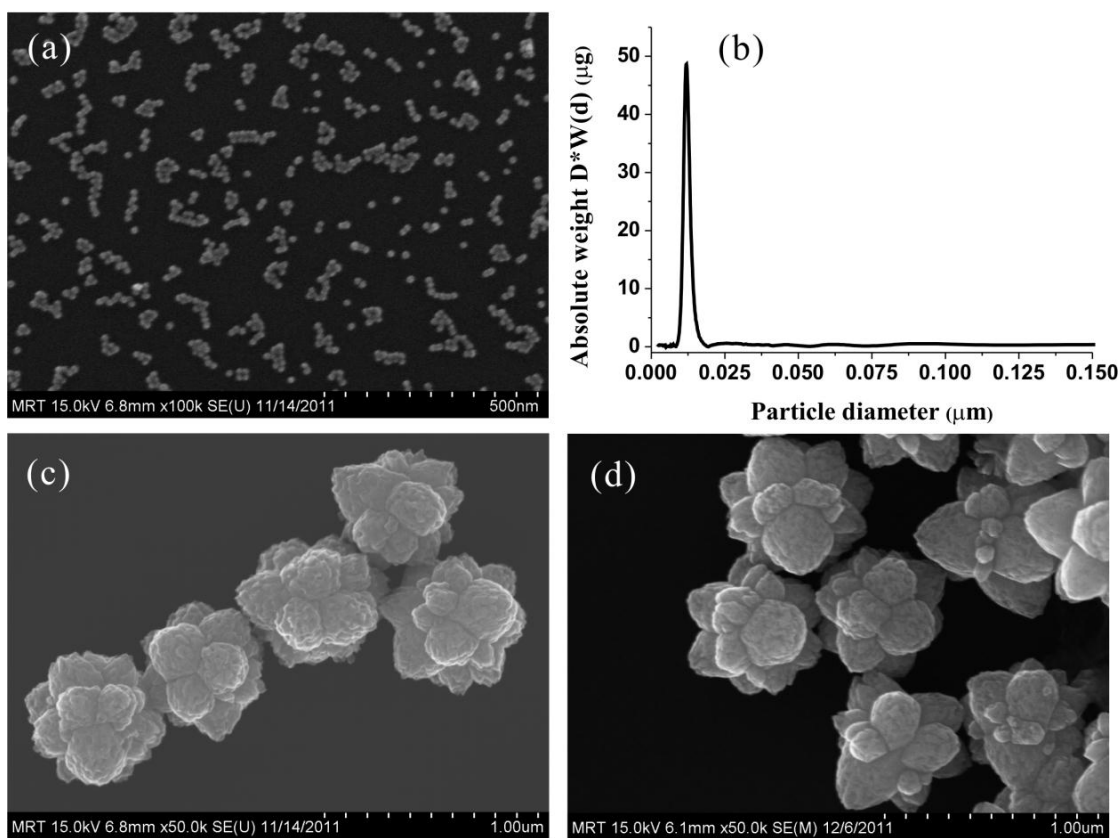
In order to synthesize composite particles with more homogeneous shape and size, another assembly strategy has been applied to prepare ZnO/4-mercaptopbenzoic acid (4-MBA)/Au composite particles. The absorption spectra and Raman scattering of the formed particles have been investigated. To the best of our knowledge, this is the first investigation about synthesis and characterization of ZnO/4-MBA/Au composite particles.

Fig. 3.28 schematically illustrates the preparation method for ZnO/4-MBA/Au composites. In the first step, the flower-like ZnO particles were obtained by micro segmented flow synthesis and detailed experimental condition is shown in section 3.5.1. Then the prepared ZnO particles were mixed with 4-MBA ethanol solution at room temperature. The adsorption of 4-MBA molecules on ZnO particles is likely through the thiol group to form ZnO/4-MBA particles. In the second step, the 4-MBA modified ZnO particles were mixed with three different amounts of Au nanoparticles prepared in batch to obtain ZnO/4-MBA/Au composite particles with different

coverage of Au nanoparticles on the surface. The detailed characterization is discussed later.



**Fig. 3.28** Schematic illustration of the synthesis method for ZnO/4-MBA/Au composites.



**Fig. 3.29** SEM image of (a) Au nanoparticles with (b) corresponding DCS spectrum. SEM images of (c) ZnO microparticles and (d) ZnO/4-MBA particles.

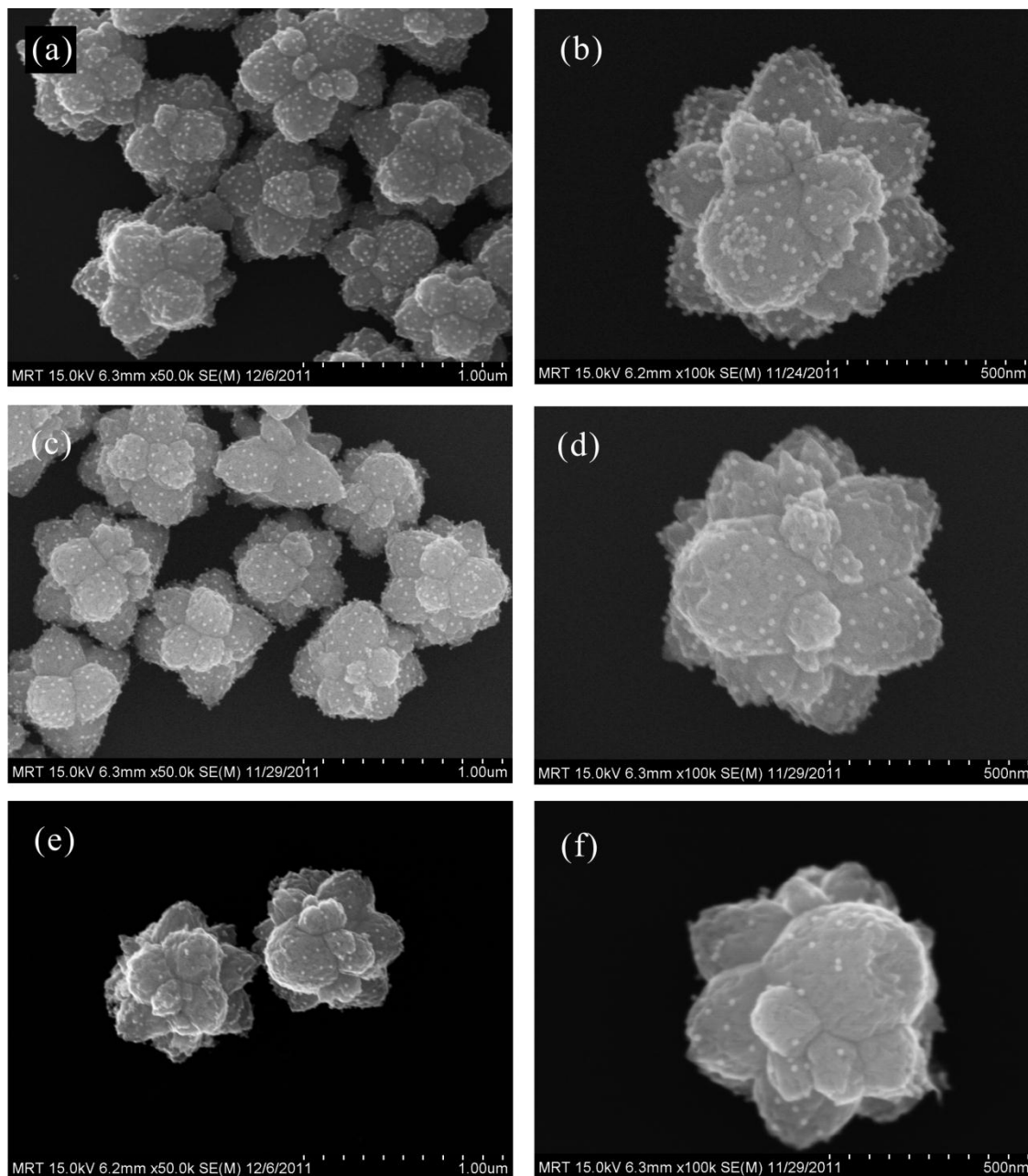


**Fig. 3.30** SEM images of ZnO/4-MBA/Au composites with different molar ratios of ZnO/4-MBA to Au: (a, b) 10/1; (c, d) 20/1; (e, f) 40/1.

The SEM image of formed Au nanoparticles is shown in Fig. 3.29a. Spherical Au nanoparticles with very homogeneous shape and size were observed. The particle size distribution of Au nanoparticles was analyzed by DCS spectra shown in Fig. 3.29b. The peak position indicates the mean particle size, while the half width of the distribution function represents the particle size distribution [146]. The DCS spectra showed that the obtained Au nanoparticles had a mean

diameter of 12.0 nm with a size distribution of 2.7 nm.

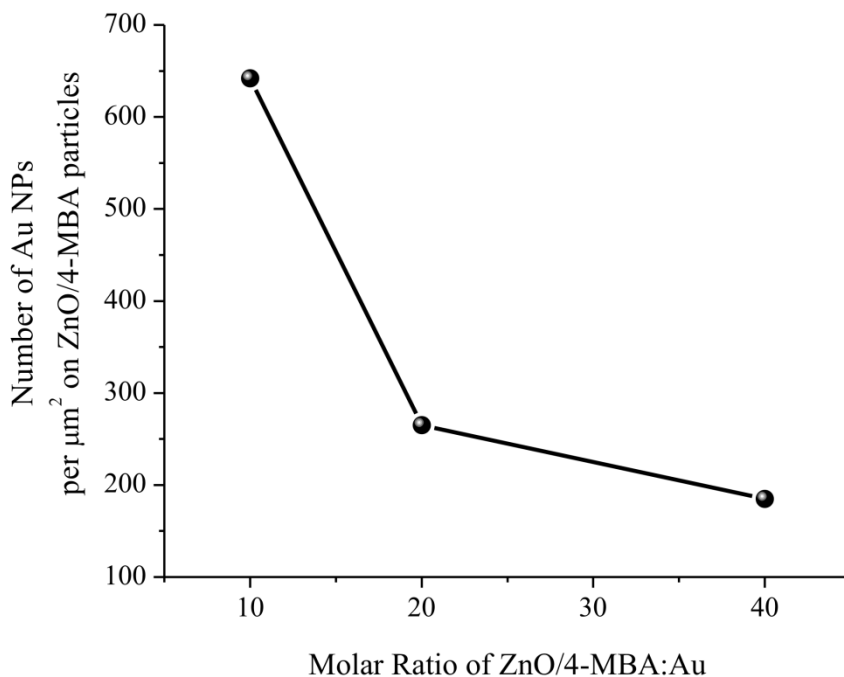


**Fig. 3.31** Number of Au nanoparticles per  $\mu\text{m}^2$  adsorbed on the surface of ZnO/4-MBA particles as a function of the molar ratios of ZnO/4-MBA to Au.

The SEM image of the formed ZnO particles is shown in Fig. 3.29c. We can observe that the ZnO flower-like particles had very homogeneous shape and size. They were composed of different number of branches and their diameter was around 700 nm. After adsorption of 4-MBA on ZnO surface, no apparent structural changes were observed on the assembled ZnO particles shown in Fig. 3.29d.

The SEM images of ZnO/4-MBA/Au composites are presented in Fig. 3.30. It is clearly shown that Au nanoparticles were homogeneously distributed on the surface of ZnO/4-MBA particles. This indicates that 4-MBA molecules have been successfully immobilized on the surface of ZnO particles. In addition, the coverage of Au nanoparticles can be adjusted by varying the molar ratio of ZnO/4-MBA to Au. When this ratio was increased from 10/1 to 40/1, less Au nanoparticles were observed on ZnO surface. By use of the SEM images with higher magnification, we were able to count the number of the Au nanoparticles adsorbed on the surface

of ZnO/4-MBA particles. As shown in Fig. 3.31, about 642 Au nanoparticles per  $\mu\text{m}^2$  were absorbed on the particles surface when molar ratio of ZnO/4-MBA to Au was 10/1. This number drastically reduced to 185 when molar ratio of ZnO/4-MBA to Au was enhanced to 40/1.

Fig. 3.32 shows the UV/Vis absorption spectra of Au nanoparticles, ZnO particles and composite particles with molar ratio of ZnO/4-MBA: Au = 10:1. The Au nanoparticles exhibited a maximum absorption wavelength at 518 nm. For flower-like ZnO particles, a weak absorption peak centered at about 368 nm was detected. No obvious change of absorption spectra was observed after modification of ZnO surface with 4-MBA molecule. However, a broad band at around 521 nm was found in the absorption spectra of composite particles when molar ratio of ZnO/4-MBA: Au was 10:1, which indicated the presence of Au nanoparticles on ZnO/4-MBA particles.

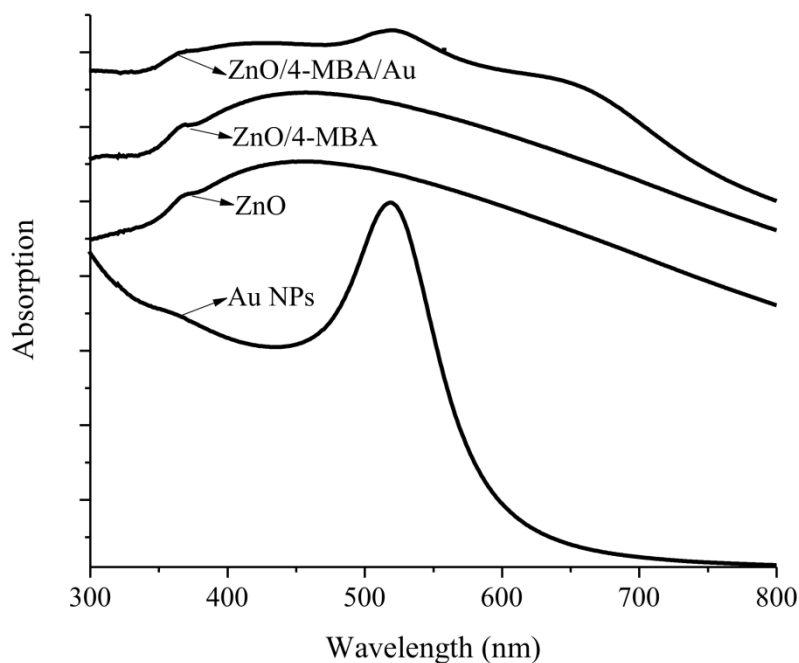


**Fig. 3.32** UV/Vis spectra of Au nanoparticles, ZnO particles, ZnO/4-MBA and composites particles with molar ratio of ZnO/4-MBA: Au = 10:1.

In order to investigate which functional group of 4-MBA molecule was attached to ZnO particles, Raman spectroscopy was applied to analyse the obtained particles. Fig. 3.33 shows the

Raman spectra of 4-MBA powder. The predominant peaks located at 1097 and 1594  $\text{cm}^{-1}$  corresponded to  $\nu_{8a}$  ( $a_1$ ) and  $\nu_{12}$  ( $a_1$ ) aromatic ring characteristic vibrations, respectively [212-213]. Other weak bands which were visible in the spectra can be attributed to the bending of the CH groups on the aromatic ring at 1181  $\text{cm}^{-1}$  and the stretching associated with  $\text{COO}^-$  group at 1450  $\text{cm}^{-1}$  [214]. The band at 2564  $\text{cm}^{-1}$  was assigned to the SH stretching vibration [215], which was absent in the Raman spectra of ZnO/4-MBA (see the insert image in Fig. 3.33). This implies that 4-MBA molecule was bound to ZnO particles through the thiol group.

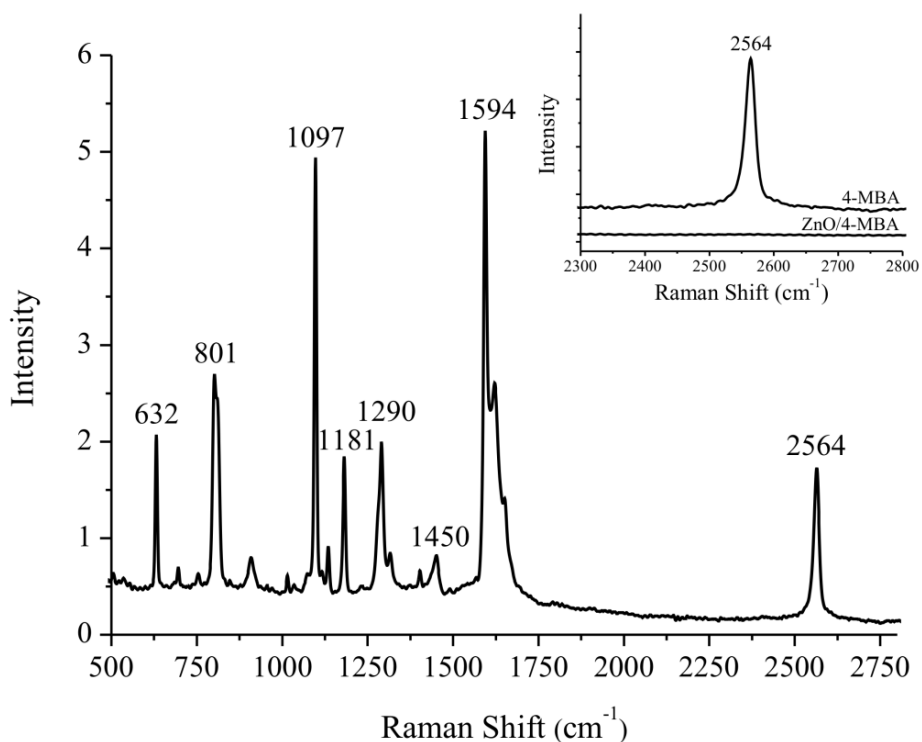


**Fig. 3.33** Raman spectrum of 4-MBA powder. The insert graph shows the part of Raman spectrum of 4-MBA and ZnO/4-MBA.

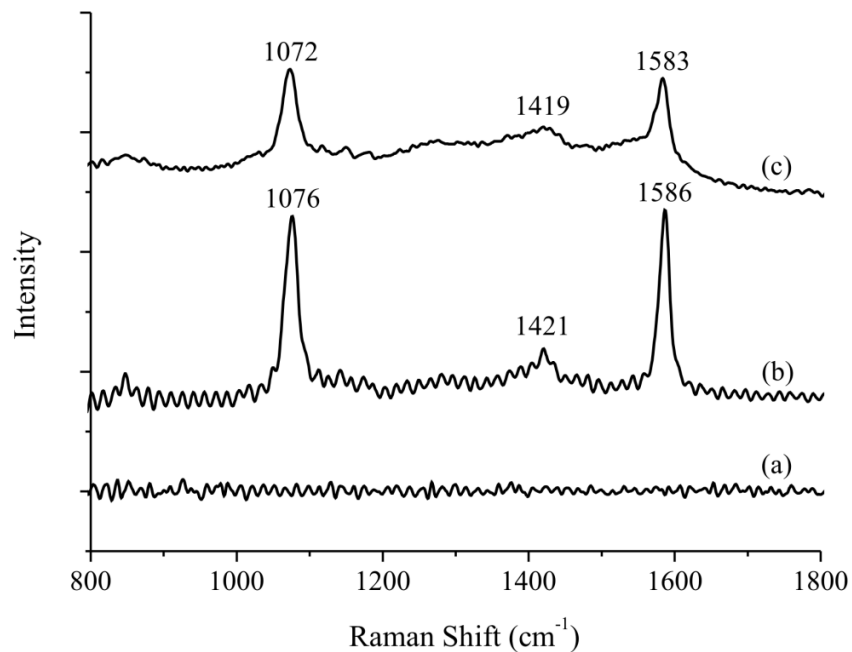


**Fig. 3.34** Raman spectrum of (a) ZnO, (b) ZnO/4-MBA and (c) ZnO/4-MBA/Au with molar ratio of ZnO/4-MBA: Au = 10:1.

From Fig. 3.34a, we can observe that there was almost no Raman intensity for the ZnO microparticles. However, the Raman spectra of ZnO/4-MBA particles in Fig. 3.34b reveals the aromatic ring breathing modes at 1076 cm<sup>-1</sup> and 1586 cm<sup>-1</sup>, which were significantly red shifted by 21 cm<sup>-1</sup> and 8 cm<sup>-1</sup>, respectively, compared to Raman spectra of 4-MBA molecules. In addition, the bandwidths were also broadened by around 20 cm<sup>-1</sup>. It is known from the literature [216-218] that when a benzene ring adsorbs on a metal surface via its  $\pi$  system, the benzene ring breathing modes are red shifted by more than 10 cm<sup>-1</sup> along with substantial band broadening. The red shift arises from the bond weakening in the benzene ring system caused by the backdonation of the metal  $d$  electrons to the benzene ring antibonding  $\pi^*$  orbitals [216-217]. The increase of the bandwidth was caused by additional vibrational relaxation due to interaction between the metal surface and the benzene ring. In the case of ZnO/4-MBA particles, the substantial red shift and the band broadening indicate that 4-MBA molecules were effectively bonded to the surface of ZnO particles and there was strong interaction between them. In the Raman spectra of the ZnO/4-MBA/Au composite shown in Fig. 3.34c, it is interesting to note that both of the dominant bands slightly red shifted by 3-4 cm<sup>-1</sup> compared to that of ZnO/4-MBA

particles, implying that the direct interaction between Au  $d$  electrons and benzene ring  $\pi^*$  orbital was relatively low.

In summary, a simple solution-based method has been applied to prepare ZnO/Au composite particles. However, the quality of the product produced by this method was not high. In contrast, the ZnO/4-MBA/Au composite particles with homogeneous shape and size have been successfully synthesized by an assembly strategy for the first time. The surface coverage of Au nanoparticles can be easily tuned by changing the molar ratios of ZnO/4-MBA to Au. Raman spectra indicate that ZnO particles were bound to 4-MBA through thiol group. The red shift of Raman spectra in ZnO/4-MBA and ZnO/4-MBA/Au particles indicate that the interaction between 4-MBA molecules and ZnO particles was stronger than that between 4-MBA molecules and Au particles.

## 4 Conclusion and outlook

This dissertation leads to the following major conclusions:

- The micro segmented flow technique is suitable to precisely control the reaction conditions and produce ZnO particles with well-defined shape and size.
- The enhanced convective mass and heat transfer induced by higher flow rate allows the formation of ZnO particles with higher homogeneity.
- Hydrothermal synthesis can be perfectly applied to the micro reaction system for the formation of high quality ZnO particles with controlled size (400 nm-3.5  $\mu\text{m}$ ) and different morphologies (flower-like, star-like, cylinder-like and spherical).
- The reactant concentration and molar ratio of the reactants have a strong effect on the size, size distribution and aspect ratio of the produced ZnO particles.
- The water content plays an important role on the quality of the ZnO particles prepared in water/EG binary solvent. At lower water content, quasi-spherical particles with smaller size were obtained, while nut-like and ellipsoidal particles with increased particle size were formed at higher water content.
- ZnO nanoparticles can also be prepared in the micro segmented flow system, and they have shown interesting visible emissions. The EXAFS measurements of ZnO micro and nanoparticles reveal a high number of vacancies and a large degree of structural disorders in the nanoparticles than that of the microparticles.
- The prepared ZnO flower-like microparticles have been applied to prepare ZnO/4-MBA/Au composite particles with very homogeneous shape and size by a simple strategy.

Outlook:

- Study the formation mechanism of ZnO particles in microfluidic system
- Investigation of the catalytic application of the synthesized ZnO and ZnO composite particles

## 5 References

- [1] Pearton, S. J.; Norton, D. P.; Ip, K.; Heo, Y. W.; Steiner, T., Recent progress in processing and properties of ZnO. *Superlattices and Microstructures* **2003**, *34* (1-2), 3-32.
- [2] Wang, Z. L., Zinc oxide nanostructures: growth, properties and applications. *Journal of Physics-Condensed Matter* **2004**, *16* (25), R829-R858.
- [3] Djuricic, A. B.; Leung, Y. H., Optical properties of ZnO nanostructures. *Small* **2006**, *2* (8-9), 944-961.
- [4] Djuricic, A. B.; Ng, A. M. C.; Chen, X. Y., ZnO nanostructures for optoelectronics: Material properties and device applications. *Progress in Quantum Electronics* **2010**, *34* (4), 191-259.
- [5] Gao, P. Piezoelectric nanostructures of zinc oxide: Synthesis, characterization and devices. Georgia Institute of Technology, Atlanta, **2005**.
- [6] Xu, J. Q.; Pan, Q. Y.; Shun, Y. A.; Tian, Z. Z., Grain size control and gas sensing properties of ZnO gas sensor. *Sensors and Actuators B-Chemical* **2000**, *66* (1-3), 277-279.
- [7] Fuller, M. L., A method of determining the axial ratio of a crystal from x-ray diffraction data the axial ratio and lattice constants of zinc oxide. *Science* **1929**, *70*, 196-198.
- [8] Bunn, C. W., The lattice-dimensions of zinc oxide *Proceedings of the Physical Society* **1935**, *47* (5), 835-842.
- [9] Mollwo, E., Die Wirkung von Wasserstoff auf die Leitfähigkeit und Lumineszenz von Zinkoxydkristallen. *Zeitschrift Fur Physik* **1954**, *138* (3-4), 478-488.
- [10] Damen, T. C.; Porto, S. P. S.; Tell, B., Raman effect in zinc oxide. *Physical Review* **1966**, *142* (2), 570-574.
- [11] Claus Franz Klingshirn; Bruno K. Meyer; Andreas Waag; Axel Hoffmann; Geurts, J. M. M., *Zinc Oxide: From Fundamental Properties Towards Novel Applications*. Springer: **2010**; Vol. 120.
- [12] Look, D. C.; Claflin, B., P-type doping and devices based on ZnO. *physica status solidi (b)* **2004**, *241* (3), 624-630.
- [13] Ozgur, U.; Alivov, Y. I.; Liu, C.; Teke, A.; Reshchikov, M. A.; Dogan, S.; Avrutin, V.; Cho, S. J.; Morkoc, H., A comprehensive review of ZnO materials and devices. *Journal of Applied Physics* **2005**, *98* (4), 041301.
- [14] Klingshirn, C., ZnO: From basics towards applications. *Physica Status Solidi B-Basic Solid State Physics* **2007**, *244*, 3027-3073.

- 
- [15] Klingshirn, C.; Hauschild, R.; Priller, H.; Decker, M.; Zeller, J.; Kalt, H., ZnO rediscovered - once again!?. *Superlattices and Microstructures* **2005**, *38* (4-6), 209-222.
- [16] Wang, Z. L., ZnO nanowire and nanobelt platform for nanotechnology. *Materials Science & Engineering R-Reports* **2009**, *64* (3-4), 33-71.
- [17] Baruah, S.; Dutta, J., Hydrothermal growth of ZnO nanostructures. *Science and Technology of Advanced Materials* **2009**, *10* (1), 013001.
- [18] Izyumskaya, N.; Avrutin, V.; Ozgur, U.; Alivov, Y. I.; Morkoc, H., Preparation and properties of ZnO and devices. *Physica Status Solidi B-Basic Solid State Physics* **2007**, *244* (5), 1439-1450.
- [19] Jagadish, C.; Pearton, S. J., *Zinc oxide bulk, thin films and nanostructures: processing, properties and applications*. First ed.; Elsevier: Oxford, **2006**.
- [20] Triboulet, R., The scope of the ZnO growth. *International Conference on Solid State Crystals 2000: Growth, Characterization, and Applications of Single Crystals* **2001**, *4412*, 1-8.
- [21] Wang, Z. L., Nanostructures of zinc oxide. *Materials Today* **2004**, *7* (6), 26-33.
- [22] Norton, D. P.; Heo, Y. W.; Ivill, M. P.; Ip, K.; Pearton, S. J.; Chisholm, M. F.; Steiner, T., ZnO: growth, doping & processing. *Materials Today* **2004**, *7* (6), 34-40.
- [23] Peng, W. Q.; Qu, S. C.; Cong, G. W.; Wang, Z. G., Synthesis and structures of morphology-controlled ZnO nano- and microcrystals. *Crystal Growth & Design* **2006**, *6* (6), 1518-1522.
- [24] Lim, Y. S.; Park, J. W.; Hong, S. T.; Kim, J., Carbothermal synthesis of ZnO nanocomb structure. *Materials Science and Engineering B-Solid State Materials for Advanced Technology* **2006**, *129* (1-3), 100-103.
- [25] Byung Sun, H.; Young Rang, U.; Chang Kyu, R., Synthesis for nanoflower and rod of ZnO by a surfactant free and low temperature method. *Surface Review and Letters* **2010**, *17* (2), 173-176.
- [26] Kong, X. Y.; Ding, Y.; Yang, R.; Wang, Z. L., Single-crystal nanorings formed by epitaxial self-coiling of polar nanobelts. *Science* **2004**, *303* (5662), 1348-1351.
- [27] Kong, X. Y.; Wang, Z. L., Spontaneous Polarization-Induced Nanohelices, Nanosprings, and Nanorings of Piezoelectric Nanobelts. *Nano Letters* **2003**, *3* (12), 1625-1631.
- [28] Kong, X. Y.; Wang, Z. L., Polar-surface dominated ZnO nanobelts and the electrostatic energy induced nanohelices, nanosprings, and nanospirals. *Applied Physics Letters* **2004**, *84* (6), 975-977.
- [29] Castaneda, L., Synthesis and characterization of ZnO micro- and nano-cages. *Acta Materialia* **2009**, *57* (5), 1385-1391.
-

- [30] Lu, J. G.; Ye, Z. Z.; Huang, J. Y.; Zhu, L. P.; Zhao, B. H.; Wang, Z. L.; Fujita, S., ZnO quantum dots synthesized by a vapor phase transport process. *Applied Physics Letters* **2006**, *88* (6).
- [31] Cao, B. Q.; Li, Y.; Duan, G. T.; Cai, W. P., Growth of ZnO nanoneedle arrays with strong ultraviolet emissions by an electrochemical deposition method. *Crystal Growth & Design* **2006**, *6* (5), 1091-1095.
- [32] Yin, Z. Y.; Wu, S. X.; Zhou, X. Z.; Huang, X.; Zhang, Q. C.; Boey, F.; Zhang, H., Electrochemical Deposition of ZnO Nanorods on Transparent Reduced Graphene Oxide Electrodes for Hybrid Solar Cells. *Small* **2010**, *6* (2), 307-312.
- [33] Wu, J. J.; Liu, S. C., Low-temperature growth of well-aligned ZnO nanorods by chemical vapor deposition. *Advanced Materials* **2002**, *14* (3), 215-218.
- [34] Yang, L. L. Synthesis and Characterization of ZnO Nanostructures. Linköping University, Norrköping, **2010**.
- [35] Wikipedia: <http://en.wikipedia.org/wiki/ZnO>.
- [36] Dulub, O.; Boatner, L. A.; Diebold, U., STM study of the geometric and electronic structure of ZnO(0001)-Zn, (000(1)over-bar)-O, (10(1)over-bar0), and (11(2)over-bar0) surfaces. *Surface Science* **2002**, *519* (3), 201-217.
- [37] Meyer, B.; Marx, D., Density-functional study of the structure and stability of ZnO surfaces. *Physical Review B* **2003**, *67* (3), 039902.
- [38] Dulub, O.; Diebold, U.; Kresse, G., Novel stabilization mechanism on polar surfaces: ZnO(0001)-Zn. *Physical Review Letters* **2003**, *90* (1), 016102.
- [39] Staemmler, V.; Fink, K.; Meyer, B.; Marx, D.; Kunat, M.; Girol, S. G.; Burghaus, U.; Woll, C., Stabilization of polar ZnO surfaces: Validating microscopic models by using CO as a probe molecule. *Physical Review Letters* **2003**, *90* (10), 106102
- [40] Tasker, P. W., The stability of ionic crystal surfaces *Journal of Physics C-Solid State Physics* **1979**, *12* (22), 4977-4984.
- [41] Wander, A.; Schedin, F.; Steadman, P.; Norris, A.; McGrath, R.; Turner, T. S.; Thornton, G.; Harrison, N. M., Stability of polar oxide surfaces. *Physical Review Letters* **2001**, *86* (17), 3811-3814.
- [42] Fan, Z. Y.; Lu, J. G., Zinc oxide nanostructures: Synthesis and properties. *Journal of Nanoscience and Nanotechnology* **2005**, *5* (10), 1561-1573.
- [43] Pearton, S. J.; Norton, D. P.; Ip, K.; Heo, Y. W.; Steiner, T., Recent progress in processing and properties of ZnO. *Progress in Materials Science* **2005**, *50*, 293-340.
- [44] Hadis Morkoç, Özgür, Ü., *Zinc Oxide: Fundamentals, Materials and Device Technology*. Wiley-VCH Verlag GmbH & Co. KGaA: **2009**.

- 
- [45] Ozgur, U.; Hofstetter, D.; Morkoc, H., ZnO Devices and Applications: A Review of Current Status and Future Prospects. *Proceedings of the Ieee* **2010**, 98 (7), 1255-1268.
- [46] Hwang, D. K.; Kang, S. H.; Lim, J. H.; Yang, E. J.; Oh, J. Y.; Yang, J. H.; Park, S. J., p-ZnO/n-GaN heterostructure ZnO light-emitting diodes. *Applied Physics Letters* **2005**, 86 (22), 222101.
- [47] Yuen, C.; Yu, S. F.; Lau, S. P.; Rusli; Chen, T. P., Fabrication of n-ZnO:Al/p-SiC(4H) heterojunction light-emitting diodes by filtered cathodic vacuum arc technique. *Applied Physics Letters* **2005**, 86 (24), 241111.
- [48] Chen, P.; Ma, X.; Yang, D., Ultraviolet electroluminescence from ZnO/p-Si heterojunctions. *Journal of Applied Physics* **2007**, 101 (5), 053103.
- [49] Ohta, H.; Kamiya, M.; Kamaiya, T.; Hirano, M.; Hosono, H., UV-detector based on pn-heterojunction diode composed of transparent oxide semiconductors, p-NiO/n-ZnO. *Thin Solid Films* **2003**, 445 (2), 317-321.
- [50] Wang, C. X.; Yang, G. W.; Gao, C. X.; Liu, H. W.; Han, Y. H.; Luo, J. F.; Zou, G. T., Highly oriented growth of n-type ZnO films on p-type single crystalline diamond films and fabrication of high-quality transparent ZnO/diamond heterojunction. *Carbon* **2004**, 42 (2), 317-321.
- [51] Ya. I. Alivov; J. E. Van Nostrand; D. C. Look; M. V. Chukichev; Ataev, B. M., Observation of 430 nm electroluminescence from ZnO/GaN heterojunction light-emitting diodes. *Applied Physics Letters* **2003**, 83 (14), 2943-2945.
- [52] Lupan, O.; Pauporte, T.; Viana, B., Low-Temperature Growth of ZnO Nanowire Arrays on p-Silicon (111) for Visible-Light-Emitting Diode Fabrication. *Journal of Physical Chemistry C* **2010**, 114 (35), 14781-14785.
- [53] Look, D. C.; Claflin, B.; Alivov, Y. I.; Park, S. J., The future of ZnO light emitters. *Physica Status Solidi a-Applied Research* **2004**, 201 (10), 2203-2212.
- [54] Claus F. Klingshirn; Bruno K. Meyer; Andreas Waag; Axel Hoffmann; Geurts, J., Zinc Oxide - From Fundamental Properties Towards Novel Applications. Springer: Berlin, **2010**.
- [55] Liao, L.; Lu, H. B.; Li, J. C.; He, H.; Wang, D. F.; Fu, D. J.; Liu, C.; Zhang, W. F., Size dependence of gas sensitivity of ZnO nanorods. *Journal of Physical Chemistry C* **2007**, 111 (5), 1900-1903.
- [56] Rao, G. S. T.; Rao, D. T., Gas sensitivity of ZnO based thick film sensor to NH<sub>3</sub> at room temperature. *Sensors and Actuators B-Chemical* **1999**, 55 (2-3), 166-169.
- [57] Chang, S. J.; Hsueh, T. J.; Chen, I. C.; Huang, B. R., Highly sensitive ZnO nanowire CO sensors with the adsorption of Au nanoparticles. *Nanotechnology* **2008**, 19 (17), 175502.
-

- [58] Das, S. N.; Kar, J. P.; Choi, J. H.; Il Lee, T.; Moon, K. J.; Myoung, J. M., Fabrication and Characterization of ZnO Single Nanowire-Based Hydrogen Sensor. *Journal of Physical Chemistry C* **2010**, *114* (3), 1689-1693.
- [59] Wu, R. J.; Lin, H. L.; Chen, M. H.; Wu, T. M.; Chien, F. S. S., Application of Nanostructure ZnO for Room Working Temperature Ozone Sensor. *Sensor Letters* **2008**, *6* (6), 800-802.
- [60] Wang, C. H.; Chu, X. F.; Wu, M. W., Detection of H<sub>2</sub>S down to ppb levels at room temperature using sensors based on ZnO nanorods. *Sensors and Actuators B-Chemical* **2006**, *113* (1), 320-323.
- [61] Shishiyanu, S. T.; Shishiyanu, T. S.; Lupan, O. I., Sensing characteristics of tin-doped ZnO thin films as NO<sub>2</sub> gas sensor. *Sensors and Actuators B-Chemical* **2005**, *107* (1), 379-386.
- [62] Wan, Q.; Li, Q. H.; Chen, Y. J.; Wang, T. H.; He, X. L.; Li, J. P.; Lin, C. L., Fabrication and ethanol sensing characteristics of ZnO nanowire gas sensors. *Applied Physics Letters* **2004**, *84* (18), 3654-3656.
- [63] Gratzel, M., Applied physics - Solar cells to dye for. *Nature* **2003**, *421* (6923), 586-587.
- [64] Yang, Z. Z.; Xu, T.; Ito, Y. S.; Welp, U.; Kwoko, W. K., Enhanced Electron Transport in Dye-Sensitized Solar Cells Using Short ZnO Nanotips on A Rough Metal Anode. *Journal of Physical Chemistry C* **2009**, *113* (47), 20521-20526.
- [65] Xu, F.; Dai, M.; Lu, Y.; Sun, L., Hierarchical ZnO Nanowire–Nanosheet Architectures for High Power Conversion Efficiency in Dye-Sensitized Solar Cells. *The Journal of Physical Chemistry C* **2010**, *114* (6), 2776-2782.
- [66] Law, M.; Greene, L. E.; Johnson, J. C.; Saykally, R.; Yang, P., Nanowire dye-sensitized solar cells. *Nat Mater* **2005**, *4* (6), 455-459.
- [67] Martinson, A. B. F.; Elam, J. W.; Hupp, J. T.; Pellin, M. J., ZnO nanotube based dye-sensitized solar cells. *Nano Letters* **2007**, *7* (8), 2183-2187.
- [68] Wu, C. T.; Liao, W. P.; Wu, J. J., Three-dimensional ZnO nanodendrite/nanoparticle composite solar cells. *Journal of Materials Chemistry* **2011**, *21* (9), 2871-2876.
- [69] Irene, G. V.; Monica, L. C., Vertically-aligned nanostructures of ZnO for excitonic solar cells: a review. *Energy & Environmental Science* **2009**, *2* (1), 19-34.
- [70] Hughes, W. L. Synthesis and characterization of zinc oxide nanostructures for piezoelectric applications. Georgia Institute of Technology, Atlanta, **2006**.
- [71] Ansari, A. A.; Alhoshan, M.; Alsalhi, M. S.; Aldwayyan, A. S., Prospects of Nanotechnology in Clinical Immunodiagnosics. *Sensors* **2010**, *10* (7), 6535-6581.
- [72] P. M. Aneesh; K. A. Vanaja; Jayaraj, M. K. In *Synthesis of ZnO nanoparticles by hydrothermal method*, Proceeding of SPIE, Gaburro, Z.; Cabrini, S., Eds. **2007**, 66390J.

- 
- [73] Zhang, Y.; Mu, J., Controllable synthesis of flower- and rod-like ZnO nanostructures by simply tuning the ratio of sodium hydroxide to zinc acetate. *Nanotechnology* **2007**, *18* (7), 075606.
- [74] Yang, J. H.; Zheng, J. H.; Zhai, H. J.; Yang, L. L., Low temperature hydrothermal growth and optical properties of ZnO nanorods. *Crystal Research and Technology* **2009**, *44* (1), 87-91.
- [75] Kuo, C. L.; Kuo, T. J.; Huang, M. H., Hydrothermal Synthesis of ZnO Microspheres and Hexagonal Microrods with Sheetlike and Platelike Nanostructures. *The Journal of Physical Chemistry B* **2005**, *109* (43), 20115-20121.
- [76] Peng, Y.; Xu, A. W.; Deng, B.; Antonietti, M.; Cölfen, H., Polymer-Controlled Crystallization of Zinc Oxide Hexagonal Nanorings and Disks. *The Journal of Physical Chemistry B* **2006**, *110* (7), 2988-2993.
- [77] Feldmann, C.; Jungk, H. O., Polyol-mediated preparation of nanoscale oxide particles. *Angewandte Chemie-International Edition* **2001**, *40* (2), 359-362.
- [78] Feldmann, C., Polyol-mediated synthesis of nanoscale functional materials. *Advanced Functional Materials* **2003**, *13* (2), 101-107.
- [79] Feldmann, C.; Metzmacher, C., Polyol mediated synthesis of nanoscale MS particles (M = Zn, Cd, Hg). *Journal of Materials Chemistry* **2001**, *11* (10), 2603-2606.
- [80] Wang, Z. L.; Quan, Z. W.; Lin, J.; Fang, J. Y., Polyol-mediated synthesis and photoluminescent properties of Ce<sup>3+</sup> and/or Tb<sup>3+</sup>-doped LaPO<sub>4</sub> nanoparticles. *Journal of Nanoscience and Nanotechnology* **2005**, *5* (9), 1532-1536.
- [81] Wiley, B.; Sun, Y. G.; Mayers, B.; Xia, Y. N., Shape-controlled synthesis of metal nanostructures: The case of silver. *Chemistry-a European Journal* **2005**, *11* (2), 454-463.
- [82] Siekkinen, A. R.; McLellan, J. M.; Chen, J.; Xia, Y., Rapid synthesis of small silver nanocubes by mediating polyol reduction with a trace amount of sodium sulfide or sodium hydrosulfide. *Chemical Physics Letters* **2006**, *432* (4-6), 491-496.
- [83] Sun, Y. G.; Mayers, B.; Herricks, T.; Xia, Y. N., Polyol synthesis of uniform silver nanowires: A plausible growth mechanism and the supporting evidence. *Nano Letters* **2003**, *3* (7), 955-960.
- [84] Xiong, Y. J.; Chen, J. Y.; Wiley, B.; Xia, Y. N.; Aloni, S.; Yin, Y. D., Understanding the role of oxidative etching in the polyol synthesis of Pd nanoparticles with uniform shape and size. *Journal of the American Chemical Society* **2005**, *127* (20), 7332-7333.
- [85] Xiong, H. M., Photoluminescent ZnO nanoparticles modified by polymers. *Journal of Materials Chemistry* **2010**, *20* (21), 4251-4262.
- [86] Meulenkamp, E. A., Synthesis and growth of ZnO nanoparticles. *Journal of Physical Chemistry B* **1998**, *102* (29), 5566-5572.
-

- [87] Xiong, H. M.; Xu, Y.; Ren, Q. G.; Xia, Y. Y., Stable Aqueous ZnO@Polymer Core–Shell Nanoparticles with Tunable Photoluminescence and Their Application in Cell Imaging. *Journal of the American Chemical Society* **2008**, *130* (24), 7522-7523.
- [88] Xiong, H. M.; Wang, Z. D.; Liu, D. P.; Chen, J. S.; Wang, Y. G.; Xia, Y. Y., Bonding Polyether onto ZnO Nanoparticles: An Effective Method for Preparing Polymer Nanocomposites with Tunable Luminescence and Stable Conductivity. *Advanced Functional Materials* **2005**, *15* (11), 1751-1756.
- [89] Hung, C. H.; Whang, W. T., Effect of surface stabilization of nanoparticles on luminescent characteristics in ZnO/poly(hydroxyethyl methacrylate) nanohybrid films. *Journal of Materials Chemistry* **2005**, *15* (2), 267-274.
- [90] Xiong, H. M.; Wang, Z. D.; Xia, Y. Y., Polymerization Initiated by Inherent Free Radicals on Nanoparticle Surfaces: A Simple Method of Obtaining Ultrastable (ZnO)Polymer Core–Shell Nanoparticles with Strong Blue Fluorescence. *Advanced Materials* **2006**, *18* (6), 748-751.
- [91] Jai Il, P.; Saffari, A.; Kumar, S.; Guumlntner, A.; Kumacheva, E., Microfluidic Synthesis of Polymer and Inorganic Particulate Materials. *Annual Review of Materials Research* **2010**, *40*, 415-443.
- [92] Garstecki, P.; Fuerstman, M. J.; Stone, H. A.; Whitesides, G. M., Formation of droplets and bubbles in a microfluidic T-junction - scaling and mechanism of break-up. *Lab on a Chip* **2006**, *6* (3), 437-446.
- [93] Jahn, A.; Reiner, J. E.; Vreeland, W. N.; DeVoe, D. L.; Locascio, L. E.; Gaitan, M., Preparation of nanoparticles by continuous-flow microfluidics. *Journal of Nanoparticle Research* **2008**, *10* (6), 925-934.
- [94] Song, H.; Chen, D. L.; Ismagilov, R. F., Reactions in droplets in microfluidic channels. *Angewandte Chemie-International Edition* **2006**, *45* (44), 7336-7356.
- [95] Song, Y.; Hormes, J.; Kumar, C. S. S. R., Microfluidic synthesis of nanomaterials. *Small* **2008**, *4* (6), 698-711.
- [96] Stone, H. A.; Stroock, A. D.; Ajdari, A., Engineering flows in small devices: Microfluidics toward a lab-on-a-chip. *Annual Review of Fluid Mechanics* **2004**, *36*, 381-411.
- [97] Teh, S.-Y.; Lin, R.; Hung, L.-H.; Lee, A. P., Droplet microfluidics. *Lab on a Chip* **2008**, *8* (2), 198-220.
- [98] Gunther, A.; Jensen, K. F., Multiphase microfluidics: from flow characteristics to chemical and materials synthesis (vol 6, pg 1487, 2006). *Lab on a Chip* **2007**, *7* (3), 399-399.
- [99] Nisisako, T.; Torii, T.; Higuchi, T., Droplet formation in a microchannel network. *Lab on a Chip* **2002**, *2* (1), 24-26.

- 
- [100] Thorsen, T.; Roberts, R. W.; Arnold, F. H.; Quake, S. R., Dynamic pattern formation in a vesicle-generating microfluidic device. *Physical Review Letters* **2001**, *86* (18), 4163-4166.
- [101] Xu, J. H.; Li, S. W.; Tan, J.; Wang, Y. J.; Luo, G. S., Preparation of highly monodisperse droplet in a T-junction microfluidic device. *Aiche Journal* **2006**, *52* (9), 3005-3010.
- [102] Li, W.; Young, E. W. K.; Seo, M.; Nie, Z.; Garstecki, P.; Simmons, C. A.; Kumacheva, E., Simultaneous generation of droplets with different dimensions in parallel integrated microfluidic droplet generators. *Soft Matter* **2008**, *4* (2), 258-262.
- [103] Martin-Banderas, L.; Flores-Mosquera, M.; Riesco-Chueca, P.; Rodriguez-Gil, A.; Cebolla, A.; Chavez, S.; Ganan-Calvo, A. M., Flow focusing: A versatile technology to produce size-controlled and specific-morphology microparticles. *Small* **2005**, *1* (7), 688-692.
- [104] Schneider, T.; Zhao, H.; Jackson, J. K.; Chapman, G. H.; Dykes, J.; Haefeli, U. O., Use of Hydrodynamic Flow Focusing for the Generation of Biodegradable Camptothecin-Loaded Polymer Microspheres. *Journal of Pharmaceutical Sciences* **2008**, *97* (11), 4943-4954.
- [105] Ward, T.; Faivre, M.; Stone, H. A., Drop Production and Tip-Streaming Phenomenon in a Microfluidic Flow-Focusing Device via an Interfacial Chemical Reaction. *Langmuir* **2010**, *26* (12), 9233-9239.
- [106] Baroud, C. N.; Gallaire, F.; Dangla, R., Dynamics of microfluidic droplets. *Lab on a Chip* **2010**, *10* (16), 2032-2045.
- [107] Kohler, J. M.; Kirner, T., Nanoliter segment formation in micro fluid devices for chemical and biological micro serial flow processes in dependence on flow rate and viscosity. *Sensors and Actuators a-Physical* **2005**, *119* (1), 19-27.
- [108] Shia-Yen, T.; Lin, R.; Lung-Hsin, H.; Lee, A. P., Droplet microfluidics. *Lab on a Chip* **2008**, *8* (2).
- [109] Anna, S. L.; Bontoux, N.; Stone, H. A., Formation of dispersions using "flow focusing" in microchannels. *Applied Physics Letters* **2003**, *82* (3), 364-366.
- [110] Dreyfus, R.; Tabeling, P.; Willaime, H., Ordered and disordered patterns in two-phase flows in microchannels. *Physical Review Letters* **2003**, *90* (14), 144505.
- [111] Gu, H.; Duits, M. H. G.; Mugele, F., Droplets Formation and Merging in Two-Phase Flow Microfluidics. *International Journal of Molecular Sciences* **2011**, *12* (4), 2572-2597.
- [112] Huebner, A.; Sharma, S.; Srisa-Art, M.; Hollfelder, F.; Edel, J. B.; deMello, A. J., Microdroplets: A sea of applications? *Lab on a Chip* **2008**, *8* (8), 1244-1254.
-

- [113] Kohler, J. M.; Henkel, T.; Grodrian, A.; Kirner, T.; Roth, M.; Martin, K.; Metze, J., Digital reaction technology by micro segmented flow - components, concepts and applications. *Chemical Engineering Journal* **2004**, *101* (1-3), 201-216.
- [114] Bremond, N.; Thiam, A. R.; Bibette, J., Decompressing emulsion droplets favors coalescence. *Physical Review Letters* **2008**, *100* (2), 024501.
- [115] Mazutis, L.; Baret, J.-C.; Treacy, P.; Skhiri, Y.; Araghi, A. F.; Ryckelynck, M.; Taly, V.; Griffiths, A. D., Multi-step microfluidic droplet processing: kinetic analysis of an in vitro translated enzyme. *Lab on a Chip* **2009**, *9* (20), 2902-2908.
- [116] Song, H.; Tice, J. D.; Ismagilov, R. F., A microfluidic system for controlling reaction networks in time. *Angewandte Chemie-International Edition* **2003**, *42* (7), 768-772.
- [117] Link, D. R.; Anna, S. L.; Weitz, D. A.; Stone, H. A., Geometrically mediated breakup of drops in microfluidic devices. *Physical Review Letters* **2004**, *92* (5), 054503.
- [118] Steinbacher, J. L.; McQuade, D. T., Polymer chemistry in flow: New polymers, beads, capsules, and fibers. *Journal of Polymer Science Part a-Polymer Chemistry* **2006**, *44* (22), 6505-6533.
- [119] Malsch, D.; Kielpinski, M.; Merthan, R.; Albert, J.; Mayer, G.; Koehler, J. M.; Suesse, H.; Stahl, M.; Henkel, T.,  $\mu$ PIV - Analysis of Taylor flow in micro channels. *Chemical Engineering Journal* **2008**, *135*, S166-S172.
- [120] Paik, P.; Pamula, V. K.; Fair, R. B., Rapid droplet mixers for digital microfluidic systems. *Lab on a Chip* **2003**, *3* (4), 253-259.
- [121] Ehrfeld, W.; Hessel, V.; Löwe, H., *Microreactors: New Technology for Modern Chemistry*. Wiley-VCH: Weinheim, **2000**.
- [122] Watts, P.; Wiles, C., Recent advances in synthetic micro reaction technology. *Chemical Communications* **2007**, (5), 443-467.
- [123] Shen, J.; Zhao, Y.; Chen, G.; Yuan, Q., Investigation of Nitration Processes of iso-Octanol with Mixed Acid in a Microreactor. *Chinese Journal of Chemical Engineering* **2009**, *17* (3), 412-418.
- [124] Braune, S.; Poehlauer, P.; Reintjens, R.; Steinhofer, S.; Winter, M.; Lobet, O.; Guidat, R.; Woehl, P.; Guerneur, C., Selective nitration in a microreactor for pharmaceutical production under cGMP conditions. *Chimica Oggi-Chemistry Today* **2009**, *27* (1), 26-29.
- [125] Kumar, C. S. S. R., *Microfluidic Devices in Nanotechnology*. Wiley-VCH: New Jersey, **2010**.
- [126] Yen, B. K. H.; Günther, A.; Schmidt, M. A.; Jensen, K. F.; Bawendi, M. G., A Microfabricated Gas-Liquid Segmented Flow Reactor for High-Temperature Synthesis: The Case of CdSe Quantum Dots. *Angewandte Chemie International Edition* **2005**, *44* (34), 5447-5451.

- 
- [127] Bošković, D.; Loebbecke, S.; Gross, G. A.; Koehler, J. M., Residence Time Distribution Studies in Microfluidic Mixing Structures. *Chemical Engineering & Technology* **2011**, *34* (3), 361-370.
- [128] Jensen, K. F., Silicon-based microreactors. In *Microreactor Technology and Process Intensification*, Wang, Y.; Holladay, J. D., Eds. American Chemical Society: **2005**, *914*, 2-22.
- [129] Ehrfeld, W.; Ehrfeld, U. In *Micro Fabrication for Process Intensification*, 5<sup>th</sup> International Conference on Microreaction Technology, Strasbourg, Michael John Matlosz; Wolfgang Ehrfeld; Baselt, J. P., Eds. Springer-Verlag: Strasbourg, **2001**.
- [130] deMello, A. J., Control and detection of chemical reactions in microfluidic systems. *Nature* **2006**, *442* (7101), 394-402.
- [131] Chambers, R. D.; Fox, M. A.; Holling, D.; Nakano, T.; Okazoe, T.; Sandford, G., Elemental fluorine Part 16. Versatile thin-film gas-liquid multi-channel microreactors for effective scale-out. *Lab on a Chip* **2005**, *5* (2), 191-198.
- [132] Serra, C. A.; Chang, Z., Microfluidic-assisted synthesis of polymer particles. *Chemical Engineering & Technology* **2008**, *31* (8), 1099-1115.
- [133] Il Park, J.; Saffari, A.; Kumar, S.; Guenther, A.; Kumacheva, E., Microfluidic Synthesis of Polymer and Inorganic Particulate Materials. In *Annual Review of Materials Research*, Vol 40, Clarke, D. R. R. M. Z. F., Ed. **2010**, *40*, 415-443.
- [134] Marre, S.; Jensen, K. F., Synthesis of micro and nanostructures in microfluidic systems. *Chemical Society Reviews* **2010**, *39* (3), 1183-1202.
- [135] Theberge, A. B.; Courtois, F.; Schaerli, Y.; Fischlechner, M.; Abell, C.; Hollfelder, F.; Huck, W. T. S., Microdroplets in Microfluidics: An Evolving Platform for Discoveries in Chemistry and Biology. *Angewandte Chemie-International Edition* **2010**, *49* (34), 5846-5868.
- [136] Nisisako, T.; Torii, T.; Higuchi, T., Novel microreactors for functional polymer beads. *Chemical Engineering Journal* **2004**, *101* (1-3), 23-29.
- [137] Nie, Z.; Li, W.; Seo, M.; Xu, S.; Kumacheva, E., Janus and ternary particles generated by microfluidic synthesis: Design, synthesis, and self-assembly. *Journal of the American Chemical Society* **2006**, *128* (29), 9408-9412.
- [138] Sugiura, S.; Nakajima, M.; Itou, H.; Seki, M., Synthesis of Polymeric Microspheres with Narrow Size Distributions Employing Microchannel Emulsification. *Macromolecular Rapid Communications* **2001**, *22* (10), 773-778.
- [139] Takeuchi, S.; Garstecki, P.; Weibel, D. B.; Whitesides, G. M., An Axisymmetric Flow-Focusing Microfluidic Device. *Advanced Materials* **2005**, *17* (8), 1067-1072.
-

- [140] Serra, C.; Berton, N.; Bouquey, M.; Prat, L.; Hadziioannou, G., A predictive approach of the influence of the operating parameters on the size of polymer particles synthesized in a simplified microfluidic system. *Langmuir* **2007**, *23* (14), 7745-7750.
- [141] Hayward, R. C.; Utada, A. S.; Dan, N.; Weitz, D. A., Dewetting instability during the formation of polymersomes from block-copolymer-stabilized double emulsions. *Langmuir* **2006**, *22* (10), 4457-4461.
- [142] Hung, L. H.; Lee, A. P., Microfluidic devices for the synthesis of nanoparticles and biomaterials. *Journal of Medical and Biological Engineering* **2007**, *27* (1), 1-6.
- [143] Xu, S. Q.; Nie, Z. H.; Seo, M.; Lewis, P.; Kumacheva, E.; Stone, H. A.; Garstecki, P.; Weibel, D. B.; Gitlin, I.; Whitesides, G. M., Generation of monodisperse particles by using microfluidics: Control over size, shape, and composition. *Angewandte Chemie-International Edition* **2005**, *44* (5), 724-728.
- [144] Kim, S. H.; Jeon, S. J.; Yang, S. M., Optofluidic encapsulation of crystalline colloidal arrays into spherical membrane. *Journal of the American Chemical Society* **2008**, *130* (18), 6040-6046.
- [145] Duraiswamy, S.; Khan, S. A., Droplet-Based Microfluidic Synthesis of Anisotropic Metal Nanocrystals. *Small* **2009**, *5* (24), 2828-2834.
- [146] Knauer, A.; Thete, A.; Li, S.; Romanus, H.; Csaki, A.; Fritzsche, W.; Koehler, J. M., Au/Ag/Au double shell nanoparticles with narrow size distribution obtained by continuous micro segmented flow synthesis. *Chemical Engineering Journal* **2011**, *166* (3), 1164-1169.
- [147] Shestopalov, I.; Tice, J. D.; Ismagilov, R. F., Multi-step synthesis of nanoparticles performed on millisecond time scale in a microfluidic droplet-based system. *Lab on a Chip* **2004**, *4* (4), 316-321.
- [148] Frenz, L.; El Harrak, A.; Pauly, M.; Begin-Colin, S.; Griffiths, A. D.; Baret, J.-C., Droplet-based microreactors for the synthesis of magnetic iron oxide nanoparticles. *Angewandte Chemie-International Edition* **2008**, *47* (36), 6817-6820.
- [149] Kirner, T.; Albert, J.; Gunther, M.; Mayer, G.; Reinhackel, K.; Köhler, J. M., Static micromixers for modular chip reactor arrangements in two-step reactions an photochemical activated processes. *Chemical Engineering Journal* **2004**, *101* (1-3), 65-74.
- [150] Köhler, J. M.; Wagner, J.; Albert, J., Formation of isolated and clustered Au nanoparticles in the presence of polyelectrolyte molecules using a flow-through Si chip reactor. *Journal of Materials Chemistry* **2005**, *15* (19), 1924-1930.
- [151] Wagner, J.; Köhler, J. M., Continuous synthesis of gold nanoparticles in a microreactor. *Nano Letters* **2005**, *5* (4), 685-691.

- 
- [152] Köhler, J. M.; Held, M.; Huebner, U.; Wagner, J., Formation of Au/Ag nanoparticles in a two step micro flow-through process. *Chemical Engineering & Technology* **2007**, *30* (3), 347-354.
- [153] Kimling, J.; Maier, M.; Okenve, B.; Kotaidis, V.; Ballot, H.; Plech, A., Turkevich method for gold nanoparticle synthesis revisited. *Journal of Physical Chemistry B* **2006**, *110* (32), 15700-15707.
- [154] Turkevich, J.; Stevenson, P. C.; Hillier, J., A study of the nucleation and growth processes in the synthesis of colloidal gold. *Discussions of the Faraday Society* **1951**, (11), 55-75.
- [155] Li, P.; Liu, H.; Zhang, Y.-F.; Wei, Y.; Wang, X.-K., Synthesis of flower-like ZnO microstructures via a simple solution route. *Materials Chemistry and Physics* **2007**, *106* (1), 63-69.
- [156] Zhang, W. Q.; Lu, Y.; Zhang, T. K.; Xu, W.; Zhang, M.; Yu, S. H., Controlled Synthesis and Biocompatibility of Water-Soluble ZnO Nanorods/Au Nanocomposites with Tunable UV and Visible Emission Intensity. *The Journal of Physical Chemistry C* **2008**, *112* (50), 19872-19877.
- [157] Gfroerer, T. H., Photoluminescence in Analysis of Surfaces and Interfaces. In *Encyclopedia of Analytical Chemistry*, John Wiley & Sons, Ltd: **2006**, 9209-9231.
- [158] Ray, B.; Mandal, B. M., Dispersion Polymerization of Acrylamide. *Langmuir* **1997**, *13* (8), 2191-2196.
- [159] *CPS disc centrifuge operating manuel*. CPS nstruments, Inc.: Stuart, Florida (USA), **2003**.
- [160] McKenzie, L. C.; Haben, P. M.; Kevan, S. D.; Hutchison, J. E., Determining Nanoparticle Size in Real Time by Small-Angle X-ray Scattering in a Microscale Flow System. *Journal of Physical Chemistry C* **2010**, *114* (50), 22055-22063.
- [161] Wess, T. J.; Drakopoulos, M.; Snigirev, A.; Wouters, J.; Paris, O.; Fratzl, P.; Collins, M.; Hiller, J.; Nielsen, K., The use of small-angle x-ray diffraction studies for the analysis of structural features in archaeological samples. *Archaeometry* **2001**, *43*, 117-129.
- [162] Kelly, S. D.; Hesterberg, D.; Ravel, B., *Analysis of Soils and Minerals Using X-ray Absorption Spectroscopy*. Soil Science Society of America, Inc.: Madison, Wisconsin, **2008**.
- [163] Newville, M., Fundamentals of XAFS. Consortium for Advanced Radiation Sources, University of Chicago: Chicago, Illinois, 2004.
- [164] Agarwal, U. P.; Atalla, R. H., *Raman spectroscopy*. CRC Press: Boca Raton, **1995**; Vol. 8, 152-181.
-

- [165] Zhou, Q.; Zhao, G.; Chao, Y.; Li, Y.; Wu, Y.; Zheng, J., Charge-Transfer Induced Surface-Enhanced Raman Scattering in Silver Nanoparticle Assemblies. *The Journal of Physical Chemistry C* **2007**, *111* (5), 1951-1954.
- [166] Yang, L.; Ruan, W.; Jiang, X.; Zhao, B.; Xu, W.; Lombardi, J. R., Contribution of ZnO to Charge-Transfer Induced Surface-Enhanced Raman Scattering in Au/ZnO/PATP Assembly. *The Journal of Physical Chemistry C* **2009**, *113* (1), 117-120.
- [167] Lombardi, J. R.; Birke, R. L., A Unified Approach to Surface-Enhanced Raman Spectroscopy. *The Journal of Physical Chemistry C* **2008**, *112* (14), 5605-5617.
- [168] Djurisic, A. B.; Leung, Y. H.; Tam, K. H.; Hsu, Y. F.; Ding, L.; Ge, W. K.; Zhong, Y. C.; Wong, K. S.; Chan, W. K.; Tam, H. L.; Cheah, K. W.; Kwok, W. M.; Phillips, D. L., Defect emissions in ZnO nanostructures. *Nanotechnology* **2007**, *18* (9), 095702.
- [169] Polsongkram, D.; Chamninok, P.; Pukird, S.; Chow, L.; Lupan, O.; Chai, G.; Khallaf, H.; Park, S.; Schulte, A., Effect of synthesis conditions on the growth of ZnO nanorods via hydrothermal method. *Physica B* **2008**, *403* (19-20), 3713-3717.
- [170] Cheng, B.; Shi; Russell-Tanner, J. M.; Zhang, L.; Samulski, E. T., Synthesis of Variable-Aspect-Ratio, Single-Crystalline ZnO Nanostructures. *Inorg. Chem.* **2006**, *45* (3), 1208-1214.
- [171] Gao, P. X.; Wang, Z. L., Substrate Atomic-Termination-Induced Anisotropic Growth of ZnO Nanowires/Nanorods by the VLS Process. *J. Phys. Chem. B* **2004**, *108* (23), 7534-7537.
- [172] Wahab, R.; Ansari, S. G.; Kim, Y. S.; Seo, H. K.; Kim, G. S.; Khang, G.; Shin, H.-S., Low temperature solution synthesis and characterization of ZnO nano-flowers. *Mater. Res. Bull.* **2007**, *42* (9), 1640-1648.
- [173] Li, W. J.; Shi, E. W.; Zhong, W. Z.; Yin, Z. W., Growth mechanism and growth habit of oxide crystals. *J. Cryst. Growth* **1999**, *203* (1-2), 186-196.
- [174] Ahsanulhaq, Q.; Kim, S. H.; Kim, J. H.; Hahn, Y. B., Structural properties and growth mechanism of flower-like ZnO structures obtained by simple solution method. *Mater. Res. Bull.* **2008**, *43* (12), 3483-3489.
- [175] Aimable, A.; Buscaglia, M. T.; Buscaglia, V.; Bowen, P., Polymer-assisted precipitation of ZnO nanoparticles with narrow particle size distribution. *J. Eur. Ceram. Soc.* **2010**, *30* (2), 591-598.
- [176] Zhang, J.; Sun, L. D.; Yin, J. L.; Su, H. L.; Liao, C. S.; Yan, C. H., Control of ZnO morphology via a simple solution route. *Chemistry of Materials* **2002**, *14* (10), 4172-4177.
- [177] Xu, L.; Hu, Y. L.; Pelligra, C.; Chen, C. H.; Jin, L.; Huang, H.; Sithambaram, S.; Aindow, M.; Joesten, R.; Suib, S. L., ZnO with Different Morphologies Synthesized by Solvothermal Methods for Enhanced Photocatalytic Activity. *Chemistry of Materials* **2009**, *21* (13), 2875-2885.

- 
- [178] Bouropoulos, N.; Tsiaoussis, I.; Poulopoulos, P.; Reditis, P.; Baskoutas, S., ZnO controllable sized quantum dots produced by polyol method: An experimental and theoretical study. *Materials Letters* **2008**, *62* (20), 3533-3535.
- [179] Tang, X. S.; Choo, E. S. G.; Li, L.; Ding, J.; Xue, J. M., One-Pot Synthesis of Water-Stable ZnO Nanoparticles via a Polyol Hydrolysis Route and Their Cell Labeling Applications. *Langmuir* **2009**, *25* (9), 5271-5275.
- [180] Tice, J. D.; Song, H.; Lyon, A. D.; Ismagilov, R. F., Formation of droplets and mixing in multiphase microfluidics at low values of the Reynolds and the capillary numbers. *Langmuir* **2003**, *19* (22), 9127-9133.
- [181] Jensen, K. F., Microreaction engineering - is small better? *Chemical Engineering Science* **2001**, *56* (2), 293-303.
- [182] Hu, Z.; Escamilla Ramirez, D. J.; Heredia Cervera, B. E.; Oskam, G.; Searson, P. C., Synthesis of ZnO Nanoparticles in 2-Propanol by Reaction with Water. *The Journal of Physical Chemistry B* **2005**, *109* (22), 11209-11214.
- [183] Brus, L., Electronic wave functions in semiconductor clusters: experiment and theory. *The Journal of Physical Chemistry* **1986**, *90* (12), 2555-2560.
- [184] Pesika, N. S.; Stebe, K. J.; Searson, P. C., Relationship between Absorbance Spectra and Particle Size Distributions for Quantum-Sized Nanocrystals. *The Journal of Physical Chemistry B* **2003**, *107* (38), 10412-10415.
- [185] Lee, S.; Jeong, S.; Kim, D.; Hwang, S.; Jeon, M.; Moon, J., ZnO nanoparticles with controlled shapes and sizes prepared using a simple polyol synthesis. *Superlattices and Microstructures* **2008**, *43* (4), 330-339.
- [186] Dakhlaoui, A.; Jendoubi, M.; Smiri, L. S.; Kanaev, A.; Jouini, N., Synthesis, characterization and optical properties of ZnO nanoparticles with controlled size and morphology. *Journal of Crystal Growth* **2009**, *311* (16), 3989-3996.
- [187] Wang, B. G.; Shi, E. W.; Zhong, W. Z., Understanding and controlling the morphology of ZnO crystallites under hydrothermal conditions. *Crystal Research and Technology* **1997**, *32* (5), 659-667.
- [188] Biswas, K.; Das, B.; Rao, C. N. R., Growth kinetics of ZnO nanorods: Capping-dependent mechanism and other interesting features. *Journal of Physical Chemistry C* **2008**, *112* (7), 2404-2411.
- [189] Han, S. W.; Yoo, H. J.; An, S. J.; Yoo, J.; Yi, G. C., Orientation-dependent x-ray absorption fine structure of ZnO nanorods. *Applied Physics Letters* **2005**, *86* (2).
- [190] Han, S.-W., X-ray absorption fine structure and nanostructures. *International Journal of Nanotechnology* **2006**, *3* (2-3), 396-413.
- [191] Tran, N. H.; Hartmann, A. J.; Lamb, R. N., Structural order of nanocrystalline ZnO films. *Journal of Physical Chemistry B* **1999**, *103* (21), 4264-4268.
-

- [192] Wu, Z. H.; Zhou, Y. X.; Zhang, X. Y.; Wei, S. Q.; Chen, D. L., Structure of grain boundaries in nanostructured ZnO. *Applied Physics Letters* **2004**, *84* (22), 4442-4444.
- [193] Vafaei, M.; Ghamsari, M. S., Preparation and characterization of ZnO nanoparticles by a novel sol-gel route. *Materials Letters* **2007**, *61* (14-15), 3265-3268.
- [194] Spanhel, L.; Anderson, M. A., Semiconductor clusters in the sol-gel process: quantized aggregation, gelation, and crystal growth in concentrated zinc oxide colloids. *Journal of the American Chemical Society* **1991**, *113* (8), 2826-2833.
- [195] Zhang, Q.; Vickers, M. E.; Patel, A.; Whatmore, R. W., Determination of particle size and shape during the hydrolysis of Pb(Zr<sub>0.3</sub>Ti<sub>0.7</sub>)O<sub>3</sub> precursor solutions. *Journal of Sol-Gel Science and Technology* **1998**, *11* (2), 141-152.
- [196] Hino, K.; Shingai, R.; Morita, T.; Toku, K.; Hirano, T.; Yoshikawa, H.; Nakano, H.; Nishi, N., Size distribution of gold nanoparticles covered with thiol-terminated cyanobiphenyl-type liquid crystal molecules studied with small-angle X-ray scattering and TEM. *Chemical Physics Letters* **2008**, *460* (1-3), 173-177.
- [197] Hernandez, R.; Sacristan, J.; Nogales, A.; Ezquerro, T. A.; Mijangos, C., Structural Organization of Iron Oxide Nanoparticles Synthesized Inside Hybrid Polymer Gels Derived from Alginate Studied with Small-Angle X-ray Scattering. *Langmuir* **2009**, *25* (22), 13212-13218.
- [198] Aacutebrahaacutem, N.; Deacutekaacuteny, I., Size-dependent photoluminescence properties of bare ZnO and polyethylene imine stabilized ZnO nanoparticles and their Langmuir-Blodgett films. *Colloids and Surfaces A: Physicochemical and Engineering Aspects* **2010**, *364* (1-3), 26-33.
- [199] Abdullah, M.; Morimoto, T.; Okuyama, K., Generating blue and red luminescence from ZnO/poly(ethylene glycol) nanocomposites prepared using an in-situ method. *Advanced Functional Materials* **2003**, *13* (10), 800-804.
- [200] Tang, X.; Choo, E. S. G.; Li, L.; Ding, J.; Xue, J., Synthesis of ZnO Nanoparticles with Tunable Emission Colors and Their Cell Labeling Applications. *Chemistry of Materials* **2010**, *22* (11), 3383-3388.
- [201] Xiong, H. M.; Liu, D. P.; Xia, Y. Y.; Chen, J. S., Polyether-grafted ZnO nanoparticles with tunable and stable photoluminescence at room temperature. *Chemistry of Materials* **2005**, *17* (12), 3062-3064.
- [202] Zhang, L.; Yin, L.; Wang, C.; Lun, N.; Qi, Y.; Xiang, D., Origin of Visible Photoluminescence of ZnO Quantum Dots: Defect-Dependent and Size-Dependent. *Journal of Physical Chemistry C* **2010**, *114* (21), 9651-9658.
- [203] Ankudinov, A. L.; Ravel, B.; Rehr, J. J.; Conradson, S. D., Real-space multiple-scattering calculation and interpretation of x-ray-absorption near-edge structure. *Physical Review B* **1998**, *58* (12), 7565-7576.

- 
- [204] Li, P.; Wei, Z.; Wu, T.; Peng, Q.; Li, Y., Au-ZnO Hybrid Nanopyramids and Their Photocatalytic Properties. *Journal of the American Chemical Society* **2011**, *133* (15), 5660-5663.
- [205] Subramanian, V.; Wolf, E.; Kamat, P. V., Semiconductor-metal composite nanostructures. To what extent do metal nanoparticles improve the photocatalytic activity of TiO<sub>2</sub> films? *Journal of Physical Chemistry B* **2001**, *105* (46), 11439-11446.
- [206] Kamat, P. V., Photoinduced transformations in semiconductor-metal nanocomposite assemblies. *Pure and Applied Chemistry* **2002**, *74* (9), 1693-1706.
- [207] Shaviv, E.; Banin, U., Synergistic Effects on Second Harmonic Generation of Hybrid CdSe–Au Nanoparticles. *ACS Nano* **2010**, *4* (3), 1529-1538.
- [208] Joshi, R. K.; Hu, Q.; Alvi, F.; Joshi, N.; Kumar, A., Au Decorated Zinc Oxide Nanowires for CO Sensing. *The Journal of Physical Chemistry C* **2009**, *113* (36), 16199-16202.
- [209] Im, J.; Singh, J.; Soares, J. W.; Steeves, D. M.; Whitten, J. E., Synthesis and Optical Properties of Dithiol-Linked ZnO/Gold Nanoparticle Composites. *Journal of Physical Chemistry C* **2011**, *115* (21), 10518-10523.
- [210] Yuan, D. W.; Song, S. G.; Yan, R. F.; Ryba, E. R.; Simkovich, G., Formation of ZnO/metal composites by rapid oxidation of Zn melts. *Journal of Materials Science* **1999**, *34* (6), 1293-1300.
- [211] Alammar, T.; Mudring, A. V., Facile preparation of Ag/ZnO nanoparticles via photoreduction. *Journal of Materials Science* **2009**, *44* (12), 3218-3222.
- [212] Michota, A.; Bukowska, J., Surface-enhanced Raman scattering (SERS) of 4-mercaptobenzoic acid on silver and gold substrates. *Journal of Raman Spectroscopy* **2003**, *34* (1), 21-25.
- [213] Yang, L.; Jiang, X.; Ruan, W.; Zhao, B.; Xu, W.; Lombardi, J. R., Adsorption study of 4-MBA on TiO<sub>2</sub> nanoparticles by surface-enhanced Raman spectroscopy. *Journal of Raman Spectroscopy* **2009**, *40* (12), 2004-2008.
- [214] Sisco, P. N.; Murphy, C. J., Surface-Coverage Dependence of Surface-Enhanced Raman Scattering from Gold Nanocubes on Self-Assembled Monolayers of Analyte. *Journal of Physical Chemistry A* **2009**, *113* (16), 3973-3978.
- [215] Lee, S. B.; Kim, K.; Kim, M. S., SURFACE-ENHANCED RAMAN-SCATTERING OF ORTHO-MERCAPTOBENZOIC ACID IN SILVER SOL. *Journal of Raman Spectroscopy* **1991**, *22* (12), 811-817.
- [216] Aee Chun, H.; Wan Boo, D.; Kim, K.; Soo Kim, M., Surface-enhanced Raman scattering of 4-methoxybenzylcyanide in silver sol. *Journal of Molecular Structure* **1990**, *216* (0), 41-52.
-

- [217] Chun, H. A.; Kim, M. S.; Kim, K., Surface-enhanced Raman spectroscopic study of hydrocinnamitrile adsorbed on silver surface. *Journal of Molecular Structure* **1989**, *213* (0), 63-75.
- [218] Joo, S. W.; Han, S. W.; Han, H. S.; Kim, K., Adsorption and stability of phthalic acid on a colloidal silver surface: surface-enhanced Raman scattering study. *Journal of Raman Spectroscopy* **2000**, *31* (3), 145-150.

## 6 Appendix

### 6.1 Abbreviations

CTAB	Cetrimonium Bromide
CV	Coefficient of Variation
DMSO	Dimethyl Sulfoxid
$D_n$	Numer-Average Diameter
$D_w$	Weight-Average Diameter
EDX	Energy-Dispersive X-Ray Spectroscopy
EG	Ethylene Glycol
ETFE	Ethylene Tetrafluoroethylene
EXAFS	Extended X-ray Absorption Fine Structure
PDI	Polydispersity Index
PEEK	Polyether Ether Ketone
PEG	Polyethylene Glycol
PP9	Perfluoromethyldecalin
PTFE	Polytetrafluoroethylene
SAXS	Small Angle X-ray Scattering
SEM	Scanning Electron Microscope
TD	Tetradecane
TEA	Triethanolamine
TEM	Transmission Electron Microscopy
TMAH	Tetramethylammonium Hydroxide
XRD	X-Ray Diffraction
LED	Light Emitting Diode

## 6.2 Synthesis of water core/polymer shell particles by co-axial capillaries microfluidic device

The experiments in this section were carried out in the Laboratory of Polymer Engineering for High Technology (LIPHT) at University of Strasbourg, France. An easy assembling-disassembling co-axial capillaries microfluidic device was built up to produce uniform water core/polymer shell particles. The number and size of cores, the shell thickness and overall droplet diameter can be easily adjusted by changing the flow rates of the middle and inner fluids. The formed particles were characterized by optical microscopy.

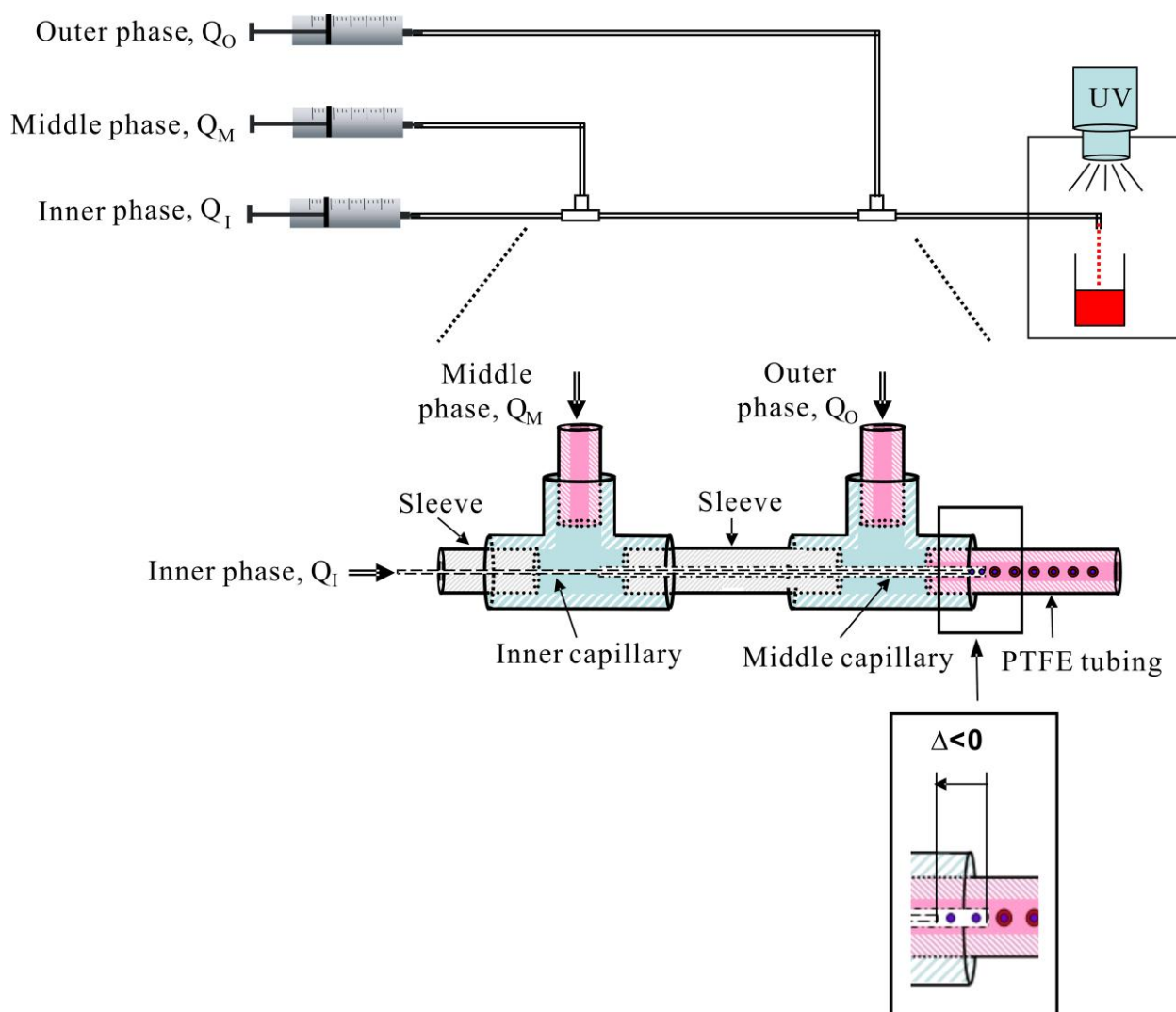


**Fig. 6.1** Schematic illustration of the co-axial capillaries microfluidic device applied for the preparation of water core/polymer shell particles with a negative capillaries' tips relative position ( $\Delta < 0$ ).

## 6.2.1 Experimental methods

### Co-axial capillaries microfluidic device

As reported in previous literature<sup>1</sup>, the device was composed of capillaries with hydrophilic (Fused silica tubing, Polymicro Technologies) or hydrophobic (PEEK or PTFE tubings, Upchurch Scientific) inner walls, T-junctions (P-728-01, Upchurch Scientific), gas-tight syringes, syringe pumps (PHD 2000, Harvard Apparatus), UV light (Lightningcure LC8, Hamamatsu) and tubing (Polytetrafluoroethylene, Fisher Scientific Bioblock).

**Table 6.1** The diameter and materials of the used capillaries and experimental materials.

	Inner diameter	Outer diameter	Materials
Inner capillary <sup>a</sup>	20 $\mu\text{m}$	90 $\mu\text{m}$	Glass
Middle capillary <sup>b</sup>	150 $\mu\text{m}$	360 $\mu\text{m}$	PEEK
Outer capillary	500 $\mu\text{m}$	1600 $\mu\text{m}$	PTFE
Inner fluid phase	H <sub>2</sub> O		
Middle fluid phase	tri(propylene glycol) diacrylate (TPGDA <sup>c</sup> ; 1- hydroxycyclohexyl phenyl ketone (HCPT)		
Outer fluid phase	Aqueous solution of methyl cellulose		
<sup>a</sup> Sleeve used for inner capillary: ID: 70 $\mu\text{m}$ -110 $\mu\text{m}$ ; <sup>b</sup> Sleeve used for middle capillary: ID: 340 $\mu\text{m}$ -380 $\mu\text{m}$ ; <sup>c</sup> Plastic syringe and PTFE tube which contain TPGDA should be packed with Al foil or black adhesive tape to avoid light.			

As shown in Fig. 6.1, two co-axial capillaries were inserted inside a T-junction along its main axis. In order to get a double emulsion, the inner and middle solutions were immiscible fluids as well as the middle and outer phases. Diameters of the different capillaries used are shown in Table 6.1. The inner phase, which ultimately led to the microparticle's core, was delivered

<sup>1</sup> Chang, Z.; Serra, C. A.; Bouquey, M.; Prat, L.; Hadziioannou, G., Co-axial capillaries microfluidic device for synthesizing size- and morphology-controlled polymer core-polymer shell particles. *Lab on a Chip* **2009**, 9 (20), 3007-3011.

via the inner capillary. The middle phase, which composed the microparticle's shell, was delivered through the second inlet of the first T-junction and exited at the tip of the middle capillary. Finally, the continuous phase was injected via the second inlet of the second T-junction. Upon formation of the double droplet, the shell was hardened under UV irradiation (365 nm) directly in the outlet PTFE tubing. Two different systems were tested by varying the flow rate of the middle phase and outer phase.

### Preparation of chemicals

An aqueous solution of 1.5 % methyl cellulose (Alfa Aesar) in distilled water was used as the continuous phase (Outer fluid) with viscosity of 1100 cP. The middle fluid consisted of 96 wt% tri(propylene glycol) diacrylate (TPGDA) (Aldrich) and 4 wt% 1-hydroxycyclohexyl phenyl ketone (HCPT) as photoinitiator (Aldrich). The inner fluid was distilled water.

### Characterization

Direct observation of the droplet formation was realized by coupling a CCD camera (Pike F-032B, Allied Technology) with a Nikon microscope (Eclipse 80i, Nikon). The camera captured up to 200 fps at a full resolution of 648×488 pixels. The overall diameter, core diameter and shell thickness of the formed particles were analyzed using the image analysis module of the software controlling the CCD camera (Hiris, R&D vision). The average diameter of the produced particles was determined by measuring the diameter of at least 50 polymer particles. The viscosity of the continuous phase was measured with a rheometer (Rheo RV8, spindle 6.50 rpm).

### 6.2.2 Results and discussion

In microsystem, the Reynolds number (Re) and the capillary number (Ca) are two dimensionless numbers which have shown significant contribution to the produced particles diameter<sup>2</sup>. They are defined by equation 6.1 and 6.2, respectively.

---

<sup>2</sup> Serra, C. A.; Chang, Z., Microfluidic-assisted synthesis of polymer particles. *Chemical Engineering & Technology* **2008**, *31* (8), 1099-1115.

---

$$\text{Re} = \frac{\rho V D}{\mu} \quad (6.1)$$

$$\text{Ca} = \frac{\mu V}{\gamma} \quad (6.2)$$

where  $\rho$  and  $\mu$  are the fluids density and viscosity, respectively,  $V$  is the mean fluids velocity,  $D$  is the characteristic dimension of the flow (usually the channel width), and  $\gamma$  is the interfacial tension between the two immiscible fluids.

Generally speaking, an increase in the flow rate of the continuous phase or a decrease in the dispersed phase flow rate can induce a decrease in the produced particles diameter. It is also known that higher viscosity of the continuous phase or lower viscosity of dispersed phase can also reduce the size of the generated particles. In addition, the particle diameter is also influenced by the interfacial tension and the characteristic dimension of the microsystem. However, in this study, we only investigate the effect of the flow rates of the middle and outer fluids while keeping other parameters constant.

It is known that the droplet formation from two continuous co-flowing liquids is based on two mechanisms: dripping or jetting<sup>3, 4, 5</sup>. In the dripping mode, drops are formed close to the capillary tube, while in the jetting mode, a jet extends downstream from the orifice and drop detachment takes place at the end of the long threads. Droplets produced by dripping are characterized by periodic formation of highly monodisperse droplets and prevails at low flow rates. In comparison, the jetting regime is normally quite irregular, resulting in polydisperse droplets. In this experiment, since we worked at high viscosity ratio of continuous phase to dispersed phase, as well as a relatively low velocity of all fluids, the droplets were formed in the

---

<sup>3</sup> Utada, A. S.; Lorenceau, E.; Link, D. R.; Kaplan, P. D.; Stone, H. A.; Weitz, D. A., Monodisperse double emulsions generated from a microcapillary device. *Science* **2005**, *308* (5721), 537-541.

<sup>4</sup> Cui, Y.; Gupta, N. R., Surfactant effects on drop formation in co-flowing fluid streams. *Colloids and Surfaces A: Physicochemical and Engineering Aspects* **2012**, *393* (0), 111-121.

<sup>5</sup> Cramer, C.; Fischer, P.; Windhab, E. J., Drop formation in a co-flowing ambient fluid. *Chemical Engineering Science* **2004**, *59* (15), 3045-3058.

dripping mode which ensured the formation of highly homogeneous double droplets<sup>6</sup>.

---

<sup>6</sup> Serra, C.; Berton, N.; Bouquey, M.; Prat, L.; Hadziioannou, G., A predictive approach of the influence of the operating parameters on the size of polymer particles synthesized in a simplified microfluidic system. *Langmuir* **2007**, *23* (14), 7745-7750.

**Preparation of water core/poly(TPGDA) shell particles produced under constant flow rates of middle fluid (0.004 mL/min) and inner fluid (0.001 mL/min)**

In our previous work<sup>1</sup>, it has been found that if the inner capillary tip was moved upstream relatively to the middle capillary tip shown in Fig. 5.1, droplets with smaller and multiple cores were produced. Here, the middle and inner fluids were kept constant as 0.004 mL/min and 0.001 mL/min, respectively. The flow rate of outer fluid was adjusted from 0.01 mL/min to 0.09 mL/min to investigate the changes of the number of cores and particle diameter.

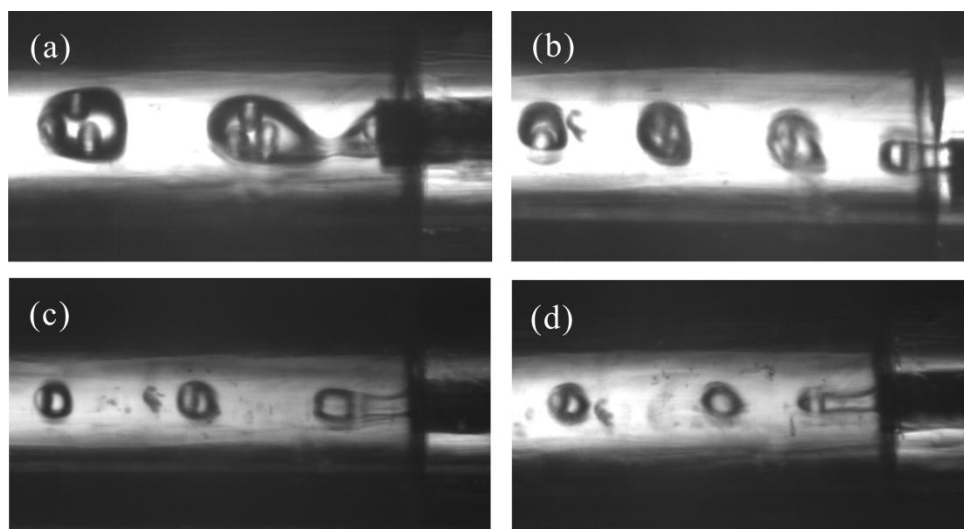


**Fig. 6.2** Snapshots of the formation of the water core/poly(TPGDA) shell droplets at the exit of the two co-axial capillaries produced under constant flow rates of middle fluid (0.004 mL/min) and inner fluid (0.001 mL/min). The flow rate of outer fluid was varied: (a)  $Q_o = 0.01$  mL/min; (b)  $Q_o = 0.03$  mL/min; (c)  $Q_o = 0.06$  mL/min; (d)  $Q_o = 0.07$  mL/min.

As shown in Fig. 6.2, if the flow rate of outer continuous phase was 0.10 mL/min, droplets with three small cores were formed, which would fuse with each other and finally became core/shell droplets with only one core. If the outer flow rate was increased to 0.30 mL/min, droplets with one or two cores were produced. Optical microscopes image (Fig. 6.3a) indicated that at this condition, the size distribution of formed particles was not homogeneous since they had different number of cores. However, homogeneous core/shell droplets can be obtained if the outer fluid flow rate was varied from 0.04 mL/min to 0.06 mL/min shown in Fig. 6.3b, c. Further increase of the outer flow rate higher than 0.06 mL/min generated some single droplets without core inside. Single droplets have been marked by the squares in Fig. 6.3d. When the shearing force

from the continuous phase is too strong, it would extrude the middle fluid heavily while the core droplet cannot be cut off by middle fluid at the same time, which causes the single droplets. Therefore, the optimal flow rates of middle and outer fluid are very important to obtain homogeneous core/shell droplets in this work. Please note that some small droplets which had a diameter far below the double droplets were found in Fig. 6.2c, d. This phenomenon is caused by the so-called “tipstreaming”<sup>7</sup>, where a fine jet is formed from the tip of the droplet, which eventually breaks into tiny droplets before the formation of the main droplet. It can be observed when large outer flow rate is applied coupled with small inner flow rate<sup>8</sup>.

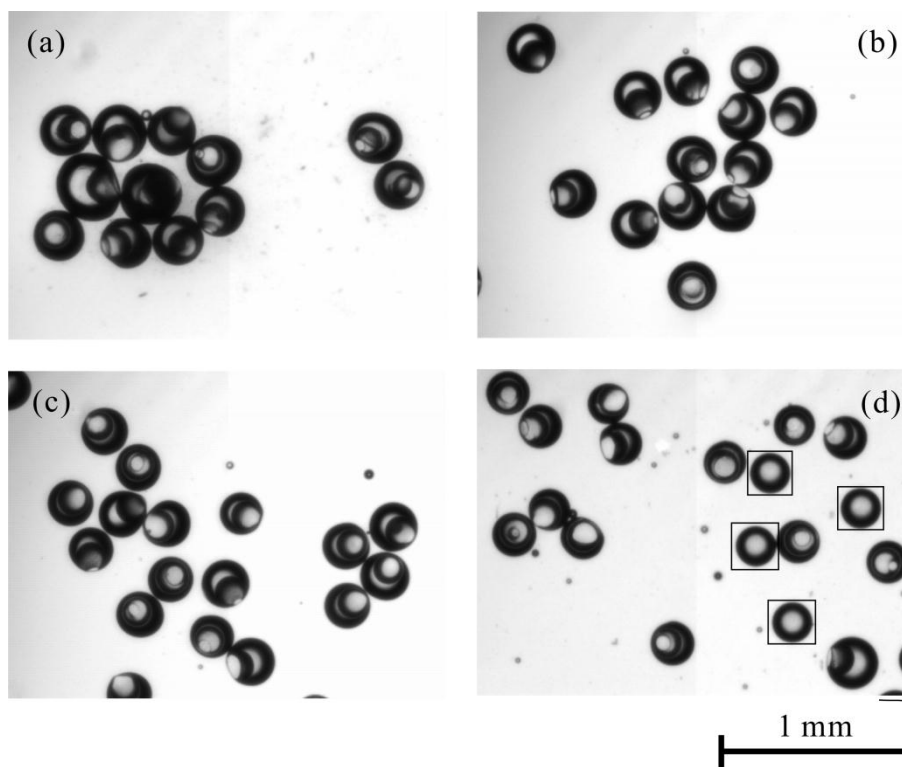


**Fig. 6.3** Optical microscope images of water core/Poly(TPGDA) shell particles with different sizes. The flow rates of middle and inner fluids were kept constant as 0.004 mL/min and 0.001 mL/min, respectively. The flow rate of outer fluid was varied: (a)  $Q_o = 0.03$  mL/min; (b)  $Q_o = 0.05$  mL/min; (c)  $Q_o = 0.06$  mL/min; (d)  $Q_o = 0.07$  mL/min.

In addition, the flow rate of continuous phase also plays an important role on the diameter of the

<sup>7</sup> Suryo, R.; Basaran, O. A., Tip streaming from a liquid drop forming from a tube in a co-flowing outer fluid. *Physics of Fluids* **2006**, *18* (8), 082102.

<sup>8</sup> Zhou, C.; Yue, P.; Feng, J. J., Formation of simple and compound drops in microfluidic devices. *Physics of Fluids* **2006**, *18* (9), 092105.

produced droplets. As shown in Fig. 6.4, when the outer fluid's flow rate was increased from 0.02 mL/min to 0.09 mL/min, the overall droplet diameter was decreased from 297  $\mu\text{m}$  to 216  $\mu\text{m}$  with the core droplet diameter reducing from 197  $\mu\text{m}$  to 165  $\mu\text{m}$ . The shell thickness of the droplets was also slightly decreased from 50  $\mu\text{m}$  to 25  $\mu\text{m}$ . In order to produce the double droplets with wider size range, the second group of experiments was carried out.

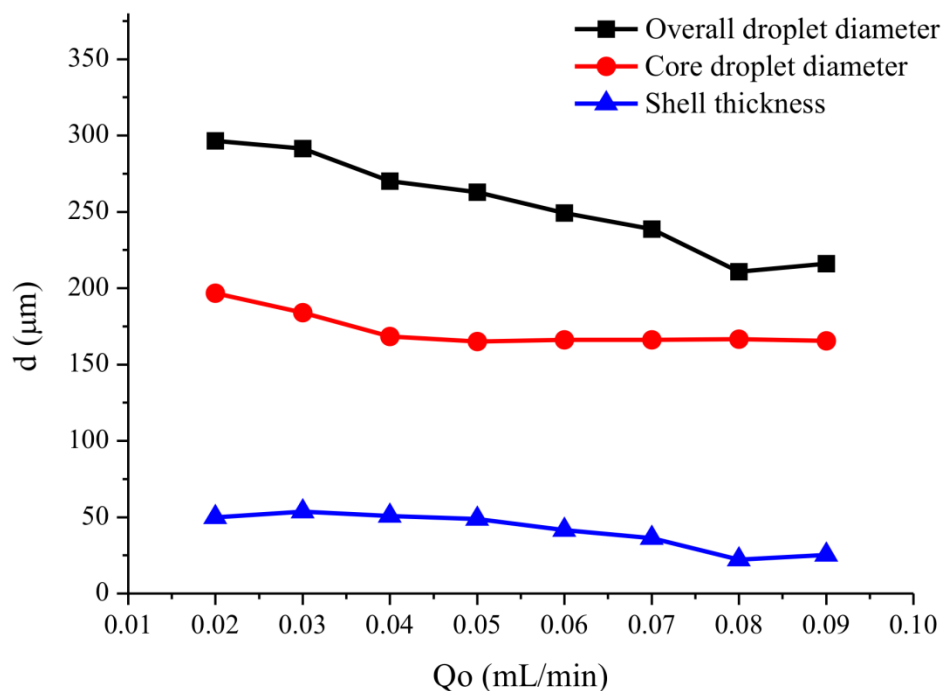


**Fig. 6.4** The influence of outer fluid's flow rate on the core and overall droplet diameter as well as the shell thickness of the water core/poly(TPGDA) shell droplets. The flow rates of middle and inner fluids were kept constant as 0.004 mL/min and 0.001 mL/min, respectively.

#### **Preparation of water core/poly(TPGDA) shell particles produced under constant flow rates of middle fluid (0.0025 ml/min) and inner fluid (0.001 ml/min)**

Here, the flow rate of middle fluid was reduced from 0.004 mL/min to 0.0025 mL/min and inner fluid flow rates were kept the same as 0.001 mL/min. The outer fluid's flow rate was adjusted from 0.02 mL/min to 0.10 mL/min to investigate the size change of the formed droplets. As expected, droplets with one to four cores were successfully generated by adjusting outer fluid's flow rate from 0.01 mL/min to 0.10 mL/min (Fig. 6.5).

However, if the outer fluid flow rate was below than 0.04 mL/min, the fuse of the several small cores resulted in one big core, which can easily escape from the shell and produce some single droplets without core inside. The single droplets are shown in Fig. 6.6a with marked squares. If the outer flow rate was more than 0.06 mL/min, homogeneous droplets with one core inside were generated shown in Fig. 6.6b-d.

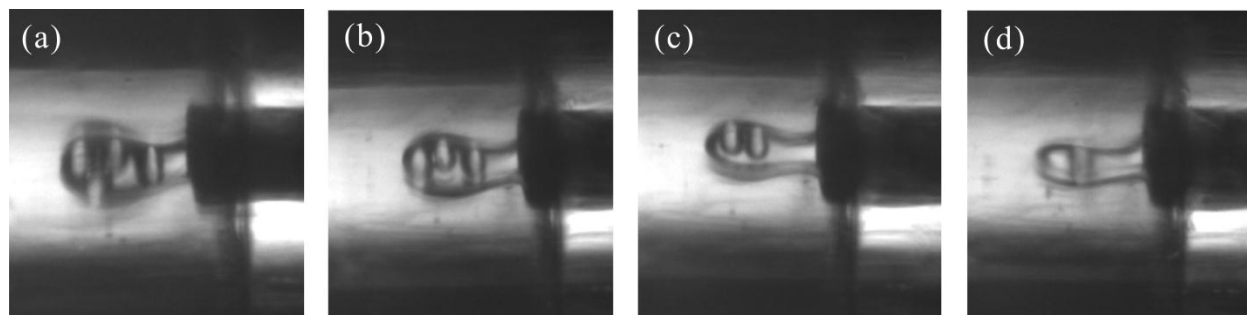


**Fig. 6.5** Snapshots of the formation of the double droplets at the exit of the two co-axial capillaries produced under constant middle and inner fluid flow rates ( $Q_m = 0.0025$  mL/min,  $Q_i = 0.001$  mL/min). The flow rate of outer fluid was varied: (a)  $Q_o = 0.01$  mL/min; (b)  $Q_o = 0.02$  mL/min; (c)  $Q_o = 0.03$  mL/min; (d)  $Q_o = 0.06$  mL/min.

For co-axial capillaries microfluidic device, the sizes of the overall droplets, core diameter and shell thickness are strongly affected by the flow rates of outer, middle and inner fluids. As shown in Fig. 6.6, the overall droplet diameter was decreased dramatically from 320  $\mu\text{m}$  to 192  $\mu\text{m}$  when the outer fluid's flow rate was increased from 0.02 mL/min to 0.07 mL/min. The size of core droplet also reduced from 219  $\mu\text{m}$  to 139  $\mu\text{m}$  at the same flow rate range of outer fluid. However, this decrease rate became slower when the outer fluid flow rate was higher than 0.07 mL/min. The shell thickness had the similar downward trend. In contrast, the shell thickness had relatively weak decreasing rate and it went down from 51  $\mu\text{m}$  to 23  $\mu\text{m}$  with increasing outer flow rate from 0.02 mL/min to 0.10 mL/min. As described previously, in this device, the inner capillary tip had been moved upstream relatively to the middle capillary tip, which meant that the core was generated inside the middle capillary first and then grew up and flowed out of the middle capillary to form double droplets. Note that the inner diameter of middle capillary was 150  $\mu\text{m}$  and the minimum core diameter was 139  $\mu\text{m}$ . It indicates that it is very difficult to continue to decrease the double droplet diameter by simply increasing the flow rate of outer fluid's flow rate, except that smaller middle capillary is chosen due to the limited shearing force for the cores from the middle fluid.

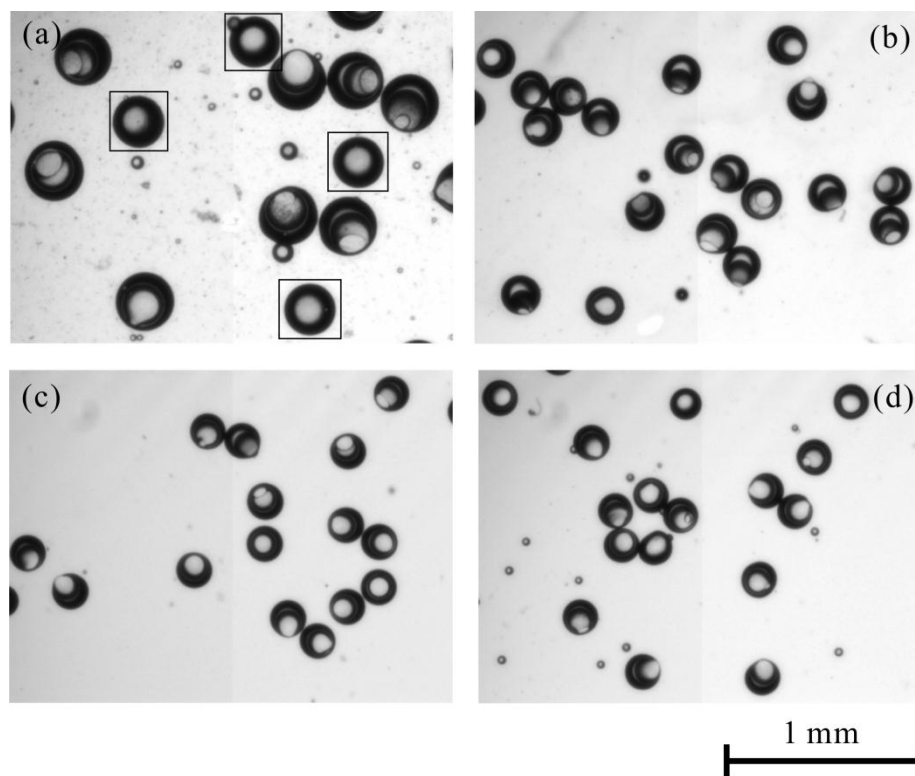


**Fig. 6.6** Optical microscope images of the formed water core/TPGDA shell particles produced under constant middle and inner fluid flow rates ( $Q_m = 0.0025$  mL/min,  $Q_i = 0.001$  mL/min). The flow rate of outer fluid was varied: (a)  $Q_o = 0.02$  mL/min; (b)  $Q_o = 0.06$  mL/min; (c)  $Q_o = 0.07$  mL/min; (d)  $Q_o = 0.10$  mL/min.

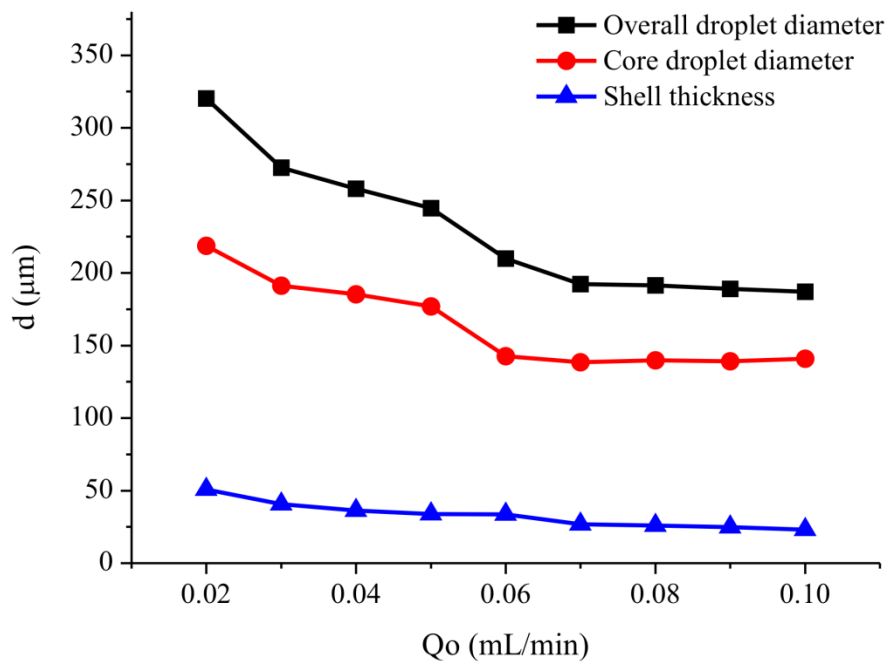


**Fig. 6.7** The influence of outer fluid's flow rate on the core and overall droplet size as well as on the shell thickness of the water core/poly(TPGDA) shell droplets under constant middle and inner fluid flow rates ( $Q_m = 0.0025$  mL/min,  $Q_i = 0.001$  mL/min)..

In a short summary, a two co-axial capillaries microfluidic device was designed for production of uniform double droplets, which were then photopolymerized downstream to produce water core/polymer shell particles. The overall droplet diameter, core number and diameter as well as shell thickness were strongly dependent on the flow rates of the middle and outer fluids. The overall droplet size can be controlled from 320  $\mu\text{m}$  to 187  $\mu\text{m}$  with increasing outer flow rate from 0.02 mL/min to 0.10 mL/min.

### 6.3 Generation of monodisperse slugs by a flow-focusing millifluidic chip

These experiments were carried out at the Center of Advanced Microstructures and Devices (CAMD), Louisiana State University, USA. The generation of uniform slugs was realized in a flow-focusing millifluidic device. The effect of flow rate and carrier fluid on the slug shape and size was investigated.

#### 6.3.1 Experimental methods

##### Experimental arrangement and devices

The experimental set-up for slug formation is shown in Fig. 2. In detail, the PMMA flow focusing chip was mounted on a microfluidic device manifold (Model: 6 way manifold, MicroPlumbers microsciences LLC). Silicon oil or tetradecane were used as continuous phase and flowed into the two outside channels, while aqueous solutions of 0.1 mM rhodamine B and 0.1 mM methylene blue were used as dispersed phase and flowed into the two middle channels. The flow rate of each channel was controlled by high precision syringe pumps (NEMESYS, Cetoni) or pressure pumps (Mitos P-pumps, Dolomite). The generated slugs were recorded by use of a handheld digital camera (Model: 44302, Celestron). The camera can take pictures with frequency of 30 frames each second. When setting a new flow rate, the system was run for at least 2 minutes to reach steady state before images were taken. The slug sizes were averaged by more than 20 observed stable slugs.

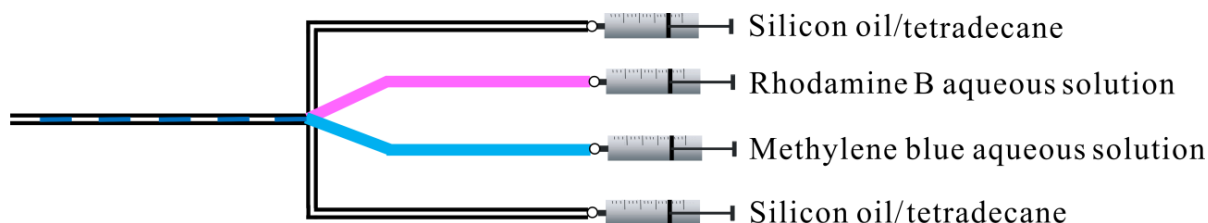
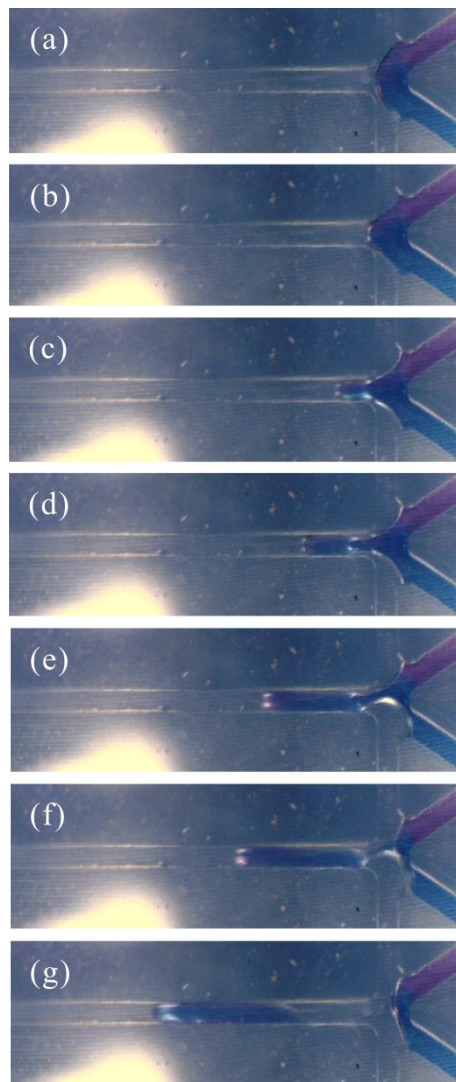


Fig. 6.8 Schematic illustration of the flow-focusing millifluidic chip for slug formation.

#### Chemicals

Methylene blue, rhodamine B, tetradecane (purity: 99.0 %) and silicon oil (viscosity: 10 cSt) were purchased from Sigma Aldrich and used as received. Deionized water (Nanopure infinity ultrapure water system, Barnstead) was used for the preparation of all solutions.

### 6.3.2 Results and discussion



**Fig. 6.9** Experimental images of the slug formation process in the PMMA based microfluidic reactor. The continuous phase was silicon oil with flow rate of 100  $\mu\text{L}/\text{min}$ , while the dispersed phases were aqueous solutions of rhodamine B and methylene blue with flow rate of 10  $\mu\text{L}/\text{min}$ .

The slug formation process in the fabricated microfluidic chip can be described to proceed through five different stages: (1) The two streams of dispersed phase (aqueous solution) merge together; meanwhile, the dispersed phase grow and effectively block the focusing region (Fig. 6.9a, b). During this stage, the dispersed phase expands with a parabolic shape before it reaches the edge of the straight channel. (2) As the continuous phase flows inside the gap between the tip of the dispersed phase and the channel wall to maintain the flow rate, a high pressure drop is

built from each inlet to the interface of two phases (Fig. 6.9c). (3) Due to the shear force and the pressure exerted by continuous phase, the continuous phase drives the thread in its axial direction, and a visible neck forms while the dispersed phase is squeezed into the straight channel (Fig. 6.9d, e). (4) The neck of the dispersed phase breaks asymmetrically adjacent to the channel wall in the junction region (Fig. 6.9f). (5) Finally, a slug is pinched off from the dispersed phase and pushed into the straight channel (Fig. 6.9g).

### **Effect of flow rate ratio on plug size**

In order to study the effect of flow rate ratio of oil phase/water phase on the droplet size, two different oil phases were applied. The first oil phase used here was silicon oil. Camera images of formed plugs are shown in Fig. 6.10a, b. We can observe that smaller plug sizes were generated when enhancing the flow rate ratio of silicon oil/water phase. When the flow rate of silicon oil was 100  $\mu\text{L}/\text{min}$ , the slug size was decreased from 5.0 mm to 3.3 mm when the flow rate ratio was enhanced from 4 to 20 (Fig. 6.10d). In comparison, when the flow rate of silicon oil was 50  $\mu\text{L}/\text{min}$ , the plug size can be adjusted from 7.0 mm to 4.8 mm with increasing flow rate ratio from 1 to 5.

The same effect was also observed when tetradecane was used as continuous phase shown in Fig. 5.10c. The plug size was dramatically reduced from 9.1 mm to 3.9 mm if the flow rate ratio was increased from 1 to 2.86. Please note that keeping increasing the flow rate ratio of oil phase/water phase will lead to unstable plug flow due to an insufficient water flow supply. In addition, no spherical droplets were generated in this chip. The microchannel geometry might be the main factor.

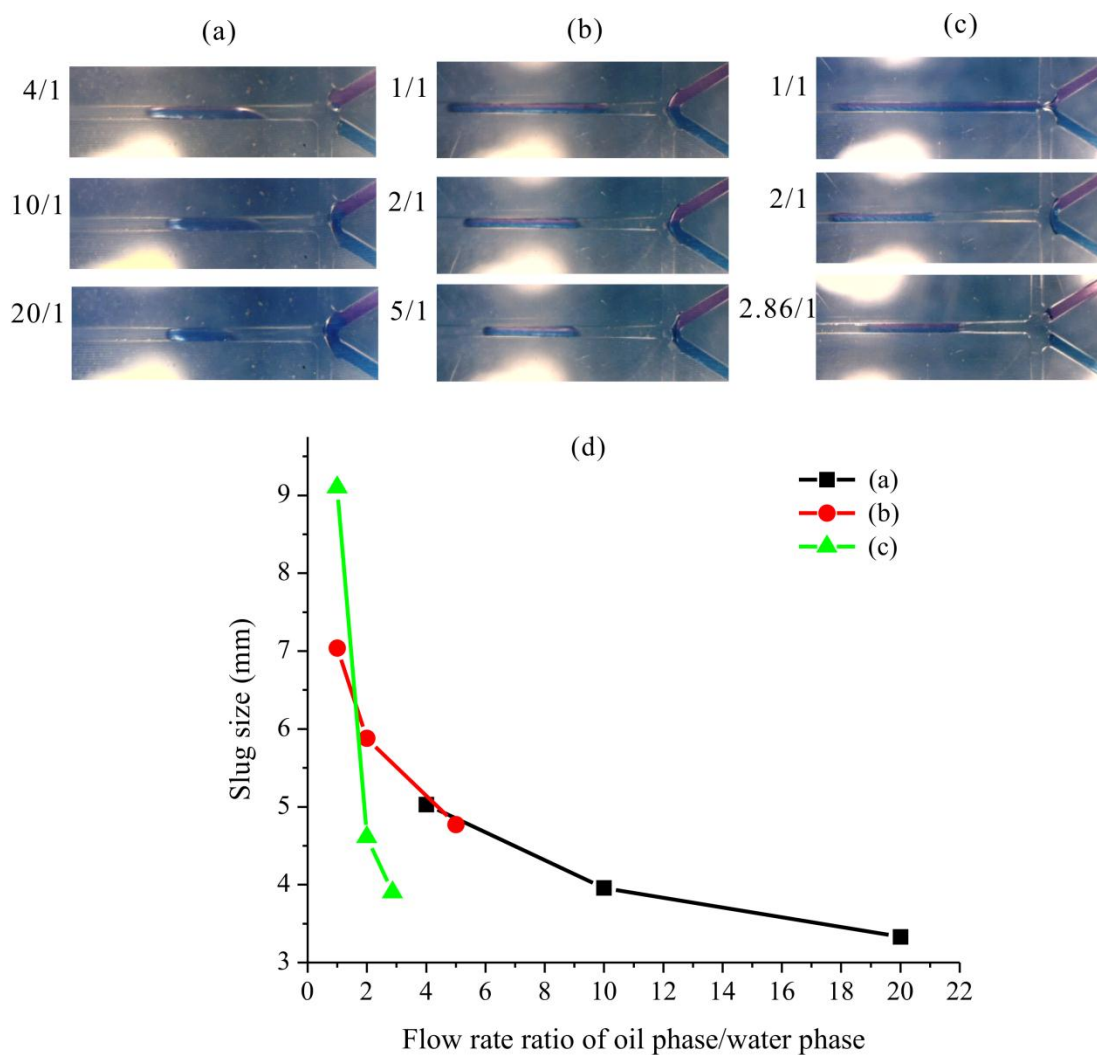


**Fig. 6.10** Camera images of the slugs formed under different flow rate ratio of oil phase/water phase. (a) Continuous phase: silicon oil with constant flow rate of 100  $\mu\text{L}/\text{min}$ ; (b) Continuous phase: silicon oil with constant flow rate of 50  $\mu\text{L}/\text{min}$ ; (c) Continuous phase: tetradecane with constant pressure of 200 mbar; (d) The dependence of the slug size on the flow rate ratio of oil phase/water phase under condition (a, b, c).

#### 6.4 Preparation of Co-doped ZnO nanoparticles by micro segmented flow synthesis

All the experiments in this section were carried out in set-up IV shown in section 2.1. Detailed experimental parameters are presented in Table 6.2. For synthesis of Co-doped ZnO nanoparticles, 0.01 M  $\text{CoCl}_2$  was mixed with 0.09 M  $\text{Zn}(\text{Ac})_2$  in EG and used as precursor. SEM images of undoped and doped ZnO nanoparticles are shown in Fig. 6.11a, b, respectively. The average particle diameter was around 10 nm. No apparent structural changes were observed after doping Co in ZnO nanoparticles. EXD spectra of Co-doped ZnO nanoparticles (Fig. 6.12) have confirmed the presence of Co in the formed particles. It has determined that the weight percent of Co was 7.83 %. The UV/Vis absorption spectra of undoped and doped ZnO nanoparticles are shown in Fig. 6. 13. We can observe the excitonic band of ZnO nanoparticles was around 328 nm. The absorption spectrum of the concentrated Co-doped ZnO nanoparticles revealed three transitions at 562 nm, 604 nm and 644 nm. These can be assigned to cobalt related  ${}^4\text{A}_2(\text{F}) \rightarrow {}^2\text{A}_1(\text{G})$ ,  ${}^4\text{A}_2(\text{F}) \rightarrow {}^4\text{T}_1(\text{P})$ , and  ${}^4\text{A}_2(\text{F}) \rightarrow {}^2\text{E}(\text{G})$  ligand field transitions for tetrahedral symmetry of transition metal ions<sup>9, 10</sup>, which confirmed the presence of high spin  $\text{Co}^{2+}(\text{d}^7)$  state in ZnO lattice.

**Table 6.2** Experimental conditions for synthesis of ZnO nanoparticles.

Reactant	$\text{Zn}(\text{Ac})_2/\text{EG}^a$ 0.1 M	$\text{NaOH}/\text{EG}$ 0.2 M	$\text{H}_2\text{O}$	$\text{TD}^b$	T
Flow rate	850 $\mu\text{L}/\text{min}$	850 $\mu\text{L}/\text{min}$	300 $\mu\text{L}/\text{min}$	3000 $\mu\text{L}/\text{min}$	150 °C
<sup>a</sup> EG: ethylene glycol					
<sup>b</sup> TD: tetradecane					

<sup>9</sup>Inamdar, D. Y.; Lad, A. D.; Pathak, A. K.; Dubenko, I.; Ali, N.; Mahamuni, S., Ferromagnetism in ZnO Nanocrystals: Doping and Surface Chemistry. *The Journal of Physical Chemistry C* **2010**, *114* (3), 1451-1459.

<sup>10</sup>Singhal, A.; Achary, S. N.; Manjanna, J.; Chatterjee, S.; Ayyub, P.; Tyagi, A. K., Chemical Synthesis and Structural and Magnetic Properties of Dispersible Cobalt- and Nickel-Doped ZnO Nanocrystals. *The Journal of Physical Chemistry C* **2010**, *114* (8), 3422-3430.

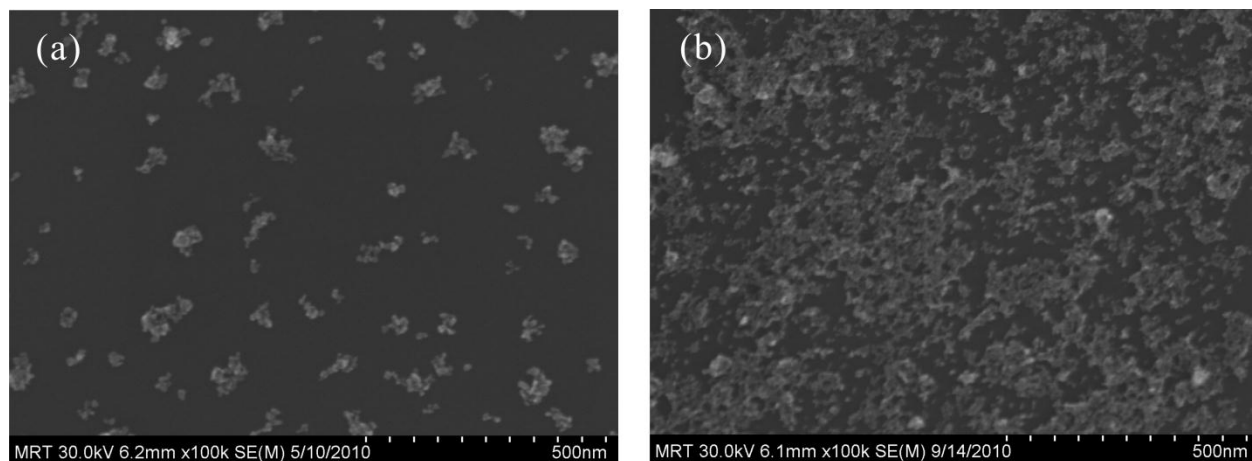


Fig. 6.11 SEM images of (a) ZnO particles and (b) Co-doped ZnO particles.

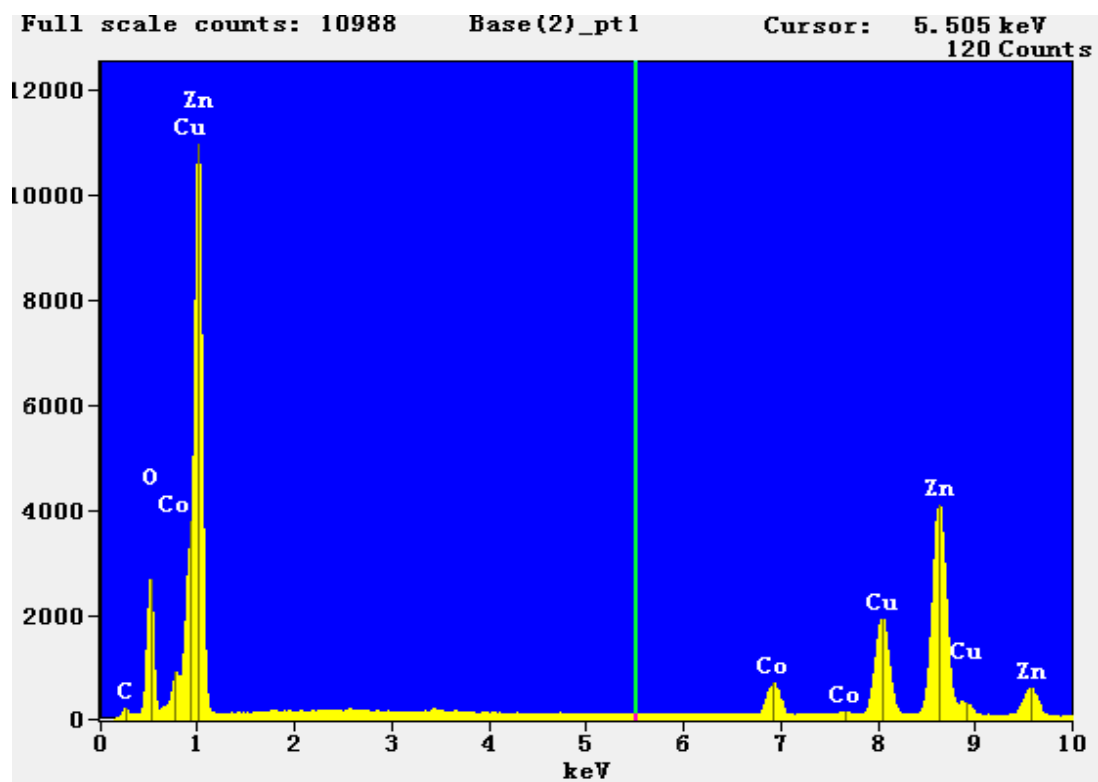
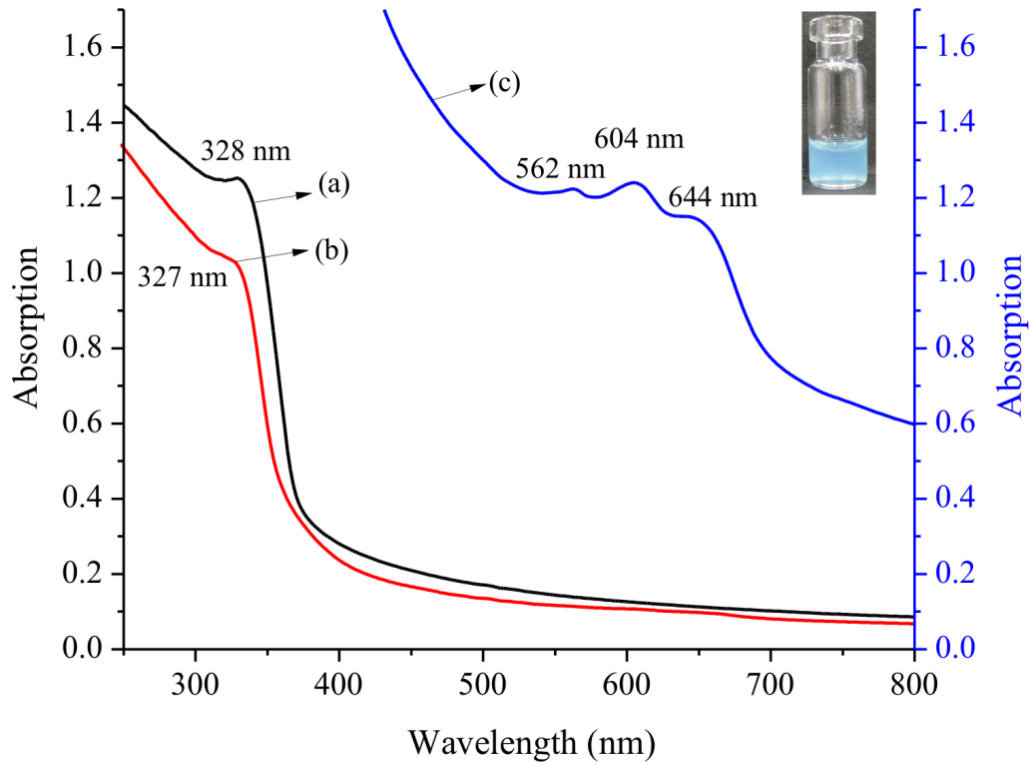


Fig. 6.12 EDX spectra of Co-doped ZnO nanoparticles.



**Fig. 6.13** UV/Vis absorption spectra of (a) ZnO nanoparticles, (b) Co-doped ZnO nanoparticles with diluted concentration and (c) high concentrated Co-doped ZnO nanoparticles. The insert graph shows the picture of Co-doped ZnO nanoparticles solution.

## 6.5 Batch synthesis of Ag and Au nanoparticles

### Ag nanoparticles

Ag nanoparticles solution was prepared by adding 3.5 mg  $\text{NaBH}_4$  to 75 mL cold distilled water (4 °C). Then  $\text{AgNO}_3$  aqueous solution (7.5 mL 2.2 mM) precooled to 4 °C was added dropwise to  $\text{NaBH}_4$  solution with constant stirring. The mixture was stirred in ice-water bath for 45 min. The resulting Ag nanoparticle solution exhibited bright yellow color with UV/Vis absorption peak at 396 nm. Differential centrifugal sedimentation (CPS) analysis showed that the diameter of the Ag nanoparticles was 5.0 nm.

### Au nanoparticles<sup>11</sup>

Sodium borohydride method: Au nanoparticles were prepared by mixing  $\text{HAuCl}_4$  (375  $\mu\text{L}$  4% w/v) and  $\text{K}_2\text{CO}_3$  (500  $\mu\text{L}$  0.2 M) in 100 mL distilled water. Then  $\text{NaBH}_4$  (1 mL 13 mM) was added five times with stirring. The formed Au nanoparticle solution had dark red color with an UV/Vis absorption peak at 515 nm. CPS measurement determined that the size of the Au nanoparticles was 5.0 nm.

Citrate method: After boiling  $\text{HAuCl}_4$  solution (50 mL 0.01% w/v), trisodium citrate solution (0.5 mL 1% w/v) was quickly added with vigorous stirring. The boiling was continued for 3 min. Then the solution was kept stirring without heating until it cooled to room temperature and showed dark red color. The UV/Vis spectrum of the Au nanoparticles showed an absorption peak at 532 nm. The average diameter of the Au nanoparticle was about 50 nm as characterized by DCS.

---

<sup>11</sup> Protocols from Andrea Knauer, Department of Physical Chemistry/Microreaction Technology, TU Ilmenau.

---

## 6.6 Scientific publications

### Journal publications

#### 2012

Y. Li, D. G. Yamane, **S. Li**, R. Reddy, J. S. Goettert, K. Nandakumar, C. S. S. R. Kumar, “Geometric Optimization of Liquid-Liquid Slug Flow in Flow-Focusing Millifluidic Devices”, 2012, submitted

**S. Li**, A. Knauer, K. Risch, U. Ritter, J. M. Köhler, “Synthesis and Characterization of ZnO/4-Mercaptobenzoic Acid/Au Composite Particles”, *Materials Letters*, 2012, revised

**S. Li**, A. Roy, H. Lichtenberg, G. Merchan, C. S. S. R. Kumar, J.M. Köhler, “Local Structure of ZnO Micro Flowers and Nanoparticles Obtained by Micro Segmented Flow Synthesis”, *ChemPhysChem*, 2012, 13, 1557-1561

#### 2011

**S. Li**, G. A. Groß, P. M. Günther, J. M. Köhler, “Hydrothermal Micro Continuous-Flow Synthesis of Spherical, Cylinder-, Star- and Flower-like ZnO Microparticles”, *Chemical Engineering Journal*, 2011, 167, 681-687

A. Knauer, A. Thete, **S. Li**, H. Romanus, A. Csáki, W. Fritzsche, J. M. Köhler, “Au/Ag/Au Double Shell Nanoparticles with Narrow Size Distribution Obtained by Continuous Micro Segmented Flow Synthesis”, *Chemical Engineering Journal*, 2011, 166, 1164-1169

#### 2010

**S. Li**, S. Meierott, J. M. Köhler, “Effect of Water Content on Growth and Optical Properties of ZnO Nanoparticles Generated in Binary Solvent Mixtures by Micro Continuous Flow Synthesis”, *Chemical Engineering Journal*, 2010, 165, 958-965

Z. Chang, C. A. Serra, M. Bouquey, I. Kraus, **S. Li**, J. M. Köhler, “Multiscale Materials from Microcontinuous-Flow Synthesis: ZnO and Au Nanoparticle-Filled Uniform and Homogeneous Polymer Microbeads”, *Nanotechnology*, 2010, 21, 015605

**2009**

S. Li, P. M. Günther, J. M. Köhler, “Micro Segmented-Flow Technique for Continuous Synthesis of Different Kinds of ZnO Nanoparticles in Aqueous and in DMSO Solution”, *Journal of Chemical Engineering of Japan*, 2009, 42, 338-345

**2007**

S. Li, X. Yang, W. Huang, “Preparation of Polymer Microspheres with Pyridyl Group and Their Stabilized Gold Metallic Colloids”, *Chinese Journal of Polymer Science*, 2007, 25, 555 – 563

**2006**

R. Li, X. Yang, G. Li, S. Li, W. Huang, “Core-Corona Polymer Composite Particles by Self-Assembled Heterocoagulation Based on a Hydrogen-Bonding Interaction”, *Langmuir*, 2006, 22, 8127 – 8133

B. Feng, R. Li, X. Yang, S. Li, W. Huang, “Preparation of Narrow-disperse or Monodisperse Polymer Microspheres with Active Hydroxyl Group by Distillation-Precipitation Polymerization”, *Polymer International*, 2006, 55, 319 – 325

**2005**

S. Li, X. Yang, W. Huang, “Synthesis of Monodisperse Polymer Microspheres with Mercapto Groups and Their Application as a Stabilizer for Gold Metallic Colloid”, *Macromolecular Chemistry and Physics*, 2005, 206, 1967 – 1972

**Posters**

**2012**

S. Li, A. Knauer, K. Risch, U. Ritter, J. M. Köhler, “Synthesis and Nanoparticle-Enhanced Raman Scattering (NPERS) of ZnO/4-MBA/Au Composite Particles”, 6th Workshop "Chemical and Biological Micro Laboratory Technology", Elgersburg, March, 2012

**2010**

**S. Li**, J. M. Köhler, "Preparation of ZnO Fluorescent Nanoparticles by Micro Segmented Flow Synthesis", 6th Conference of AK BioMST, Sankt Augustin, Nov. 2010

**S. Li**, G. A. Groß, P. M. Günther, J. M. Köhler, "Hydrothermal Micro Continuous-Flow Synthesis of Spherical, Cylinder-, Star- and Flower-like ZnO Micro and Nanoparticles", 11th International Conference on Microreaction Technology, Kyoto, Japan, March, 2010

**S. Li**, P. M. Günther, J. M. Köhler, "Solvent-Induced Grow of ZnO Micro and Nanoparticles Obtained by Micro Continuous Flow Synthesis", 5th Workshop "Chemical and Biological Micro Laboratory Technology", Elgersburg, Feb. 2010

### **2009**

**S. Li**, P. M. Günther, J. M. Köhler, "Micro Segmented-Flow Technique for Continuous Synthesis of Fluorescent ZnO Micro- and Nanoparticles", MST Kongress 2009, Berlin, Oct. 2009

**S. Li**, P. M. Günther, J. M. Köhler, "Monodisperse ZnO Micro and Nanoparticles with Different Shape and Size Obtained by Continuous Flow Synthesis", SCI Nanoparticles 2009, Liverpool, Sept. 2009

## 6.7 Curriculum vitae

### Personal Information

Name: Shuning Li  
Birth date: Dec.13.1980  
Nationality: Chinese  
Email: shuning.li@tu-ilmenau.de



### Education Background & Work Experience

05/2008-now      **PhD studies** at TU-Ilmenau, Department of Physical Chemistry and Microreaction Technology

Thesis: Monodisperse ZnO Micro and Nanoparticles Obtained by Micro Segmented Flow Synthesis

02/2011-05/2011      **Research visit** at Louisiana State University, USA

- XAS and SAXS Measurements of ZnO Micro and Nanoparticles
- Generation of Monodisperse Slugs by a Flow-Focused Millifluidic Chip

10/2009      **Research visit** at University of Strasbourg, France

- Synthesis of Core/Shell Polymer Particles by Co-Axial Capillaries Microfluidic Device

07/2006-07/2007      **Organic Synthetic Chemist**, Wuxi Pharmatech Company Ltd. Shanghai, China

Website: [www.wuxiapptec.com](http://www.wuxiapptec.com)

- Synthesized 20 new organic compounds (5-75 g, purity: 95 %)
- Operational knowledge of analytical instruments (HPLC, LCMS,

MS)

09/2003-07/2006

**Master of Science** at Nankai University, Tianjin, China

Major: Polymer Chemistry and Physics

Thesis: Synthesis of Functional Polymer Microspheres and Their Application as Stabilizer for Gold Nanoparticles

09/1999-07/2003

**Bachelor of Science** at Henan Normal University, Xinxiang, China

Major: Chemistry Education

## 6.8 Acknowledgements

The completion of PHD is a long, hard journey. Fortunately, I have met so many warm-hearted people during the last four years who have generously helped me pass through this journey. At the moment when I almost finish my dissertation, I would like to thank all of them for their guide, support, friendship and love.

First and foremost I would like to express my sincere gratitude to my advisor, Prof. J. Michael Koehler. I am very grateful for him to provide this huge opportunity for me and bring me into this warm family, our MRT group. Therefore, I have this great chance to have a brilliant new life in Germany which I will never forget for my entire life. Without his continuous guidance, invaluable insights and encouragement throughout the course of my research work, this dissertation would not have been possible.

Secondly, I am very grateful to the members of our MRT group. I would like to thank Dr. Mike Guenther and Dr. Alexander Gross for their encouragement and suggestions that helped to shape my research skills and for answering all the questions I had in my work from time to time. I also appreciate a lot for their valuable suggestions for my publications and dissertation. Many thanks to Frances for her support and valuable time in assisting with the lab work. I am also grateful to Steffen for helping designing and building up my experimental set-up. He is always available when I have technical problems of my set-up. I also greatly appreciate for his kind and patient help in my life. Andrea, Aniket, Dana, Nikunj and Jessica, thank you for all your friendship and academic support. It is a great pleasure to share the doctoral studies with all of you. My gratitude is also extended to Anette for her understanding and encouragement that carried me through difficult time. In addition, my sincere thanks also go to my dear friend, Jialan. She was the first friendly face to greet me when I came to Ilmenau in 2008. I thank her for sharing my sad and happy moments and also for her encouragement and help during the hard time of my life and work.

I am grateful to Dr. Arne Albrecht for SEM instructions and allowing me to work in the clean room in ZMN. I would also like to thank Dr. Henry Romanus for all nice suggestions and patient guidance with the TEM and SEM measurements. In addition, I also thank Dr. Andrea Csaki (IPHT, Jena) for her kind support and help for fluorescence measurement during the last two

years.

Regarding my research visit in University of Strasbourg, I express my deep gratitude and respect to Prof. Christoph Serrer for his keen interest, strong motivation and constant encouragement during the course of the work. I owe sincere thanks to Dr. Chang Zhenqi for his constant guidance and encouragement in my research work and kind help in my life. Chanjuan, Qianwen, thanks a lot for your friendship and company which left me so many happy and beautiful memories.

Many thanks and regards to Dr. Challa Kumar for inviting me to work in CAMD, Louisianan State University, so I can meet so many kind and interesting people there. I would like to extend my greatest appreciation for his advice, guidance and support in my work and life. Craig and Carryl, thanks a lot for all the paper work which made my trip to USA possible. Greg, Amitava, thank a lot for the XAS measurements. I am very grateful for your valuable advice and help for the measurement and data analysis. I also wish to express my warm and sincere thanks to Henning who helped me so much for the SAXS measurements and was always available when I needed him. I am grateful to him for being so helpful and cooperative. Sanchita, Saichrishna and Lisa, thanks for your support and help in my work and company in my life. Yanshan, your reliable friendship and help is greatly appreciated. Thanks so much for kind suggestions and comfortable conversation to let me know more about American life.

The financial support from TU Ilmenau, State of Thuringia and Stipendium der Landesgraduiertenförderung is gratefully acknowledged. My research visits in LIPHT at University of Strasburg and CAMD at Louisiana State University were funded by Procope Project and the U.S. Department of Energy, Office of Science, and Office of Basic Energy Sciences under Award Number DE-SC0001058, respectively.

Last but not least, I would like to thank my husband Yongbin. He has been always my greatest source of inspiration and strength. I appreciate him a lot for giving me love, freedom, understanding and encouragement to achieve my dreams. Without him, it would have been certainly much harder to finish my PHD. I would also like to express my deepest respect and admiration to my family. I am deeply indebted to them for their unconditional love and endless support throughout the years, which keep me going and never giving up.

---

Shuning Li

Ilmenau, 11.09.2012